



DEFENSE TECHNICAL INFORMATION CENTER

Information for the Defense Community

DTIC® has determined on

Month	Day	Year
02	18	2009

 that this Technical Document has the Distribution Statement checked below. The current distribution for this document can be found in the DTIC® Technical Report Database.

- ☒ **DISTRIBUTION STATEMENT A.** Approved for public release; distribution is unlimited.
- ☐ **© COPYRIGHTED.** U.S. Government or Federal Rights License. All other rights and uses except those permitted by copyright law are reserved by the copyright owner.
- ☐ **DISTRIBUTION STATEMENT B.** Distribution authorized to U.S. Government agencies only. Other requests for this document shall be referred to controlling office.
- ☐ **DISTRIBUTION STATEMENT C.** Distribution authorized to U.S. Government Agencies and their contractors. Other requests for this document shall be referred to controlling office.
- ☐ **DISTRIBUTION STATEMENT D.** Distribution authorized to the Department of Defense and U.S. DoD contractors only. Other requests shall be referred to controlling office.
- ☐ **DISTRIBUTION STATEMENT E.** Distribution authorized to DoD Components only. Other requests shall be referred to controlling office.
- ☐ **DISTRIBUTION STATEMENT F.** Further dissemination only as directed by controlling office or higher DoD authority.
- Distribution Statement F is also used when a document does not contain a distribution statement and no distribution statement can be determined.*
- ☐ **DISTRIBUTION STATEMENT X.** Distribution authorized to U.S. Government Agencies and private individuals or enterprises eligible to obtain export-controlled technical data in accordance with DoDD 5230.25.

REPORT DOCUMENTATION PAGE					Form Approved OMB No. 0704-0188	
<small>The public reporting burden for this collection of information is estimated to average 1 hour per response, including the time for reviewing instructions, searching existing data sources, gathering and maintaining the data needed, and completing and reviewing the collection of information. Send comments regarding this burden estimate or any other aspect of this collection of information, including suggestions for reducing the burden, to Department of Defense, Washington Headquarters Services, Directorate for Information Operations and Reports (0704-0188), 1215 Jefferson Davis Highway, Suite 1204, Arlington, VA 22202-4302. Respondents should be aware that notwithstanding any other provision of law, no person shall be subject to any penalty for failing to comply with a collection of information if it does not display a currently valid OMB control number.</small> PLEASE DO NOT RETURN YOUR FORM TO THE ABOVE ADDRESS.						
1. REPORT DATE (DD-MM-YYYY) 02-02-2009		2. REPORT TYPE Final Technical Report			3. DATES COVERED (From - To) 01/01/2006 - 12/31/2008	
4. TITLE AND SUBTITLE Human Bioresponse to Low-Frequency Underwater Sound				5a. CONTRACT NUMBER		
				5b. GRANT NUMBER N00014-06-01-0299		
				5c. PROGRAM ELEMENT NUMBER		
6. AUTHOR(S) Hamilton, Mark F.				5d. PROJECT NUMBER		
				5e. TASK NUMBER		
				5f. WORK UNIT NUMBER		
7. PERFORMING ORGANIZATION NAME(S) AND ADDRESS(ES) Applied Research Laboratories The University of Texas at Austin PO Box 8029 Austin, Texas 78713-8029				8. PERFORMING ORGANIZATION REPORT NUMBER		
9. SPONSORING/MONITORING AGENCY NAME(S) AND ADDRESS(ES) Office of Naval Research 875 North Randolph Street Arlington, VA 22203-1995				10. SPONSOR/MONITOR'S ACRONYM(S) ONR		
				11. SPONSOR/MONITOR'S REPORT NUMBER(S)		
12. DISTRIBUTION/AVAILABILITY STATEMENT						
20090206068						
13. SUPPLEMENTARY NOTES						
14. ABSTRACT A technical summary of work completed under contract N00014-06-1-0299, entitled "Human Bioresponse to Low-Frequency Underwater Sound," is given. Preliminary research such as the development of two micromechanical models of lung tissue and the calculation of elastic constants based upon such models is described. Progress made in the development of a lumped-element model of the human body and its internal organs is discussed. Master's theses completed under this contract are attached. The results obtained in this investigation may be useful for the determination of non-lethal sound pressure levels in a low-frequency underwater diver deterrence system.						
15. SUBJECT TERMS Lung resonance, micromechanical lung modeling, non-lethal diver deterrence, human bioresponse to underwater sound.						
16. SECURITY CLASSIFICATION OF:			17. LIMITATION OF ABSTRACT UU	18. NUMBER OF PAGES 237	19a. NAME OF RESPONSIBLE PERSON Mark F. Hamilton	
a. REPORT U	b. ABSTRACT U	c. THIS PAGE U			19b. TELEPHONE NUMBER (Include area code) 512-835-3106	



APPLIED RESEARCH LABORATORIES
THE UNIVERSITY OF TEXAS AT AUSTIN

P. O. Box 8029 • Austin, Texas 78713-8029 • (512) 835-3200 • FAX: (512) 835-3259

02 February 2009
SISL-09-18
MFH/rb

Dr. Robert H. Headrick
Ocean Acoustics
Office of Naval Research
875 North Randolph Street, Suite 1425
Code 321OA
Arlington, VA 22203-1995

Re: Contract N00014-06-1-0299; Human Bioresponse to Low-Frequency Underwater Sound; Final Report

Enclosed is a copy of the Final Report under the above referenced contract. This delivery is in fulfillment of the contract requirement.

Feel free to call or email me if you have any questions for comments.

Sincerely,

A handwritten signature in cursive script that reads "Mark F. Hamilton".

Mark F. Hamilton
Signal and Information Sciences Laboratory

Human Bioresponse to Low-Frequency Underwater Sound

Final Report to the Office of Naval Research
02 February 2009

Mark F. Hamilton
Applied Research Laboratories
The University of Texas at Austin
P.O. Box 8029
Austin, Texas 78713-8029
phone: (512) 835-3106 fax: (512) 835-3100 email: hamilton@mail.utexas.edu

Award Number: N00014-06-1-0299
<http://www.arlut.utexas.edu/>

LONG-TERM GOALS

The ultimate goal of our research is to provide a physiologically and acoustically based prediction of human lung damage due to low-frequency underwater sound. The threshold curve we will produce will indicate the acoustic pressure at which damage may occur as a function of frequency and exposure time. Our results will aid others in determining whether the sound pressure levels produced or predicted using various diver deterrent systems allow it to function in the nonlethal regime.

OBJECTIVES

The first objective is to determine how the human body responds to low-frequency underwater sound and what causes the hemorrhaging in the lungs, which is commonly the first encountered injury modality. The second objective is to use this understanding of lung damage to create a damage threshold curve which indicates the predicted acoustic pressure, as a function of frequency, below which injury may be avoided.

APPROACH

This work is a continuation of the work completed under contract N00014-06-1-0299. A finite element model of human thorax has now been created that includes idealized geometrical representations of the lungs, ribs, trachea, bronchiole tubes, spine, sternum, and a generalized "abdominal mass" which accounts for the diaphragm, stomach, kidneys, and spleen. The elastic properties of the lungs are calculated using a micromechanical model that accounts for the internal micromechanical structure of individual alveoli and takes a spatial average of the resulting elastic constants to determine the lung model's Lamé constants. The resulting finite-element model of the effective medium then calculates the response of the lung and other peripheral organs to low-frequency underwater sound, with a focus on lung surface displacement

and calculated shear stress and shear strain. If instantaneous damage (as opposed to cumulative damage) is being investigated, a series of simulations over a range of frequencies allows for the determination of the acoustic pressure required to cause a shear strain equal to that believed to be the threshold level for instantaneous damage in the lungs. If cumulative damage is of interest, a progressive damage model has been developed which modifies local elastic properties of the lungs based on the amount of shear strain calculated in the previous solution.

The team members on this project are:

Mark F. Hamilton, Professor and Principal Investigator
Yurii A. Ilinskii, Senior Research Scientist
Evgenia A. Zabolotskaya, Senior Research Scientist
Mark S. Wochner, Postdoctoral Fellow
Sarah L. Gourlie, Graduate Student
Paul A. Waters, Graduate Student
Theresa Y. Cheung, Undergraduate Student

WORK COMPLETED

Substantial progress has been made over the duration of our grant, particularly on our model of the human lung. In addition to descriptions of our progress in monthly ONR reports, we have disseminated our work publicly through a series of oral presentations at biannual meetings of the Acoustical Society of America. The contents of these ASA meeting presentations are summarized in published abstracts [Wochner et al. 2006, Ilinskii et al. 2006, Wochner et al. 2007a, Wochner et al. 2007b]. We have also presented our work in seminars at the Indiana University School of Medicine [Hamilton 2007] and at the University of Rochester Center for Biomedical Ultrasound [Wochner 2007]. Because our work is so novel, we have made an effort to disseminate our results as widely as possible in order to solicit maximum feedback from the acoustics, biomechanics, and medical communities. Feedback from these communities has been positive, giving us confidence in our approach. The indented passages that follow are the published ASA meeting abstracts.

We began by developing a micromechanical model of lung based on individual alveoli as the fundamental elements [Wochner et al. 2006]:

This work is focused on studying the dynamics of the human lung in response to low-frequency sound. The model developed uses individual alveoli as the basic unit cells, which are represented as truncated octahedra [Y. C. Fung, *J. Appl. Physiol.* **64**, 2132 (1988)]. Having 14 faces, this polyhedron possesses the smallest surface-to-volume ratio of any polyhedron capable of filling three-dimensional space. Unlike previous quasistatic models of this type, typically used to predict elastic properties of the lung, ours is a dynamical model. Mass is concentrated at the vertices of the polyhedra. Viscoelastic properties of the collagen and elastin in lung tissue are taken into account using a Kelvin model that is augmented to account for nonlinear elasticity. The Kelvin elements connect the point masses along the edges and across the faces of the polyhedra. Although not yet taken into account, the model permits inclusion of alveolar ducts by opening or closing

selected faces of the polyhedra to accommodate airflow. Numerical simulations of small alveolar clusters subjected to different excitations and geometric constraints will be shown.

With the objective of developing an effective medium model that can be implemented in commercial finite-element software packages, we next developed a semi-analytic model using classical elasticity theory to describe an anisotropic medium possessing the cubic symmetry of aveoli modeled as the truncated octahedron described above [Ilinskii et al. 2006]:

As described in a companion abstract, an investigation is underway to develop a bioacoustic model of human lung. In parallel with the numerical model described in the companion abstract, a semianalytic model is being developed. The basic unit cell, a truncated octahedron, is the same. In contrast here, the medium is assumed to be infinite in extent. The resulting lattice possesses cubic symmetry, and, for homogeneous deformation, all material properties are determined by a single unit cell. Deformation of the unit cell is determined by the 24 vertices of the polyhedron, only 6 of which are independent. In this presentation we discuss quasistatic deformation of the discretized medium, and thus ignore inertia and energy dissipation. An analytic model for the nonlinear elasticity of collagen and elastin is used to determine the stiffnesses of the springs connecting vertices of the polyhedra. Minimization of the potential energy for a given macroscopic deformation permits calculation of microscopic deformation within the unit cell, which in turn determines the stresses and therefore the elastic constants. Sample calculations will be presented, including the longitudinal and transverse wave speeds in the medium as functions of direction and orientation.

A significant finding in the work described in the preceding abstract was that the acoustic wave speed in lung that was predicted on the basis of the elastic constants determined by this model was in close agreement with the very low sound speed measurements reported in the literature, which are about 40 m/s. Not mentioned, but also modeled at the time of the above two presentations, are effects of surface tension and surfactant in lung tissue. The latter gives rise to hysteresis.

The next step was to convert the anisotropic medium formed by the truncated octahedra to an effective isotropic medium, because on the macroscopic level (much larger than alveoli, but much smaller than the lungs themselves) the tissue may be considered to be isotropic. This was accomplished by spatially averaging the three elastic constants for the anisotropic medium over all orientations to obtain the two elastic constants for an isotropic medium, e.g., the bulk modulus and shear modulus [Wochner et al. 2007a]:

This presentation is an extension of work described previously [Ilinskii et al., J. Acoust. Soc. Am. **120**, 3194 (2006)] on modeling the response of human lung to low-frequency underwater sound. A lumped element model with alveoli represented as truncated octahedra forming a periodic lattice with cubic symmetry was developed to capture the microscopic properties of collagen and elastin. The lattice is deformed quasistatically to determine the three elastic constants associated with the macroscopic behavior of the system. In reality lung tissue is likely isotropic and therefore a method of averaging is utilized to determine the two Lamé constants of the effective medium. The volume of the

lung is varied to simulate tidal breathing. The Lamé constants are determined for the given lung volume and used in a commercial finite element package to calculate the amplitude of vibration due to low-frequency acoustic excitation. The resulting spectral response and scattered sound field are calculated for a water-loaded viscoelastic sphere composed of the effective lung medium. Increase in lung volume tends to decrease the resonance frequency, but increasing stiffness due to collagen tends to increase the resonance frequency. Competition of these effects is discussed.

Using this approach for simple lung geometry (a sphere) we thus showed that the lung resonance frequency can be a non-monotonic function of lung volume during a normal breathing cycle, owing to the nonlinear elasticity of collagen and elastin fiber bundles in lung tissue.

Most recently, we configured our finite-element model to calculate scattered sound pressure as a function of the amplitude and frequency of sound waves incident on a pair of lungs in water, along the lines of the measurements of lung resonance made by Martin et al. [2005]. Additionally, inhomogeneity of the lung was taken into account in our finite-element model [Wochner et al. 2007b]:

An effective medium, finite element model has been developed for human lung response to low-frequency underwater sound [Wochner et al., *J. Acoust. Soc. Am.* **121**, 3082 (2007)]. Macroscopic properties are determined by averaging over microscopic properties associated with lung tissue elasticity and alveolar geometry. The resulting elastic constants depend on lung volume and thus vary with the phase of the breathing cycle. This presentation discusses effects due to spatial variations in lung and geometric features specific to the anatomy of lung. An important variation in elastic properties occurs where soft tissue of the parenchyma attaches to much stiffer bronchial tissue, resulting in stresses that may cause injury at high levels of acoustic excitation. A factor affecting inhomogeneity within the parenchyma is the orientation of the swimmer. When vertical, the suspension of the lung under its own weight may cause the stiffness to be higher at the top of the lung than at the bottom, resulting in a change in the lung resonance frequency. Finally, patient-specific geometries based on volumetric data of the human thorax are considered. Results will be presented showing stress and strain fields, lung resonance, and mode shapes.

One prediction reported in this presentation was an increase in lung resonance frequency in the upright versus prone position of the human subject, which was later found to be consistent with measurements reported by Dr. Edward Cudahy at a recent ONR program review [Cudahy 2007].

Finally, we have also made headway on developing a lumped-element model of the human body and its internal organs to account for whole-body vibration due to gradients in the sound field. Our approach to this problem is entirely different from that for studying lung resonance phenomena. The analysis is based on a five-degree-of-freedom body model developed by Henning von Gierke [1971], who wrote that “The model is used to calculate body deformations (thorax compression, pressure in the lungs, airflow into and out of the lungs, diaphragm and abdominal mass movement) as a function of external longitudinal forces (vibration or impact) and pressure loads (blast, infrasonic acoustic loads).” The corresponding state equations were derived and are being used to calculate frequency responses of body deformations due to an incident low-frequency sound wave in water. An extensive literature

search is underway to identify other potentially relevant whole-body vibration models that might provide independent confirmation of the predicted frequency responses, and also to find measurements made in frequency ranges relevant to our problem.

IMPACT/APPLICATIONS

For development of non-lethal methods of swimmer neutralization based on low-frequency underwater sound, our research will help estimate acoustic thresholds below which serious or fatal injuries may be avoided. In addition, this finite element thoracic model may also be useful for a variety of other applications including simulation of human lung response to blast waves and comparison of lung dynamics in health and disease.

REFERENCES

- E. A. Cudahy, "Underwater acoustics: Human effects review," Non-Lethal Weapons Bioeffects Program Review, Office of Naval Research (17-18 July 2007).
- M. F. Hamilton, "Biomechanical model of human lung response to low-frequency underwater sound," invited seminar, Indiana University School of Medicine (2007).
- Yu. A. Ilinskii, M. S. Wochner, M. F. Hamilton, and E. A. Zabolotskaya, "Infinite periodic model of human lung," *J. Acoust. Soc. Am.* **120**, 3194(A) (2006).
- J. S. Martin, P. H. Rogers, and E. A. Cudahy, "Measurement of the depth-dependent resonance of water-loaded human lungs," *J. Acoust. Soc. Am.* **117**, 2291-2300 (2005).
- H. E. von Gierke, "Biodynamic models and their applications," *J. Acoust. Soc. Am.* **50**, 1397-1413 (1971).
- M. S. Wochner, "Biomechanical modeling of lung response to low-frequency underwater sound," RCBU Seminar Series, Rochester Center for Biomedical Ultrasound, University of Rochester (2007).
- M. S. Wochner, Yu. A. Ilinskii, M. F. Hamilton, and E. A. Zabolotskaya, "Finite aperiodic model of human lung," *J. Acoust. Soc. Am.* **120**, 3194(A) (2006).
- M. S. Wochner, Yu. A. Ilinskii, M. F. Hamilton, and E. A. Zabolotskaya, "Effective medium model of human lung response to low-frequency sound," *J. Acoust. Soc. Am.* **121**, 3082(A) (2007a).
- M. S. Wochner, Y. Zhang, Yu. A. Ilinskii, M. F. Hamilton, and E. A. Zabolotskaya, "Influence of inhomogeneity and geometry on lung response to low-frequency underwater sound," *J. Acoust. Soc. Am.* **122**, (A) (2007b); in press.

PUBLICATIONS (Master's Theses—See attachments for full text)

S. L. Gourlie, "Whole-Body Vibration of Humans Due to a Low-Frequency Underwater Sound Field," Master's thesis, The University of Texas at Austin (Aug 2008).

P. A. Waters, "Two-Dimensional Microscopic Model of Lung Tissue Response to Acoustic Excitation," Master's thesis, The University of Texas at Austin (Dec 2008).

HONORS/AWARDS/PRIZES

Sarah L. Gourlie, an M.S. student at The University of Texas at Austin who was supported on this project and whose thesis (August 2008) is entitled "Whole-Body Vibration of Humans Due to a Low-Frequency Underwater Sound Field," received the Best Student Paper Award from the Technical Committee on Noise at the Spring 2008 Meeting of the Acoustical Society of America in Paris, France.

Copyright

by

Sarah Lynn Gourlie

2008

Whole-Body Vibration of Humans due to a Low-Frequency Underwater Sound Field

by

Sarah Lynn Gourlie, B.S.

Thesis

Presented to the Faculty of the Graduate School of

The University of Texas at Austin

in Partial Fulfillment

of the Requirements

for the Degree of

MASTER OF SCIENCE IN ENGINEERING

The University of Texas at Austin

August 2008

**Whole-Body Vibration of Humans due to a
Low-Frequency Underwater Sound Field**

**Approved by
Supervising Committee:**

Acknowledgments

I would like to thank my advisor, Dr. Mark Hamilton, for his guidance and support throughout this project and the course of my graduate studies. His investment in his students is admirable, and I cannot thank him enough for his time, patience, and encouragement. Thanks to Dr. Preston Wilson for being the second reader for this thesis. I'd also like to express my appreciation to Mark Wochner and to my fellow students in the acoustics program here at The University of Texas at Austin for all their friendship and advice.

I must also thank all of the influential educators in my life. I think I have managed to learn something from every teacher and professor I have ever had, and I am greatly indebted to all of them for fueling my love of learning.

A huge thank you to my family: my parents, William and Kathleen Gourlie, my brother Don, and grandmothers, Rose Plankey and Marion Gourlie, for their constant love and support. They have always believed in me and encouraged me in every endeavor. Finally, thank you to Michael Gale for being my someone to fall back on.

The work was supported by the Applied Research Laboratories McKinney Fellowship in Acoustics, and by the Office of Naval Research.

SARAH LYNN GOURLIE

Whole-Body Vibration of Humans due to a Low-Frequency Underwater Sound Field

Sarah Lynn Gourlie, M.S.E.

The University of Texas at Austin, 2008

Supervisor: Mark F. Hamilton

Possible effects of whole-body vibration of humans that occur as a result of low-frequency underwater acoustic excitation are discussed, with the aim of predicting discomfort or potential injury to divers from low-frequency sonar. The frequency range of interest is 40-80 Hz, which encompasses the resonance of the human lung. It is assumed that the diver is neutrally buoyant and will therefore experience whole-body acceleration equal to the particle acceleration produced by the sound field in the absence of the diver. A literature review of experiments, models, and standards for whole-body vibration in air was conducted, the findings of which were used in an attempt to draw conclusions about the effects of whole-body vibration in an underwater environment. Emphasis is placed on using lumped-element biodynamic models of the human body to predict the response of different body parts to the whole-body vibration. Unfortunately, it is difficult to interpret the results of these simulations, as no data on motion within the body have been found by the author.

It is especially clear that experiments at frequencies above 20 Hz are required before conclusions can be drawn. One apparent conclusion, however, is that the effect of the acoustic pressure of the wave will dominate over whatever effects occur as a result of the particle acceleration; therefore, the effects of the whole-body vibration will most likely be unimportant.

Contents

Acknowledgments	iv
Abstract	v
List of Figures	ix
Chapter 1 Introduction	1
Chapter 2 Observed Effects of Whole-Body Vibration	7
2.1 Early Experiments	8
2.2 Standards	10
2.3 Other Negative Effects	14
2.4 Summary	16
Chapter 3 Compilation of Whole-Body Vibration Models	18
3.1 Seated Subjects	19
3.2 Standing Subjects	23
3.3 Models Including Lungs	26
Chapter 4 Von Gierke's Five-Degree-of-Freedom Model	31
4.1 Corroboration with Given Results	32
4.2 Adaptation for Underwater Environment	37

4.3	Sources and Source Placement	39
4.4	Lung Resonance	44
4.5	Results from the Model	49
4.6	Comparison to ISO 2631	54
Chapter 5 Coermann's Circuit Model		57
5.1	Finding the Parameter Values	60
5.2	Physical Interpretation of the Model	66
Chapter 6 Other Models		69
6.1	Plan of Action	69
6.2	Results	70
6.2.1	Wan and Schimmels [38]	70
6.2.2	Muksian and Nash [40] and Quassem [41] et al.	71
6.2.3	Smith [43]	73
6.2.4	Mertens	73
6.2.5	Yue and Mester [46]	74
6.2.6	Garg and Ross [44]	75
6.3	Generalizations	76
Chapter 7 Conclusion		79
Appendix A Derivation of Added Mass		82
Bibliography		87
Vita		93

List of Figures

1.1	Approximate comparison between size of wavelength and size of diver for low-frequency sonar	2
1.2	Input acceleration amplitude as a function of frequency for (a) 190 dB and (b) 230 dB.	5
2.1	Dieckmann's <i>K</i> -scale for vertical vibration with underwater sound field input accelerations added by present author in red [28].	9
2.2	Results of vibration duration experiments with underwater sound field input accelerations in red. After Magid et al. [2], with red lines added by present author.	10
2.3	Griffin's comparison of vertical vibration limits: (a) ISO 2631 (1985) versus BS 6841 (1987); (b) ISO 2631 (1985) versus ISO 2631 (1997); (c) BS 6841 (1987) versus ISO 2631 (1997). Curves of decreasing amplitude, shown for 1 s, 1 min, 1 h, 8 h, 24 h, respectively. From Griffin [22].	12
2.4	ISO 2631 limits for 1 minute exposure time with underwater sound field input accelerations.	13
2.5	Accelerations Corresponding to a VDV of 15 as in BS 6841.	14
2.6	Griffin's visual acuity guidelines [19]. Red lines added by present author.	16

3.1	Dynamic Response Index model. After von Gierke [17].	19
3.2	Models from Liang and Chiang's compilation [34]. References in individual labels cite the original work used by Liang and Chiang. . . .	20
3.3	Mertens's model for seated subjects [42].	22
3.4	Smith's model for seated subjects [43].	23
3.5	Garg's model for standing subjects [44].	24
3.6	Standing model by Gupta [45].	25
3.7	Yue and Mester's 'wobbling mass' model [46].	26
3.8	Five-degree-of-freedom model by von Gierke [15].	27
3.9	von Gierke's concept model [10].	28
3.10	Circuit model of supine human. Adapted from Coermann et al. [3]. .	29
4.1	von Gierke's five-degree-of-freedom model [14].	32
4.2	Bond graph for von Gierke's 5-DOF model.	34
4.3	Comparison of abdomen and chest wall displacement responses due to constant velocity amplitude buttocks excitation for von Gierke's model. (a) after von Gierke [14], (b) calculations based on Equations (4.1)–(4.4).	37
4.4	Abdominal mass acceleration response with input SPL of 230 dB and diver depth of 0 m. Two sets of curves are shown, one where the acoustic pressure is applied to the chest wall along with the acceleration source(s), and one with only the acceleration source(s) applied to the model. Each set has three acceleration source placement options: blue—source applied to torso alone, red—source applied to pelvis alone, and black—source applied to both torso and pelvis. The three curves are indistinguishable when the acoustic pressure is also applied as a source.	41

4.5	Reduced bond graph of von Gierke's model after source placement decisions were made.	43
4.6	Experimental results for lung resonance as a function of water depth. After Martin et al. [1].	45
4.7	Thoracic cavity response from von Gierke's model at depths of 0 and 36 m.	46
4.8	Possible changes to abdominal characteristics.	47
4.9	Thoracic cavity response from model with parameters optimized for agreement of predicted resonance frequencies with measurements by Martin et al. [1].	48
4.10	Response of the abdominal mass.	50
4.11	Response of the chest wall mass.	51
4.12	Response of the respiratory mass.	52
4.13	Response of the thoracic cavity.	52
4.14	Responses with both acoustic pressure and particle acceleration applied as sources. Solid lines are with the particle acceleration input alone, and dotted lines are with both pressure and particle acceleration applied. Blue lines have an excitation source SPL of 230 dB and red lines have an excitation source SPL of 190 dB.	54
4.15	Acceleration responses of the abdomen and chest wall to input from ISO 2631 exposure limit compared with responses calculated in Section 4.5.	56
5.1	Experimental setup for Coermann et al. [3].	58
5.2	Results of experiment by Coermann et al. [3].	58
5.3	Circuit model used by Coermann et al. [3].	59
5.4	Frequency response of circuit model used by Coermann et al. [3].	59

5.5	Mechano-acoustic analogue of the chest with equivalent electrical circuit. R_A , M_A and C_A are the airway resistance, inertance, and alveolar air capacitance, and R_T , M_T , and C_T are the tissue resistance, inertance, and compliance. In the electrical analogue, the airway elements correspond to elements with subscript 1, and the tissue elements correspond to elements with subscript 2. After DuBois et al. [50].	60
5.6	Bond graph of circuit model in Figure 5.3.	63
5.7	Attempt to re-create frequency response calculations [3] shown in Figure 5.4, using parameter values from DuBois et al. [50].	66
5.8	Mechanical analogue of the circuit model by Coermann et al.	67
6.1	Response of the ‘viscera’ from Wan and Schimmels [38]. Parameter values used are [34]: $m_1=36$ kg, $m_2=5.5$ kg, $m_3=15$ kg, $m_4=4.17$ kg, $c_1=2,475$ N-s/m, $c_2=330$ N-s/m, $c_3=200$ N-s/m, $c_{31}=909.1$ N-s/m, $c_4=250$ N-s/m, $k_1 = 49,340$ N/m, $k_2 = 20,000$ N/m; $k_3 = 10,000$ N/m, $k_{31} = 192,000$ N/m, $k_4 = 134,400$ N/m.	71
6.2	Responses from Muksian and Nash’s model [40]. Parameter values used are [34]: $m_1 = 27.23$ kg, $m_2 = 5.921$ kg, $m_3 = 0.455$ kg, $m_4 = 1.362$ kg, $m_5 = 32.762$ kg, $m_6 = 6.82$ kg, $m_7 = 5.45$ kg, $c_2 = c_3 = c_4 = c_5=292$ N-s/m, $c_{56} = c_6 = c_7 = 3,580$ N-s/m, $k_2 = k_3 = k_4 = k_5 = 877$ N/m, $k_{56} = k_6 = k_7 = 52,600$ N/m.	72
6.3	Response of the torso/chest mass in Smith’s model. Parameter values are [43]: $M_1 = 28.1$ kg, $M_2 = 11.8$ kg, $K_2 = 162,671$ N/m, $C_2 = 17.5$ N-s/m, $M_3 = 17.2$ kg, $K_3 = 37,230$ N/m, $C_3 = 332$ N-s/m. . . .	73

6.4	Responses from Mertens's model. Parameter values are [42]: $M_1 = 15$ kg, $K_1 = 47,966$ N/m, $C_1 = 678$ N-s/m, $M_2 = 10$ kg, $K_2 = 250,000$ N/m, $C_2 = 4,000$ N-s/m, $K_3 = 200,000$ N/m, $C_3 = 1,000$ N-s/m, $M_4 = 15$ kg, $K_4 = 17,913$ N/m, $C_4 = 622$ N-s/m, $K_5 = 160,000$ N/m, $C_5 = 2,000$ N-s/m, $M_6 = 22$ kg, $K_6 = 42,558$ N/m, $C_6 = 968$ N-s/m, $M_7 = 7$ kg, $K_7 = 89,537$ N/m, $C_7 = 633$ N-s/m. . . .	74
6.5	Response of the wobbling mass in the model by Yue and Mester [46]. Parameter values are: $M_1 = 6.15$ kg, $M_2 = 6$ kg, $M_3 = 12.58$ kg, $M_4 = 50.34$ kg, $k_1 = 6$ kN/m, $k_2 = 6$ kN/m, $k_3 = 10$ kN/m, $k_4 = 10$ kN/m, $k_5 = 18$ kN/m, $c_1 = 300$ N-s/m, $c_2 = 650$ N-s/m, $c_4 = 1900$ N-s/m.	75
6.6	Response of the inner organs in Garg and Ross's model. Parameter values are [44]: Masses(kg): $M_1 = 4.76544$, $M_2 = 0.0544872$, $M_3 = 0.05450472$, $M_4 = 23.1264$, $M_5 = 7.48104$, $M_6 = 7.48104$, $M_7 = 3.04848$, $M_8 = 3.04848$, $M_9 = 2.4528$, $M_{10} = 2.04984$, $M_{11} = 2.04984$, $M_{12} = 1.161576$, $M_{13} = 1.161576$, $M_{14} = 4.09968$, $M_{15} = 4.09968$, $M_{16} = 0.001752$. Springs (N/m): $k_{115} = 175200$, $k_{1415} = 35040$, $k_{415} = 3153.6$, $k_{414} = 2277.6$, $k_{514} = 359160$, $k_{614} = 359160$, $k_{57} = 359160$, $k_{68} = 359160$, $k_{79} = 359160$, $k_{89} = 359160$, $k_{1015} = 26280$, $k_{1115} = 26280$, $k_{1012} = 26280$, $k_{1113} = 26280$, $k_{212} = 26280$, $k_{313} = 26280$, $k_{116} = 129.648$. Dampers (N-s/m): $c_{115} = 17.52$, $c_{1415} = 350.4$, $c_{415} = 52.56$, $c_{414} = 31.536$, $c_{514} = 963.6$, $c_{614} = 963.6$, $c_{57} = 963.6$, $c_{68} = 963.6$, $c_{79} = 963.6$, $c_{89} = 963.6$, $c_{1015} = 175.2$, $c_{1115} = 175.2$, $c_{1012} = 175.2$, $c_{1113} = 175.2$, $c_{212} = 175.2$, $c_{313} = 175.2$, $c_{116} = 0.00876$	76
A.1	Geometry for a general axisymmetric spherical source.	83
A.2	Geometry for the vibrating cap.	85

Chapter 1

Introduction

Human bioresponse to acoustic excitation has been studied in many contexts and many ways. From the pain caused in the ears by loud noise to seasickness, acoustic waves and vibration have widely varying effects on humans. Of particular interest to this thesis are the effects of what is known as whole-body vibration; low-frequency translational vibration of the human body, as experienced, for example, in a car on a bumpy road. The motivation for this research is the creation of a nonlethal underwater deterrent system for harbors which will make use of intense low-frequency acoustic waves in water.

The frequency range for the acoustic waves is 40 to 80 Hz, which was chosen to encompass measured resonances of the human lung [1]. Corresponding wavelengths for these frequencies in seawater are between 18 and 38 m. An approximate scale for this situation is shown in Figure 1.1. With these long wavelengths, the human body is small enough to be approximated by lumped elements. Thus, responding to the acoustic pressure, the body pulsates like a bubble due to the lung cavities, and responding to the particle velocity of the wave, the body will experience whole-body vibration. Much work is being done to understand the body's response to the acoustic pressure of these waves, particularly the lung's response, as it is understood

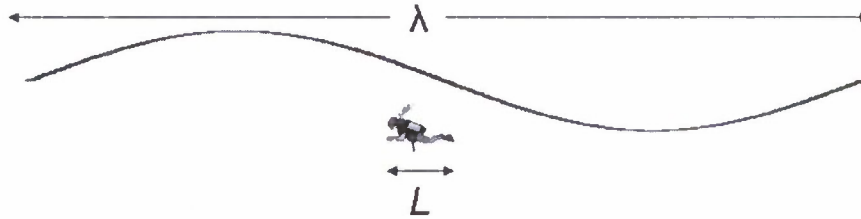


Figure 1.1: Approximate comparison between size of wavelength and size of diver for low-frequency sonar

that the response of the lung to the acoustic pressure will be the main and most severe response to the sound. However, in the interest of understanding all of the effects of the underwater acoustic wave, the effects of the translational vibration associated with the particle velocity are studied in detail in this thesis. It is the aim of this thesis to understand the effects of whole-body vibration on humans well enough to predict whether the whole-body vibration from the particle velocity of the underwater sound source will produce an effect on the diver that is comparable to the effect of the acoustic pressure on the lungs.

The first step taken to understand the effects of this underwater whole-body vibration source was to perform a literature search on whole-body vibration, gathering as much information as possible. Whole-body vibration experiments and studies as well as lumped-element models of the human body that match vibration data were found, with everything focused solely on vibration in air. The bulk of the papers found by the author were studies done by von Gierke's group at the Wright-Patterson Air Force Base [2, 3, 4, 5, 6, 7, 8, 9, 10, 11, 12, 13, 14, 15, 16, 17, 18], and by Michael Griffin in the Human Factors Unit of the Institute for Sound and Vibration Research [19, 20, 21, 22, 23, 24, 25, 26, 27]. From this literature search there seem to be two different ways of understanding the whole-body vibration that occurs due to the underwater sound field.

The first approach used by the author involves comparing the excitation from

the underwater sound wave to inputs of vibration experiments, and using the results of the experiments to predict the effect of the underwater excitation. There has been extensive experimentation on and modeling for whole-body vibration in air, with most of the work done in the context of vehicle vibration, thus dealing with seated subjects vibrated with frequencies under 20 Hz. These specifications are not particularly applicable to the context of the underwater sound field in the frequency range of 40 to 80 Hz, but attempts to extrapolate information are made. Chapter 2 details several experiments as well as two standards for limiting vibration exposure, and uses the results and limits found in these documents to put the input of the underwater sound field in the context of whole-body vibration.

The second approach is to use lumped-element models of the human body that were created to interpret vibration data. Although the data used to make the models were all taken in air, and usually at frequencies under 20 Hz, the models can be changed to account for different assumptions or contexts. Although this may be a more accurate way to get data, the problem arises that the results obtained are the motions of effective model elements within the body, and difficulties arise when trying to interpret the predicted motions. However, the models are one of the best ways to begin to understand what might be happening within the body as a result of the whole-body vibration. Chapter 3 is a compilation of the whole-body vibration models gathered, with as much detail and context as is known by the author. Only linear lumped element models were gathered, so there is a wider selection of models that include nonlinear parameters or use finite element modeling methods. Chapters 4, 5, and 6 detail the work done by the author to interpret the models and adapt them for the underwater sound excitation and the assumptions forthcoming in the Introduction. Also, results from the models are shown, although little interpretation can be given.

It is important to note that throughout this thesis, and using either approach,

the excitation sound wave, which is the source of the vibration, does not change. Although the modal structure of low-frequency sound in shallow water could be taken into account, the input wave is assumed to be a time-harmonic progressive plane wave for simplicity. An expected sound pressure level (SPL) for a typical low-frequency single sonar source such as this one is 190 dB re 1 μ Pa. An upper limit for the SPL, due to onset of cavitation, is 230 dB, and all through the paper the two values of 190 and 230 dB will be used as the two inputs that are considered. To find the input vibration amplitude from these SPL values, it is first assumed that the diver is neutrally buoyant. This is a reasonable assumption, as it is common practice for scuba divers to be neutrally buoyant in order to maintain depth control. When the diver is neutrally buoyant and approximated as an entrained particle in the low-frequency wave, he will oscillate with velocity and acceleration equal to the particle velocity and acceleration of the wave. Two quantities are of interest, the peak pressure and acceleration amplitudes in the wave. Because the excitation wave is a progressive plane wave, these can be calculated for a single frequency, f , from the definition of sound pressure level. The acoustic pressure amplitude is

$$p_0 = \sqrt{2} \times 10^{(\text{SPL}/20)-6} \text{ Pa} \quad (1.1)$$

and the particle acceleration is

$$a_0 = \frac{2\pi f p_0}{\rho_0 c_0} = 4.2f \times 10^{(\text{SPL}/20)-12} \text{ m/s}^2, \quad (1.2)$$

where ρ_0 is the density and c_0 the sound speed of seawater, which are taken to be 1026 kg/m³ and 1500 m/s, respectively. Acceleration is most commonly used in the context of whole-body vibration with units of g , the acceleration due to gravity ($g = 9.81 \text{ m/s}^2$). Figure 1.2 is a plot of the acceleration input amplitudes that are linearly increasing with frequency for the range of 40 to 80 Hz, which shows that a

difference of 40 dB in SPL generates a difference of two orders of magnitude in the input accelerations.

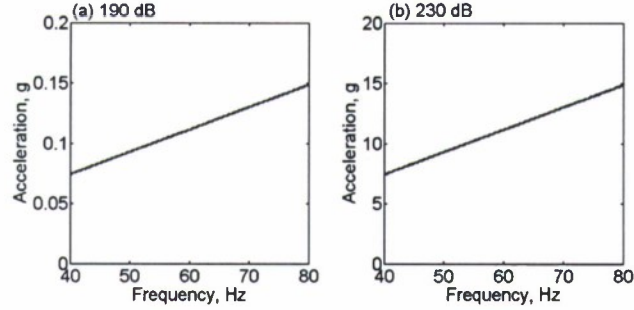


Figure 1.2: Input acceleration amplitude as a function of frequency for (a) 190 dB and (b) 230 dB.

Another important assumption that is made throughout this thesis is that the diver is perfectly horizontal in the water, with a horizontally propagating wave as the excitation. With such an orientation, all of the vibration is along the spinal axis of the diver, which is the axis where vibration is applied in most experiments and models. This assumption is not entirely realistic, as there is no way to know or control the diver's orientation in the water. However, the assumption provides an upper limit, where if the assumption is true, the diver is subjected to the maximum amount of vibration along the spinal axis. So it must be understood that the inputs shown throughout the paper are the absolute maximum vibration the diver would experience along the spinal axis for a given sound pressure level and frequency.

Because all of the whole-body vibration experiments have been performed in air, the models created are either for standing or seated subjects, and it has also been concluded that the posture (erect, relaxed, etc.) of the subject has an effect on the response of the body. For a submerged, neutrally buoyant diver, the diver is neither seated nor standing, and 'posture' is not really applicable. It is not clear whether using a standing subject model or a seated subject model is more accurate, but it is most likely that this will not matter, as the focus for this thesis is on the

inner organs and the open cavities of the body. This is because these inner organs experience the greatest relative motion with respect to the skeleton than any other part of the body, so there is greater possibility for discomfort and injury. For this reason, it is detail of the inner organs that determines the relevance of the model, rather than the posture.

Another observation is that for experiments performed in air on seated or standing subjects, gravity is acting as a force on the body and on the organs within the body along the spinal axis—the axis of vibration. However, a neutrally buoyant diver horizontal in the water experiences gravity in a different way, as different organs have different masses, the gravitational force is not uniform within the body. It will be assumed, however, that the effect of gravity is negligible compared to the input sound wave, and that in any case the body is in dynamic equilibrium in the absence of the acoustic excitation. Since only linear systems are considered, gravity will therefore have no effect on the dynamic responses of the individual organs and henceforth it will be omitted from the models and discussion.

Under these assumptions and simplifications, there can be some understanding of the effects of the whole-body vibration due to the acceleration associated with a low-frequency underwater sound wave. However, it is understood that many simplifications are used, and extrapolating the reported experiments and models to frequencies above 20 Hz may not be valid. It is important to realize that models are made to serve a specific purpose, and attempting to use a model for a different purpose may be invalid. This thesis uses the information available in an attempt to get the most comprehensive and accurate understanding of whole-body vibration in an underwater context, but it is emphasized that more work and experimentation is needed to fully understand this topic.

Chapter 2

Observed Effects of Whole-Body Vibration

The first method used to understand the effects of the underwater sound field as a whole-body vibration source is to compile and extrapolate from known effects of whole-body vibration. This chapter reviews some experiments that have been conducted to understand human response to whole-body vibration and presents safety limits that have been proposed in standards. Most studies are performed with subjects seated or standing on a vibrating platform, and measurements are taken using accelerometers or pressure sensors. Subjective responses from the subjects are often recorded as well. Experiments on humans test the limits of perception, comfort, and tolerance, and experiments on animals have surpassed these limits in an attempt to understand how a body might be injured as a result of vibration.

Some problems with this method lie in the fact that since most of the experiments were done in air, it is unknown if the results can be used to accurately interpret an underwater situation. Also, very little experimentation was done in the frequency range of interest, so results are extrapolated to the frequency range. Finally, since all experiments were done in controlled situations with subjects who

were aware of what they were experiencing, an actual reaction to a first-time exposure underwater is impossible to predict. However, these experiments are the closest approximation to the true situation, and will allow insight into the effects of whole-body vibration.

2.1 Early Experiments

The first experiment found by the author was published in 1958 by Dieckmann [28]. His experimental procedure tested sitting and standing positions, horizontal and vertical vibrations, and a frequency range up to 100 Hz. His main results include head-movement diagrams, impedance plots, and tolerance curves based on strain. Dieckmann introduced a K -scale, where ' K ' is the degree of strain. Dieckmann created a scale in which a $K = 10$ should be allowed only for a short time, and a $K = 100$ is the upper limit of strain for the average person. Figure 2.1 shows the K curves on a plot of acceleration vs. frequency, with the input from the sound field at 190 dB and 230 dB added for comparison. Clearly, if 230 dB can be achieved then the exposure limit will be surpassed, and 190 dB passes the $K = 1$ line. Further calculation shows that the minimal SPL to exceed the strain limit at approximately 40 Hz is around 220 dB.

A number of researchers at the Aerospace Medical Research Laboratory at Wright-Patterson Air Force Base conducted a group of whole-body vibration experiments in the early 1960s. The Air Force Medicine community was focused on this research at the time as Air Force personnel were exposed to lower frequency, higher amplitude vibrations from jet propulsion systems that were increasingly more powerful and from manned space travel, especially the re-entry phase. They measured strain [8], internal pressure [5], and visual acuity [7]. They also performed a study focused on the effect of the duration of exposure to vibration [2]. As with most of the studies done in air with the purpose of investigating vehicle vibration, all of these

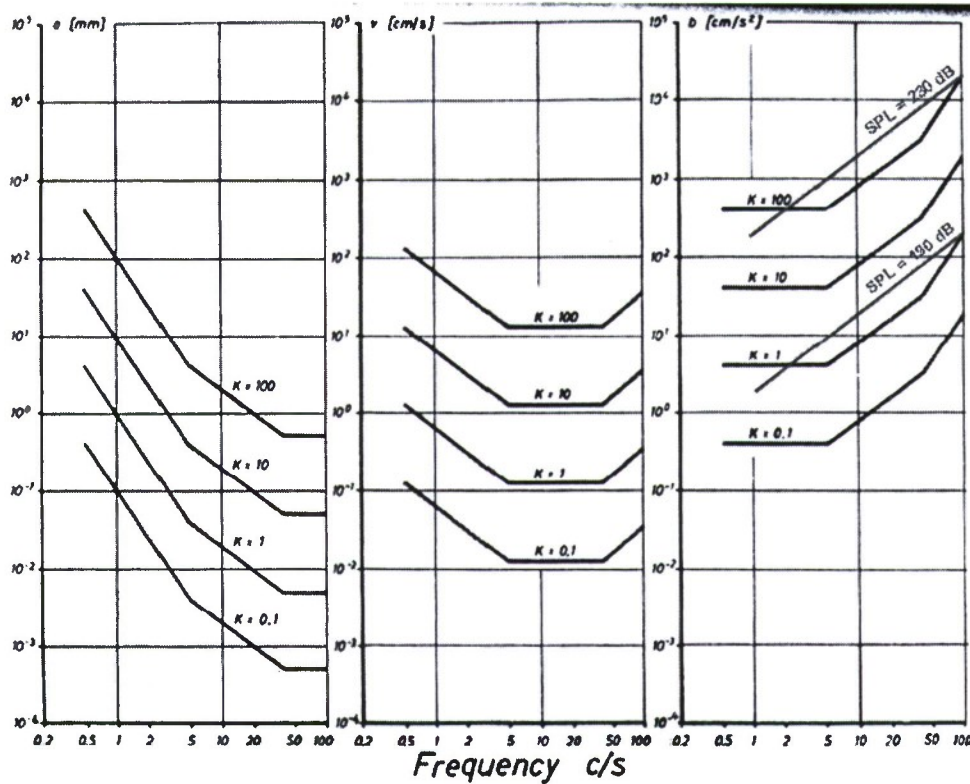


Figure 3. Scale of strain for vertical vibrations.

Figure 2.1: Dieckmann's K -scale for vertical vibration with underwater sound field input accelerations added by present author in red [28].

studies cover only frequencies below 20 Hz, because it is understood that mechanical damping systems can be used to protect operators against vibrations above 20 Hz. Although these frequencies are not in the range of interest, the exposure duration experiment can be of use.

The exposure duration experiment was conducted with sinusoidal vibrations created by a shake table and a vertical accelerator. The seated subjects were vibrated at a given frequency with increasing amplitude until their tolerance level was reached, at which point the subject pushed a button to stop the vibration. The authors stress that the subjects were not stopping the vibration at discomfort level, but at a point where they thought actual bodily harm might occur. In this way,

a tolerance acceleration amplitude was obtained for each frequency for short times, one minute and three minute durations. The results are given in Fig. 2.2, again with

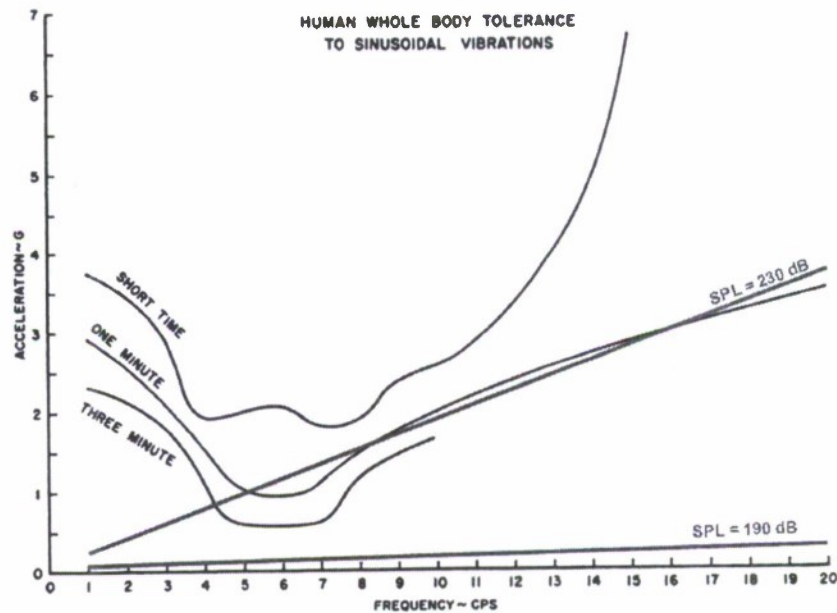


Figure 2.2: Results of vibration duration experiments with underwater sound field input accelerations in red. After Magid et al. [2], with red lines added by present author.

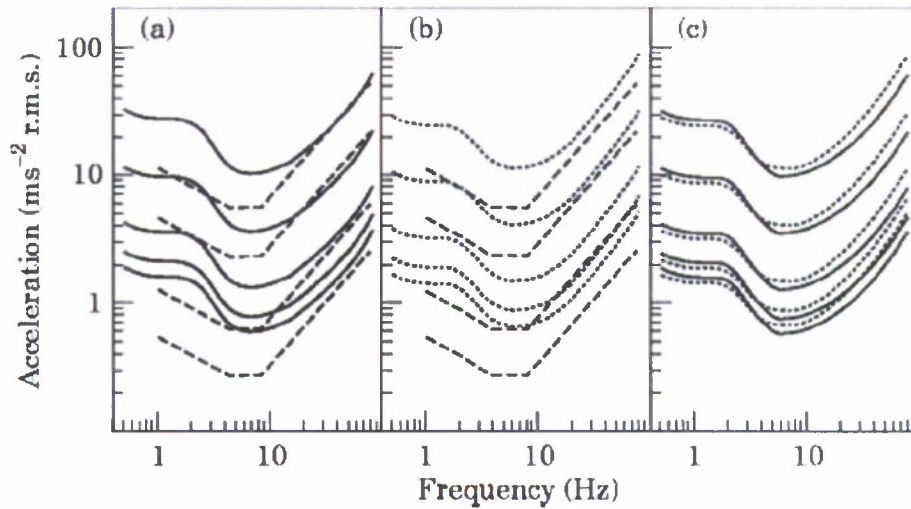
the input from the sound field at 190 dB and 230 dB added by the present author. Here, the 230 dB input is above the one-minute tolerance, and it appears that it might stay above it if the tolerance curve were extrapolated to higher frequencies. The 190 dB input is well below the tolerance level for any duration.

2.2 Standards

There are two main standards that set guidelines for vibration exposure in air. The first is the international standard ISO 2631, "Mechanical Vibration and Shock Evaluation of Human Exposure to Whole-Body Vibration. Part 1: General Re-

quirements,” and the second is the British standard BS 6841 “Measurement and Evaluation of Human Exposure to Whole-Body Vibration.” Michael J. Griffin, head of the Human Factors Research Unit at the Institute for Sound and Vibration Research and author of the *Handbook of Human Vibration* [20], has very strong opinions about these two standards. In his paper “A comparison of standardized methods for predicting the hazards of whole-body vibration and repeated shocks” [22] he describes and compares the two standards, discussing the historical progression and validity of each. Griffin’s paper stresses the fact that there is error in both the measurement and evaluation of human exposure to vibration. Standards do not define a way to report the type of evaluation method used for a particular case, and even within a particular method, there are discrepancies over acceptable levels of vibration. Evaluation of whole-body vibration is inexact at best and effects of vibration vary from person to person, so there is no way to know the exact consequences of vibration exposure. Figure 2.3 is a comparison of some vibration thresholds presented in the two standards from Griffin’s paper.

The original version of ISO 2631 dates back to 1974, and the most recent version was published in 1997. The first working group, convened in 1964, prioritized the definition of acceptable limits of exposure for industry, transportation, and residential premises [29]. Many of the conclusions originally drawn were based on Dieckmann’s work with strain curves [28]; however, the lack of consistent data and the fact that exposure time was not taken into account in Dieckmann’s study made it difficult for the group to agree on appropriate exposure limits. After subsequent meetings and additional measurements, the committee released the 1974 version, with exposure limits for the frequency range between 1 and 80 Hz. Griffin criticizes the early versions because of a complex exposure-time dependence, some unrealistic restrictions, and a contradictory calculation method. After an intermediate version and many improvements, the current standard includes both root mean square (rms)



Key: ---, ISO 2631 (1985); —, BS6841 (1987); ····, ISO 2631 (1997).

Figure 2.3: Griffin's comparison of vertical vibration limits: (a) ISO 2631 (1985) versus BS 6841 (1987); (b) ISO 2631 (1985) versus ISO 2631 (1997); (c) BS 6841 (1987) versus ISO 2631 (1997). Curves of decreasing amplitude, shown for 1 s, 1 min, 1 h, 8 h, 24 h, respectively. From Griffin [22].

and vibration dose value evaluation methods. Although the two methods allow for more accurate evaluation of vibration, Griffin still criticizes the latest version, saying that there is confusion about when to implement the different methods.

The basic vibration evaluation method described in the different versions of ISO 2631 did not change, and involves the calculation of the rms amplitude with exposure limits presented as a function of frequency and rms acceleration. The boundaries incorporate a frequency weighting system based on measured equal comfort contours. In particular, the standard presents a "reduced comfort boundary", a "fatigue, decreased proficiency boundary" (FDP) and an "exposure limit" for several different exposure times. Figure 2.4 shows the latter two limits at an exposure time of 1 minute, which is the shortest presented in the standard, plotted with the input rms accelerations due to the underwater sound field at 190 and 230 dB. As the plot

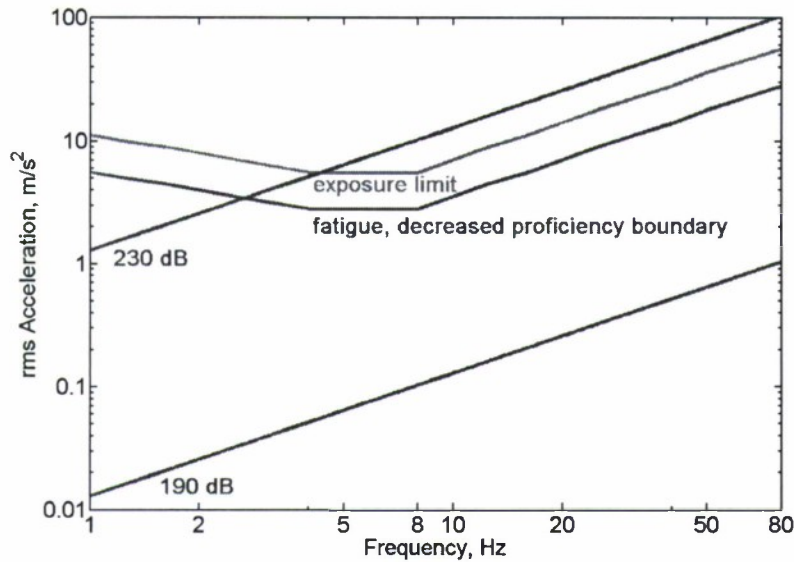


Figure 2.4: ISO 2631 limits for 1 minute exposure time with underwater sound field input accelerations.

shows, in the 40-80 Hz frequency range, 230 dB is above the exposure limit while 190 dB doesn't pass the FDP boundary. Further calculation shows that in order to exceed the FDP boundary at frequencies above 8 Hz, 219 dB must be achieved, and in order to pass the exposure limit above 8 Hz, 225 dB must be achieved.

The British Standard also uses weighted rms amplitudes for the primary vibration evaluation method, but for larger or variable vibrations it advocates the use of the vibration dose value (VDV), which uses a fourth root instead of a square root in the time dependence. This gives more reasonable results for both long and short exposure durations, with a simpler overall process. The standard states that it is impossible to specify the probability of injury for a certain amount of vibration, but claims that vibration dose values of 15 will usually cause severe discomfort, and increased exposure will cause increased risk of injury. Figure 2.5 shows a frequency and acceleration plot for a VDV of 15 for two different exposure times, one minute and one second, along with the 190 and 230 dB sound field accelerations. The plot

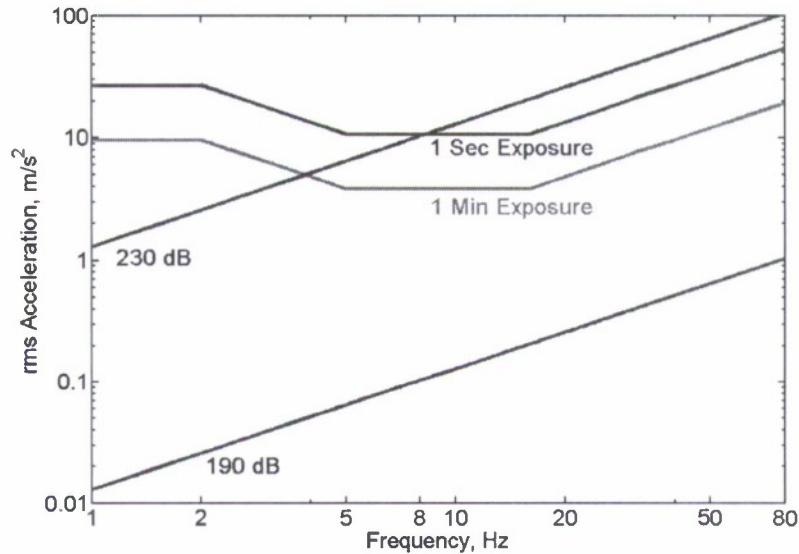


Figure 2.5: Accelerations Corresponding to a VDV of 15 as in BS 6841.

shows that 190 dB is not even close to the VDV of 15 for a one minute exposure time, and in order to exceed the limit for one second at frequencies above 8 Hz, it can be calculated that at least 225 dB is needed.

2.3 Other Negative Effects

The above standards exist mainly to set limits for everyday situations, and the “absolute limit” should be interpreted accordingly. Exposure to vibration has killed mice, rats, cats, and monkeys, and there is no reason to believe that it could not kill humans as well (e.g., see [30] for an experiment involving cats). The one instance found by the author of an intense reaction in a human was reported by Griffin [20], in which gastrointestinal bleeding occurred after vibration of 10g at 25 Hz. Exposure to vibration in the 15 to 25 Hz frequency range kills mice, and it is believed that the most severe effects in humans would occur at a lower frequency due to increased

visceral masses in humans, so severe effects are not likely to happen in the frequency range of interest (40–80 Hz) [4]. Similarly, another negative effect of whole-body vibration, motion sickness, is well understood to be a phenomenon that occurs at frequencies of vibration below 1 Hz, and therefore would not occur in the frequency range considered for this paper [31].

Exposure to vibration may also affect the extent to which people are able to carry out tasks, and there are several studies on the effect of vibration on the performance of tasks [6, 32]. Usually, subjects are required to perform a task, such as writing or controlling their movements, while being vibrated at various frequencies and amplitudes. Most of the studies are concerned with vehicle vibration, and only include frequencies below 20 Hz, so no conclusions can be drawn that apply to the frequency range of interest. In addition, the type and complexity of necessary tasks as well as the amount of practice the diver has in performing the tasks are important factors that will remain unknown in the context of a deterrent device.

The effect of vibration on vision is another factor that has been studied extensively [7, 19]. One way that visual acuity, the ability to visually resolve separate objects, is tested by finding out how far apart lines need to be in order for a subject to tell that there are two lines. In general, a decrease in visual acuity is caused by vibratory motion of the retinal image. This can be caused by either object vibration or whole-body vibration; during whole-body vibration these motions are due to differences between the eyeball and head vibration. Figure 2.6 shows a blur line that was measured by Griffin. The blur line is where objects can no longer be visually resolved, and the blur line for when the subject is being vibrated is labeled ‘vertical subject vibration’ on the plot, which also includes the 190 and 230 dB input acceleration lines and FDP boundaries from ISO 2631 are also included in the plot.

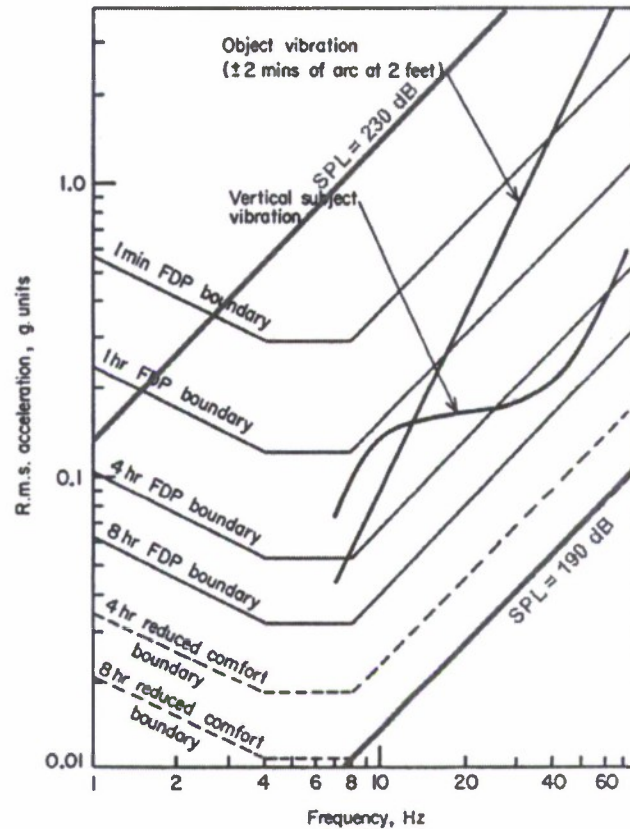


Figure 2.6: Griffin's visual acuity guidelines [19]. Red lines added by present author.

2.4 Summary

Presented in this chapter is an overview of some results of whole-body vibration experiments. In general, results are inconsistent and inconclusive, and it is very hard to draw any concrete conclusions about the effects of the underwater sound field. Many of the experiments or interesting results of experiments occur in a lower frequency range than that considered for this paper. From the two standards considered, ISO 2631 and BS 6841, there are boundary lines that can be applied to the vibrations experienced by a diver in the underwater sound field. The general conclusion seems to be that achieving an SPL of 190 dB would be right on the

border of the limits, possibly causing decreased proficiency, while higher SPLs will have greater effects. If an SPL closer to 230 dB, the threshold of cavitation, could be reached, exposure limits in the standards would be exceeded.

It is important, however, to put these conclusions in the context of a deterrent device. The standards used were created to set limits for everyday exposure to vibration in homes and workplaces. In the more extreme situation of a diver that has a specific and serious purpose, it should be assumed that it would take a much more intense experience to cause deterrence. Similarly, although the diver will most likely have blurred vision, this will probably not be a reason for the diver to stop their task or surface. The one thing that may be advantageous is the general unease the diver would experience as a result of feeling vibration or having blurred vision and not knowing the cause. During manned dive sonar studies performed by the Defense Research Agency in the U.K., some of the divers' subjective comments indicate that low frequency sonar exposure might be startling or disturbing for a diver that is unaware of the existence of low frequency sonar or unfamiliar with its effects [33]. Although there is no way of knowing if this would be an effective deterrent, it is possible that the surprise and alarm would surpass the negative physiological effects discussed above as the worst effect of low frequency sonar.

Chapter 3

Compilation of Whole-Body Vibration Models

Another way to understand the effects of whole-body vibration is to use models of the human body to predict what will happen to different body parts when exposed to whole-body vibration. The models shown in this paper are lumped element mechanical models that represent different parts of the body as systems of masses, springs, and dampers. Several models have been proposed based on experimental data for whole-body vibration in air, which can then be adapted to account for changes due to the underwater environment. This chapter lists all models found by the author and details the original purposes of the models and the probable relevance to the project.

When using whole-body vibration models there is opportunity to make adjustments to the models in order to take the underwater environment into consideration. However, these changes may or may not make accurate predictions for the body's response in water, and there is no way of knowing if the changes are accurate because there are not comparable experiments performed underwater. Also, similarly to the previous section, most of the data on which the models are based are for

frequencies under 20 Hz, so there is little known about the accuracy of the models in the frequency range of interest. Finally, problems arise because the results from the models are motions of individual organs, and the author has been unable to find any information on injury criteria for individual organs.

3.1 Seated Subjects

The most simple model created is the Dynamic Response Index (DRI) model, shown in Figure 3.1. It consists of one mass-spring-damper system, and is used to predict

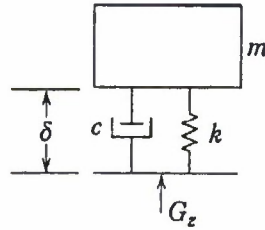


Figure 3.1: Dynamic Response Index model. After von Gierke [17].

probability of spinal injury [17]. It was originally developed in the context of predicting impact load from a seat ejection system. It was created by comparing operational injury data to predicted severity, and it accurately predicts the severity of spinal injury. This simple model is not relevant to the present project because there is no expected spinal injury. The whole-body vibration excitation for a neutrally buoyant diver is not necessarily going to be at the ‘seat’, but will be applied to the entire body, and will not create significant stress on the spine. It is the response of the inner organs that will be more relevant to simulate.

Many models of seated subjects were compiled by Liang and Chiang in a paper entitled “A study on biodynamic models of seated human subjects exposed to vertical vibration” [34]. The purpose of the paper was to gather and investigate

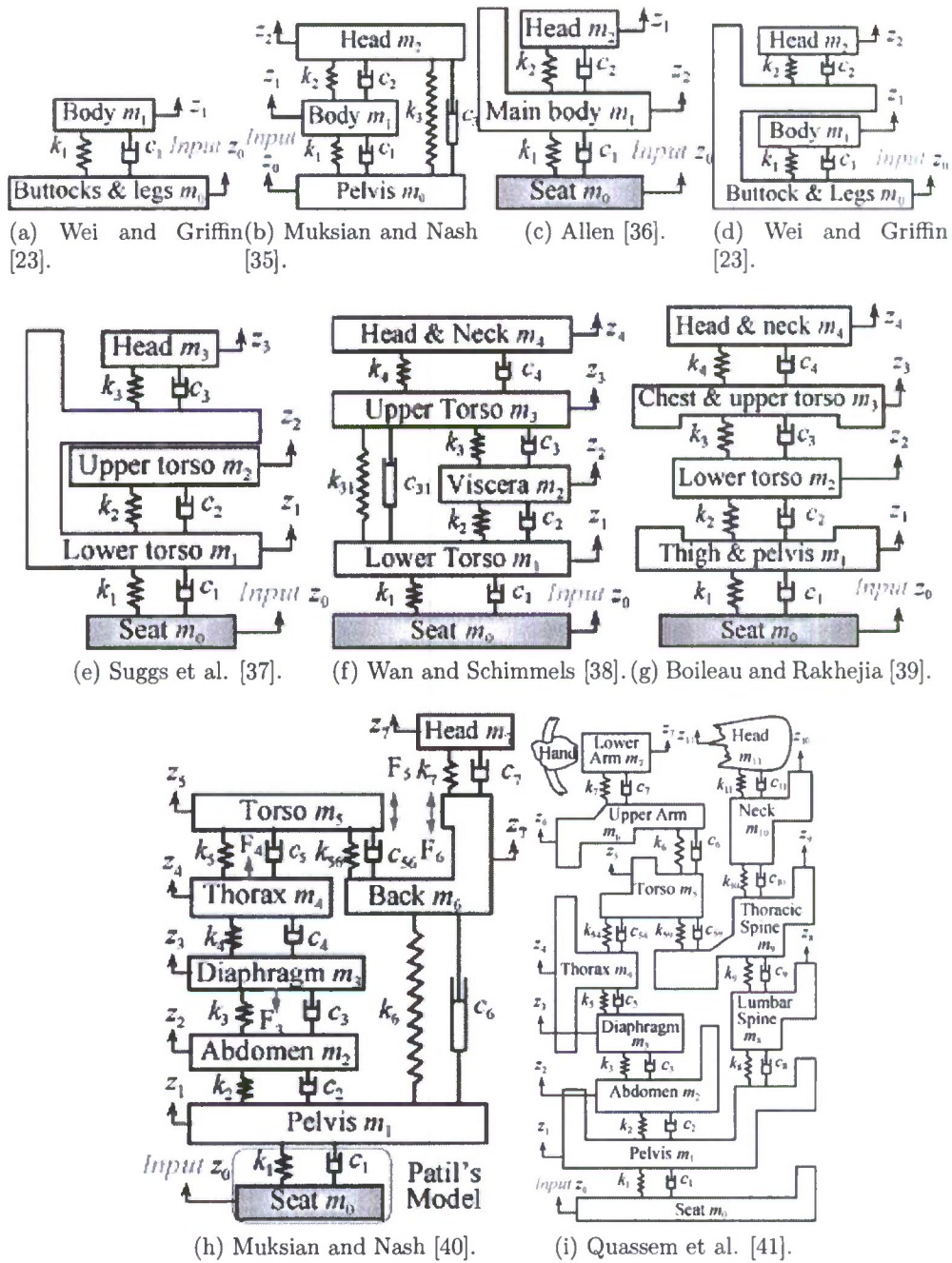


Figure 3.2: Models from Liang and Chiang's compilation [34]. References in individual labels cite the original work used by Liang and Chiang.

mathematical models of humans in the seated posture that had been proposed in earlier literature. After finding the models shown in Figure 3.2, the authors analyzed the models and compared the results to a synthesis of several experimental data sets. On the basis of seat-to-head transmissibility, driving-point mechanical impedance, and apparent mass, the authors validated the analytical models with experimental results, and concluded that the four-degree-of-freedom (DOF) model by Wan and Schimmels [38], Figure 3.2(f), best fit the experimental results. They also suggest the use of the six-DOF model by Muksian and Nash [40], Figure 3.2(h), if more mass segments are needed for analysis. For studying the effects of whole-body vibration in the underwater sound field, as stated earlier, it is important to use models based on human anatomy, so there are some models that are obviously not relevant. Models with less than four degrees of freedom, models (a) through (e) in Figure 3.2, are not anatomically based, and do not include enough detail to be relevant. Therefore, for this project, the relevant models are models (f), (g), (h), and (i), keeping in mind that (f) and (h) were found to best match experimental data.

Another model of a seated subject was created by Mertens [42] to study the behavior of humans under increasing gravity. The focus of the paper is on the non-linear behavior of the body as gravity increases, and involves measurements taken under increasing gravity. The effect of gravity is apparent in changes of the mass, spring and damper values of the model, and the paper includes these parameter values for the model subject to gravity forces of $1g$, $2g$, $3g$, and $4g$. Although created for this specific purpose, the model, shown in Figure 3.3, is still applicable to this project using the parameter values given for $1g$. The model has three spinal sections, and m_4 and m_6 are labeled as the abdomen and chest, respectively. It also includes a separate mass-spring-damper system for the leg, which will be ignored for the purposes of the present paper. The focus of the model seems to be the spine,

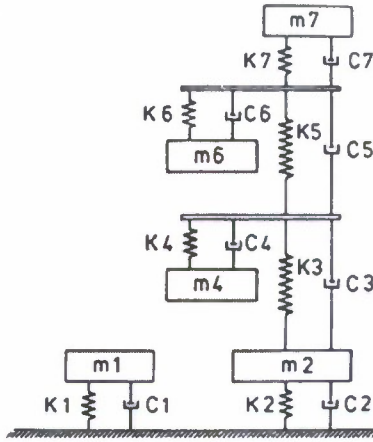


Figure 3.3: Mertens's model for seated subjects [42].

as opposed to central and internal body parts, but the inclusion of chest and abdominal properties makes the model more relevant than most of the models shown previously.

A final seated-subject model, created by Smith [43], was modified to be able to simulate the differences between different human body types, specifically between male and female. The model primary function of the model is to predict the effects of seat cushions on human body vibration response, focusing on the driving point impedance. The model is based on experimental data, and reproduces driving point impedance and chest transmissibility data. Shown in Figure 3.4, this model, like that in Figure 3.3, has a separate leg section that will be ignored, and includes spine, pelvis, and chest elements. The fact that the basis for the model is driving-point impedance is a sign that there is less emphasis placed on what is happening within the body than what is happening at the seat, which makes this model less applicable to finding the response to whole-body vibrations from the underwater sound field. However, the chest mass response will still be interesting to compare with other responses.

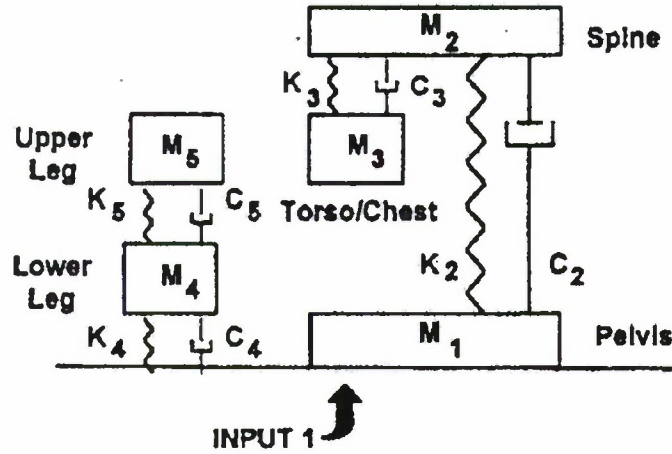


Figure 3.4: Smith's model for seated subjects [43].

3.2 Standing Subjects

Models for standing subjects have also been developed. One such model by Garg and Ross [44] is shown in Figure 3.5. Garg and Ross created this model in response to what they felt was a lack of complete models, with models that either do not resemble human anatomy or do not match human response data. Garg and Ross also believed much of the experimental data were inadequate, and performed their own measurements with a standing subject measuring feet-to-head transmissibility. The model created was first based on a simplified view of the construction of the human body that takes head rotation into account. Then, parameter values were varied until the frequency response of the model matched both the magnitude and phase of the frequency response data. Although Garg and Ross are very thorough in their development of the model, the model is less relevant for the purposes of this project because it is very detailed in the arms and legs, which are much less of a concern in the effects of the whole-body vibration from the underwater sound field, and lumps all of the internal organs together, which is where it is thought that injury would occur.

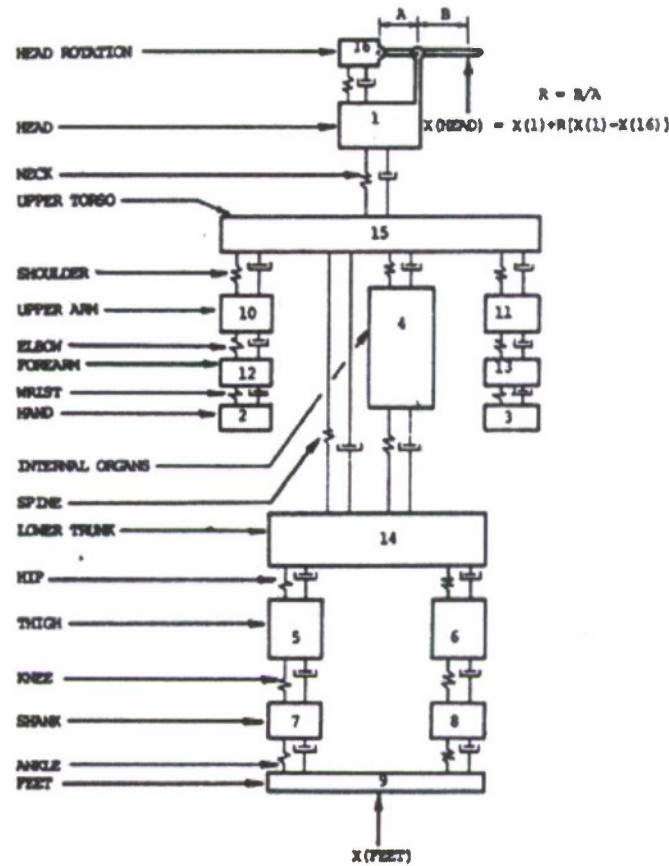


Figure 3.5: Garg's model for standing subjects [44].

Another model of a standing human was proposed by Gupta [45], who put an emphasis on the estimation of damping ratios in the model. The model, shown in Figure 3.6, was developed using anthropomorphic data and properties of bones and tissues, and then compared with experimental results after the parameters were already determined. Like the model in Figure 3.5, this model uses foot-to-head transmissibility data, and is less specific with what is occurring in between. The paper labels masses 5, 8, and 9 as upper, central, and lower torso, respectively, with no specific body parts mentioned. Thus, the model is not entirely relevant in the present paper.

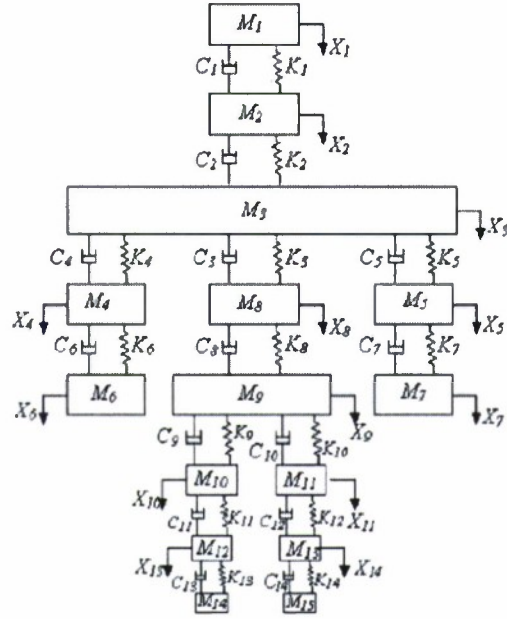


Figure 3.6: Standing model by Gupta [45].

A third model of a standing person was created to study the whole-body vibrations that occur during sports activities due to the impact of one foot hitting the ground [46]. The purpose of creating the model was to study the internal loads due to the ‘wobbling mass’, the mass that is contained within another mass in the model shown in Figure 3.7. The wobbling mass represents the non-rigid parts of the body, such as muscles, soft tissues, internal organs, and fluids, so again these elements are lumped together, and the model lacks relevant detail. However, it is assumed that in the whole-body vibrations from the sound field, it is the same wobbling mass that will be the most volatile area, so it is applicable to have a model focused on it.

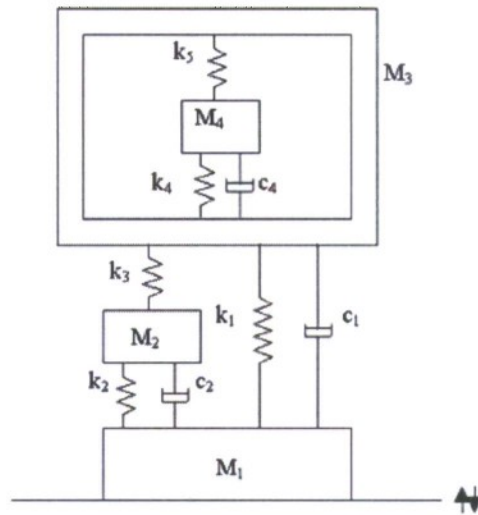


Figure 3.7: Yue and Mester's 'wobbling mass' model [46].

3.3 Models Including Lungs

A separate class of models may represent seated, standing, or supine subjects, but what sets them apart is that the models include fluid elements representing lung and airway properties along with mechanical elements representing other body parts. Because the frequency range of interest was chosen to include observed lung resonance, the inclusion of lung and airway elements is very relevant and interesting to this project. In addition, these models generally include a more detailed representation of the internal organs near the lung, where greatest discomfort is expected to occur due to relative motion, so it is possible to get a more detailed understanding of which parts of the body exhibit the most severe responses to whole-body vibration.

The first of these models was created by Henning von Gierke, former head of the Biodynamics and Bioengineering Division of the Armstrong Aerospace Medical Research Laboratory at Wright-Patterson Air Force Base. The model was created as an attempt to encompass different dynamic environments such as impact, vibration, blast, and acoustic excitations as well as demonstrating physiological accuracy

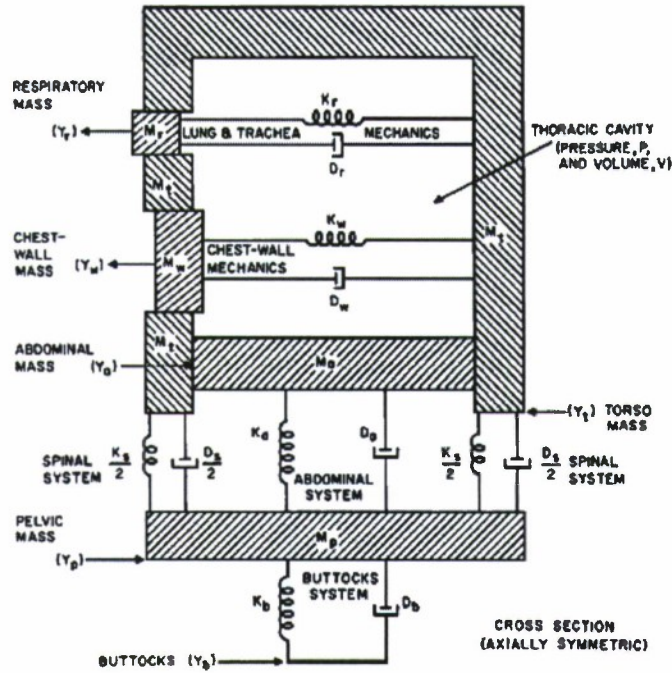


Figure 3.8: Five-degree-of-freedom model by von Gierke [15].

[15, 14]. The model is designed to combine the body's whole-body vibration response with spinal and abdominal injury, so it satisfies the basic spinal injury model, the thoracic-abdominal model, and whole-body impedance models with one set of parameter values. The model, shown in Figure 3.8, is a representation of the torso without arms, legs or head, which have secondary effects on the responses. This model can be considered as a model of a seated subject. The model includes the torso mass, which represents the loaded spine, the pelvis and abdomen, and the thorax. The thorax is simulated by an air-filled cavity with the abdomen, chest wall, and airway to the mouth coupled to the cavity. One important difference to note is that although the model is made for vertical vibration input, there are model elements that move horizontally, i.e., in the direction perpendicular to the excitation. This second dimension is possible because of the coupling of masses to

the chest cavity, and seems much more anatomically accurate. This model is the most relevant to the present thesis for all the reasons stated above and also because the model is easy to use, with given parameter values and plots of simulations for comparison.

A second model was also created by von Gierke [10], and has many similar properties to the above model, including a lung volume and chest wall perpendicular to the excitation direction, seen in Figure 3.9. The model, which can be modified

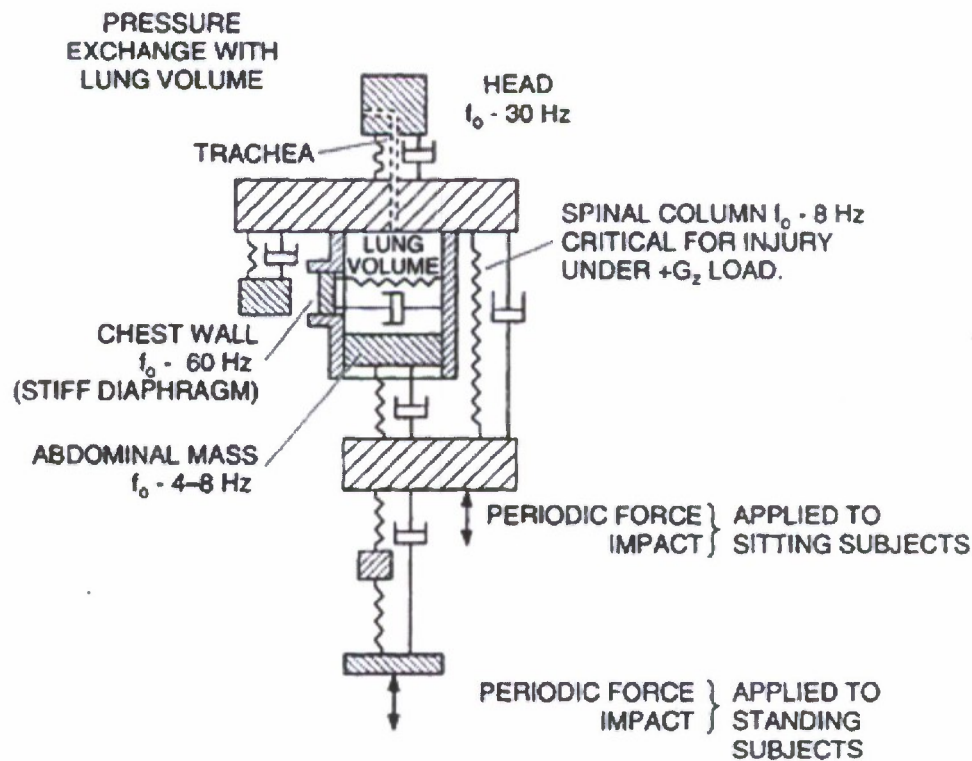


Figure 3.9: von Gierke's concept model [10].

for seated or standing subjects, is supposed to be another example of a way to combine the motions of the torso and spine with the motions of the abdomen and diaphragm in the thorax. This model was created as a concept model to demonstrate a possible configuration and to showcase the resonance frequencies that are labeled

in Figure 3.9. Therefore, parameter values were not found by the author and the model was not used to simulate any response plots.

The third and final model was created by Coermann et al. [3], who were colleagues of von Gierke. This model, in Figure 3.10, is a circuit model with different body parts represented by circuit elements. The model is one of four circuit models

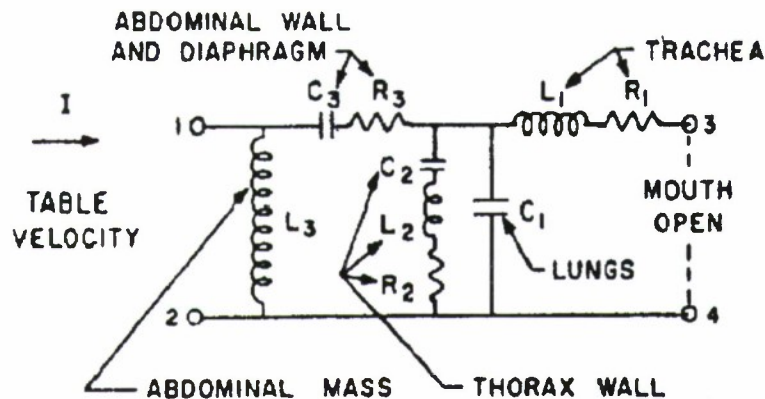


Figure 3.10: Circuit model of supine human. Adapted from Coermann et al. [3].

that were proposed in the same paper to model the thorax-abdomen system in different dynamic environments. This model is for vibration input to a person lying on his back and being vibrated in the head-to-foot direction. The other models developed by Coermann et al. represented oscillating or varying air pressure at different places in the body. The model parameters were extrapolated from measurements taken by accelerometers on the chest and abdomen, and a device to measure the airflow through the mouth. Since the model is specifically of the thorax-abdomen system, it includes only the abdomen, diaphragm, thorax/chest wall, lungs, and trachea. A drawback is that the parameter values are not given with the model, but it is implied that they can be found in other papers, and by extrapolating from resonances. This process is discussed further in Chapter 6. In some ways, this is the most relevant model because the supine position of the subject is most similar

to the input vibration from the sound field. However, the first von Gierke model, in Figure 3.8, includes more body parts and gives parameter values with the model, which eliminates one set of errors that could be made.

Chapter 4

Von Gierke's

Five-Degree-of-Freedom Model

The two most relevant models for the present study are the two that include properties of the lung and airways: the five-degree-of-freedom (5-DOF) model by von Gierke [15], and the circuit model by Coermann et al. [3]. The present chapter goes into the details of the work done by the author on von Gierke's model to adapt the model to the assumptions stated in the introduction. This includes changing model parameters and source placement on the model. In addition, results are obtained from the underwater sound field excitation. Responses from the other models in Chapter 3 will appear in subsequent chapters.

To recapitulate, von Gierke developed the five-degree-of-freedom model [15, 14] to simulate several sets of body response and injury data. The model, shown in Figure 4.1, includes the spine, pelvis, abdomen, and a thoracic cavity. There are several advantages to the model, the foremost being that parameter values for a 70 kg (154 lb) person are given and easy to use with the model. These parameter values are provided in Table 4.1. Additionally, the model gives a more detailed inner organ scheme than most other models found by the author, and the frequency response of

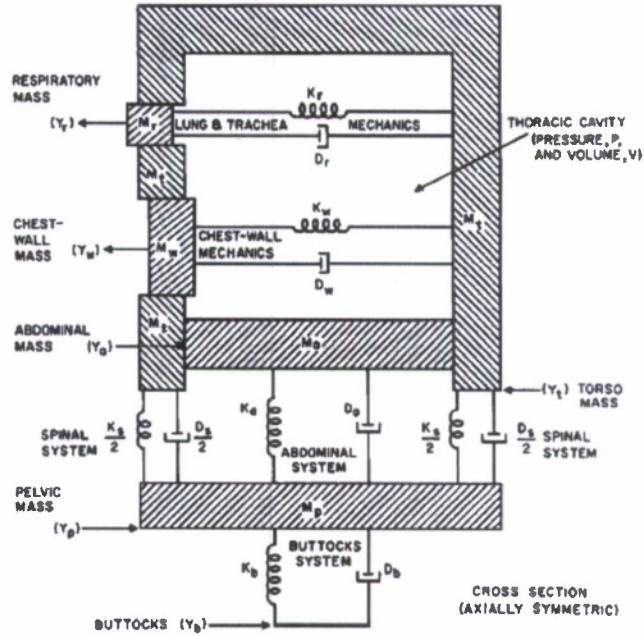


Figure 4.1: von Gierke's five-degree-of-freedom model [14].

the lung to vibration input can be found directly from the model equations.

4.1 Corroboration with Given Results

In order to use the model to simulate the biomechanical response to an underwater sound excitation, it is first necessary to derive the corresponding system of coupled first-order ordinary differential equations, or state equations, that govern the responses of the different model elements. This was done using a bond graph [47], which is a graphical description of a dynamical system that facilitates derivation of the state equations. The bond graph for the von Gierke model is shown in Figure 4.2. The symbols M , K , C , and D represent the mass, stiffness, compliance, and damping elements, respectively, that correspond to the elements in the mechanical model. The 0's are common force junctions, the 1's are common velocity junctions,

Parameter	Value (from von Gierke)	MKS Value
V_0	$4 \times 10^3 \text{ cm}^3$	0.004 m^3
A_R	2 cm^2	0.0002 m^2
M_R	$1 \times 10^{-1} \text{ g}$	0.0001 kg
D_R	$1.6 \times 10 \text{ dyne-s/cm}$	0.016 N-s/m
K_R	0 dyne/cm	0 N/m
A_W	$2 \times 10^2 \text{ cm}^2$	0.02 m^2
M_W	$1 \times 10^3 \text{ g}$	1 kg
D_W	$6 \times 10^5 \text{ dyne-s/cm}$	600 N-s/m
K_W	$1 \times 10^8 \text{ dyne/cm}$	10^5 N/m
A_A	$2 \times 10^2 \text{ cm}^2$	0.02 m^2
M_A	$4 \times 10^3 \text{ g}$	4 kg
D_A	$1 \times 10^4 \text{ dyne-s/cm}$	10 N-s/m
K_A	$8 \times 10^6 \text{ dyne/cm}$	$8,000 \text{ N/m}$
M_T	$4 \times 10^4 \text{ g}$	40 kg
D_T	$4 \times 10^6 \text{ dyne-s/cm}$	$4,000 \text{ N-s/m}$
K_T	$1 \times 10^9 \text{ dyne/cm}$	10^6 N/m
M_P	$8 \times 10^3 \text{ g}$	8 kg
D_B	$6.5 \times 10^5 \text{ dyne-s/cm}$	0.0065 N-s/m
K_B	$6 \times 10^7 \text{ dyne/cm}$	$60,000 \text{ N/m}$

Table 4.1: Table of parameter values for von Gierke’s 5-DOF model with 70 kg body mass [15].

and the TF’s are transformers that account for the areas (A ’s) of the mass elements in contact with the gas in the thoracic cavity. The sources are labeled S_v for velocity inputs (which will ultimately be specified in terms of acceleration or associated SPL) and S_F for force inputs. The source for von Gierke’s seated subjects is applied to the very bottom of the model at the buttocks spring and damper, and is included in the bond graph as the S_v on the 0 junction between the spring and damper connecting the buttocks and pelvis. This source is also referred to as u_{buttocks} . The sources used when the underwater sound field is the excitation are also included, although they are discussed in more detail in Section 4.3. These sources are the velocity (acceleration) inputs on the same 1 junctions as the torso mass and pelvic mass, which are referred to as u_{torso} and u_{pelvis} , respectively, and the force input on

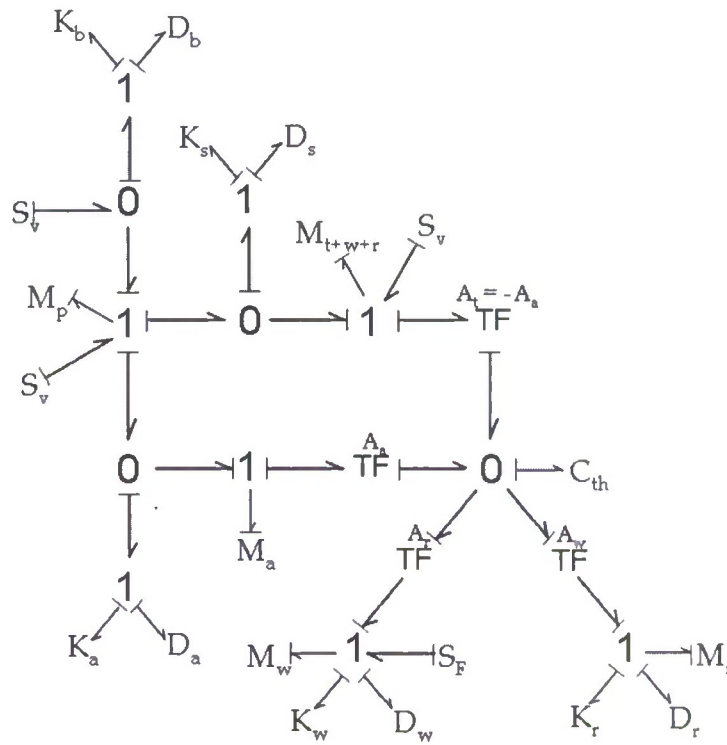


Figure 4.2: Bond graph for von Gierke's 5-DOF model.

the same 1 junction as the chest wall mass, which is referred to as F_{app} . Depending on what input is being used, the others can be zeroed out easily.

The state equations are written in the form

$$\dot{\mathbf{x}} = \mathbf{A} \cdot \mathbf{x} + \mathbf{b}. \quad (4.1)$$

The 11 elements of vector \mathbf{x} are

$$\left. \begin{aligned}
x_1 &= v_{M_a}, \text{ abdominal mass velocity} \\
x_2 &= x_{K_a}, \text{ abdominal spring displacement} \\
x_3 &= v_{M_w}, \text{ chest wall mass velocity} \\
x_4 &= x_{K_w}, \text{ chest wall spring displacement} \\
x_5 &= v_{M_r}, \text{ respiratory mass velocity} \\
x_6 &= x_{K_r}, \text{ respiratory spring displacement} \\
x_7 &= V_{C_{th}}, \text{ thoracic cavity volume} \\
x_8 &= v_{M_t}, \text{ torso mass velocity} \\
x_9 &= x_{K_s}, \text{ spinal spring displacement} \\
x_{10} &= v_{M_p}, \text{ pelvic mass velocity} \\
x_{11} &= x_{K_b}, \text{ buttocks spring displacement}
\end{aligned} \right\} \quad (4.2)$$

The 11 rows of the matrix \mathbf{A} are

$$\left. \begin{aligned}
a_{1n} &= [-D_a/M_a, K_a/M_a, 0, 0, 0, 0, -A_a/C_{th}M_a, 0, 0, D_a/M_a, 0] \\
a_{2n} &= [-1, 0, 0, 0, 0, 0, 0, 0, 0, 0, 0] \\
a_{3n} &= [0, 0, -D_w/M_w, -K_w/M_w, 0, 0, A_w/C_{th}M_w, 0, 0, 0, 0] \\
a_{4n} &= [0, 0, 1, 0, 0, 0, 0, 0, 0, 0, 0] \\
a_{5n} &= [0, 0, 0, 0, -D_r/M_r, -K_r/M_r, A_r/C_{th}M_r, 0, 0, 0, 0] \\
a_{6n} &= [0, 0, 0, 0, 1, 0, 0, 0, 0, 0, 0] \\
a_{7n} &= [-A_a, 0, A_w, 0, A_r, 0, 0, 0, 0, A_a, 0] \\
a_{8n} &= [0, 0, 0, 0, 0, 0, A_a/C_{th}M_t, -D_s/M_t, K_s/M_t, D_s/M_t, 0] \\
a_{9n} &= [0, 0, 0, 0, 0, 0, 0, -1, 0, 1, 0] \\
a_{10n} &= [D_a/M_p, -K_a/M_p, 0, 0, 0, 0, 0, D_s/M_p, \\
&\quad -K_s/M_p, -(D_b + D_s + D_a)/M_p, K_b/M_p] \\
a_{11n} &= [0, 0, 0, 0, 0, 0, 0, 0, 0, -1, 0]
\end{aligned} \right\} \quad (4.3)$$

For example, the notation a_{1n} in the first row is to be interpreted as $a_{11} = -D_a/M_a$, $a_{12} = K_a/M_a$, etc., for each element in that row. The input vector \mathbf{b} is

$$\mathbf{b} = \begin{bmatrix} (D_a/M_a)u_{\text{pelvis}} \\ u_{\text{pelvis}} \\ F_{\text{app}} \\ 0 \\ 0 \\ 0 \\ -A_a u_{\text{torso}} \\ 0 \\ u_{\text{torso}} + u_{\text{pelvis}} \\ (D_b/M_p)u_{\text{buttocks}} \\ u_{\text{buttocks}} \end{bmatrix} \quad (4.4)$$

It is assumed that the inputs are sinusoidal, and can thus be written in the form $\mathbf{b}(t) = \mathbf{B}e^{j\omega t}$. The solution will thus be of the form $\mathbf{x}(t) = \mathbf{X}(\omega)e^{j\omega t}$, which can be substituted into $\dot{\mathbf{x}} = \mathbf{A} \cdot \mathbf{x} + \mathbf{b}$ to obtain $(j\omega\mathbf{I} - \mathbf{A})\mathbf{X} = \mathbf{B}$. In this form, the magnitude of the response of different model elements as a function of frequency can be obtained using Cramer's rule; this was done using Matlab.

Shown in Figure 4.3(b) are responses obtained for the displacement of the abdomen and chest wall masses for a constant-velocity buttocks excitation. The responses of the same elements shown in Figure 4.3(a) were obtained by von Gierke [14]. Since von Gierke did not state the amplitude of the velocity source used, the responses plotted in Figure 4.3(b) are scaled to match the responses in Figure 4.3(a). In particular, it was necessary to scale the chest wall response by a factor of 45, but with no scaling factor on the abdomen response, in order for the relative amplitudes to agree with von Gierke. However, since von Gierke does not have a scale on the

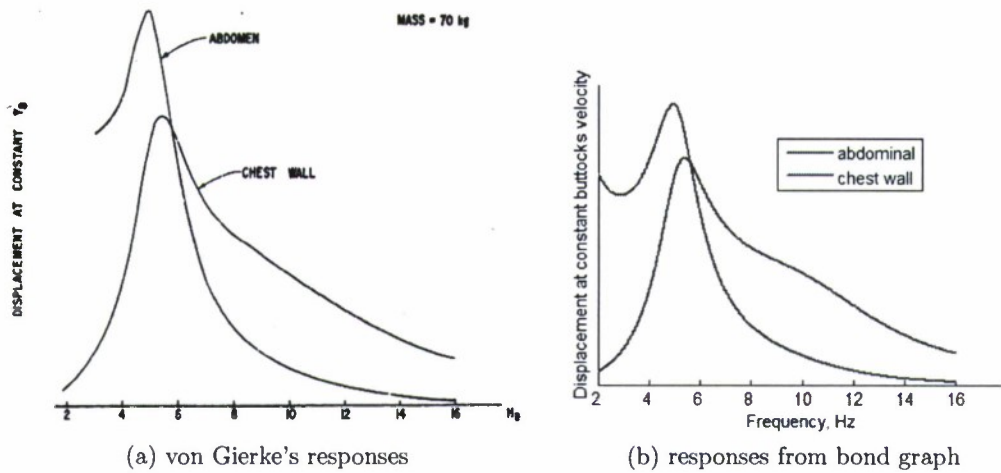


Figure 4.3: Comparison of abdomen and chest wall displacement responses due to constant velocity amplitude buttocks excitation for von Gierke's model. (a) after von Gierke [14], (b) calculations based on Equations (4.1)–(4.4).

y axis, given the otherwise good agreement with his responses, it is concluded that von Gierke also arbitrarily scaled his curves to fit on the same plot. Except for the abdominal response below 4 Hz, the responses match very well, verifying in the opinion of the author that the model is being interpreted as intended by von Gierke.

4.2 Adaptation for Underwater Environment

It is next necessary to make adjustments to the model for the premises of this project. Adjustments must comply with the assumptions stated in the Introduction and take into account the fact that the person the model is supposed to be representing is, under the circumstances, underwater. Recall the assumptions that the diver is neutrally buoyant, and thus does not experience any external forces besides those of the input, and that the diver is assumed to be horizontal with a sound wave propagating horizontally as the excitation. Under the assumption that the diver is horizontal, von Gierke's model is rotated 90 degrees, with the chest wall facing down.

In this position, the chest wall, as it is perpendicular to the rest of the elements, will be affected by gravity, and its spring will be stretched slightly. However, since the model is linear, this will not affect the responses.

Because the diver is in an underwater environment, there are two main modifications that must be made to the model. The first is to the compliance of the thoracic cavity, which changes with the depth of the diver. von Gierke simulates the thorax as an air-filled cavity, C_{th} , which is assumed to be primarily the air in the lungs. The compliance of an enclosed volume of air is $C = V/P$, where P is the pressure in the cavity and V is the volume of the cavity. V will be defined as $V = V_0$, the volume of the thoracic cavity at atmospheric pressure, which is given in Table 4.1. This volume will not change with depth because scuba gear is designed to keep the lungs at equilibrium pressure, so with the pressure in the cavity always the same as the pressure outside of the cavity, there is no volume change. However, as the diver depth h increases, the equilibrium pressure in the cavity increases by $\rho_0 gh$ over its value of P_0 at the surface, such that the pressure at depth is $P = P_0 + \rho_0 gh$. Thus the compliance of the thoracic cavity decreases to $C = V_0/(P_0 + \rho_0 gh)$.

The second change is an increase of the chest wall mass due to the inertial load of the water against the chest. This load should affect each external mass in the model, but as the torso and pelvic masses are both sources and the respiratory mass is interpreted as a slug of air rather than a skeletal mass element, only the chest wall mass is affected. This added mass was determined by approximating the thoracic cavity as a sphere and the chest wall a vibrating cap on the sphere. These assumptions are reasonable because the shape of a compact pulsating source is unimportant in the long wavelength limit. The reactance of the mechanical impedance seen by the vibrating cap, or piston, will be $j\omega M$, where M is the added mass due to the inertial load. The mass is determined by finding the mechanical impedance of such a piston, which is derived in Appendix A. The added mass is found to be

$M = \rho_0 S_{\text{cap}}^2 / 4\pi a$, where ρ_0 is the density of the surrounding fluid, a is the radius of the sphere, and S_{cap} is the surface area of the cap. Under the assumption that the thoracic cavity is a sphere with volume 0.004 m^3 (given in Table 4.1), the radius of the sphere must be 0.0985 m and the surface area must be 0.122 m^2 . A_W , the area of the chest wall from Table 4.1, is used for S_{cap} and the density of seawater, 1026 kg/m^3 for ρ_0 to calculate the added mass as 0.33 kg . Thus, the mass of the chest wall is increased from 1 kg to 1.33 kg .

4.3 Sources and Source Placement

After the above changes are made directly to the model to account for the effects of the diver being underwater, it is still necessary to look at other differences from von Gierke's conditions. The most important of these is understanding the nature of the vibration source. von Gierke based his model on data from seated subjects, and the vibration input for this situation is clearly a vertical displacement, velocity or acceleration, applied to the buttocks. However, under the assumption of a neutrally buoyant diver experiencing vibration from a sound wave propagating horizontally, it is not entirely clear where the source excitation should be applied. The diver does not have a specific point of contact with the source, but rather, the source is in contact with the entire outside of the body. Thus, it makes sense that the source should be applied to an 'outer' mass, meaning either the torso or pelvis or both, as these masses represent outer skeletal elements of the body. These options are explored by comparing frequency responses for the three source placement possibilities. Throughout this discussion, the kinematic vibration source is referred to as an acceleration source in order to be consistent with whole-body vibration literature. It is understood that the source used in the bond graph is a velocity source, but it is easy to go back and forth between velocity and acceleration with time-harmonic sources by multiplying by the angular frequency.

Another aspect of the input to consider is the acoustic pressure amplitude of the incident wave. The chest wall, as the smallest and most compliant mass element in the model, may be affected by the pressure, which would act as a force on the chest wall. Although this force is an important part of the complete effect of the sound wave, a force may not be an appropriate input for the model, which was made to simulate vertical vibration response data. Additionally, the purpose of the present work is to understand the response of the body to the vibration input from the fluid acceleration. With these considerations, the force input will be applied to the model along with the vibration sources to see what effect its inclusion will have.

In Figure 4.4, the frequency response of the abdominal mass acceleration with input vibration corresponding to 230 dB and with a diver depth of 0 m is used as an example to compare different source placements and the effect of including the applied force from the acoustic pressure of the wave on the chest wall. There are two sets of curves in the figure, each with three different source placement options: the vibration input can be on either the torso, the pelvis, or both. The unmarked lines are the responses from the three input options without the addition of the acoustic pressure on the chest wall, and the lines marked with plusses are the three input options with the addition of the pressure on the chest wall. First, it is observed that the addition of the pressure source completely dominates over the acceleration inputs. The three lines are indistinguishable, demonstrating that the different source placements do not generate different responses as they do without the pressure, and the response when the pressure source is included is significantly higher. Responses of the other model elements also show higher values with the pressure source applied along with the acceleration source. These results are consistent with the expectation that the acoustic pressure of the wave will have the greater effect, and be the mechanism responsible for any possible injury. Now, as the pressure dominates the response, it is necessary to ignore the pressure source in order to study the effects

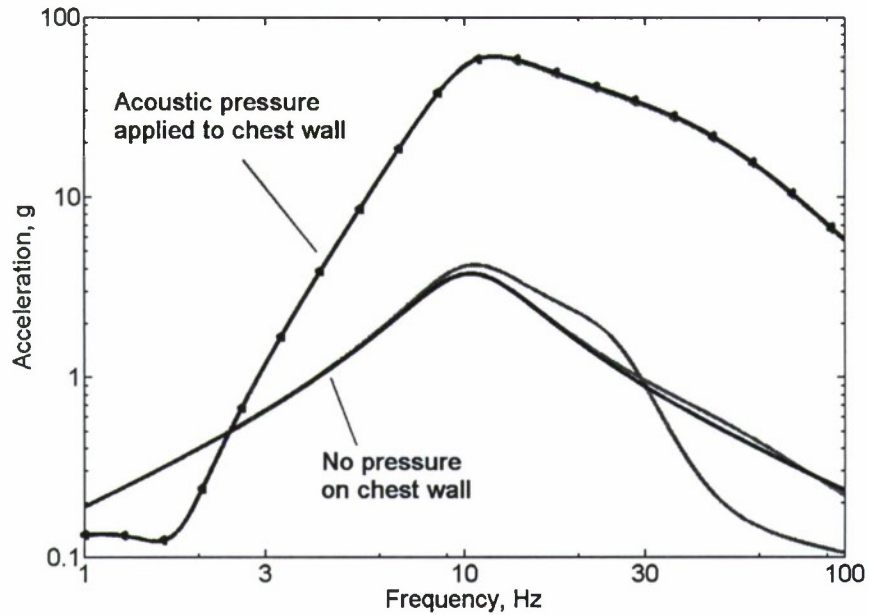


Figure 4.4: Abdominal mass acceleration response with input SPL of 230 dB and diver depth of 0 m. Two sets of curves are shown, one where the acoustic pressure is applied to the chest wall along with the acceleration source(s), and one with only the acceleration source(s) applied to the model. Each set has three acceleration source placement options: blue—source applied to torso alone, red—source applied to pelvis alone, and black—source applied to both torso and pelvis. The three curves are indistinguishable when the acoustic pressure is also applied as a source.

of whole-body vibration due to particle acceleration alone. Although it is clearly an important part of the complete response, the purpose of this project is to understand the response of the body due solely to the particle acceleration.

With the pressure source neglected, it is now important to note the differences in the responses for the different source placements. Specifically, the frequency response of the abdominal mass is the same when the acceleration source is applied to the torso alone and to the torso and pelvis simultaneously, and it is different only when the source is applied to the pelvis alone. The differences are not present at lower frequencies, and do not change the maximum value of the response, but in the

frequency range of interest, between 40 and 80 Hz, the response for the source on the pelvis alone is significantly lower than that for the source applied to the torso alone and to both the torso and pelvis. The responses with the source on the torso alone and on both the torso and pelvis together do not seem to be significantly different. This is most likely a result of the pelvis having a much smaller mass than the torso, making it easier for the torso to pull the pelvis along than the pelvis to pull the torso, especially at higher frequencies when the masses have higher accelerations. Because of these differences, it is concluded that applying the source to the pelvis alone is not the same as applying the vibration source 'everywhere' on the body, as assumed in this project. Since the difference between the responses with the source applied to the torso alone and to both the torso and pelvis is negligible, it is not crucial which one is used, but it makes the most physical sense to have the input on both the torso and pelvis, as these two masses are essentially a shell around the inner organs. Therefore, the input acceleration source will hereafter be applied to both the torso and pelvic mass elements equally and simultaneously.

Applying the source to the both the torso and pelvis introduces some simplifications to the bond graph and state equations discussed in Section 4.1. First, when the vibration source is applied to the pelvis and torso masses their motion is the input itself. Thus, these masses are no longer necessary in the system. Also, the buttocks spring and spinal spring become irrelevant. The spinal spring is only connected to the torso and the pelvis, so the entire system of the torso mass, pelvic mass, and spinal spring and damper will not have an independent response. The buttocks spring was included for seated subjects, but in this situation as it is only connected to the pelvis and does not affect the rest of the model, it becomes irrelevant. The reduced bond graph is shown in Figure 4.5.

The system is now seventh order, and the elements of the state variable vector are now

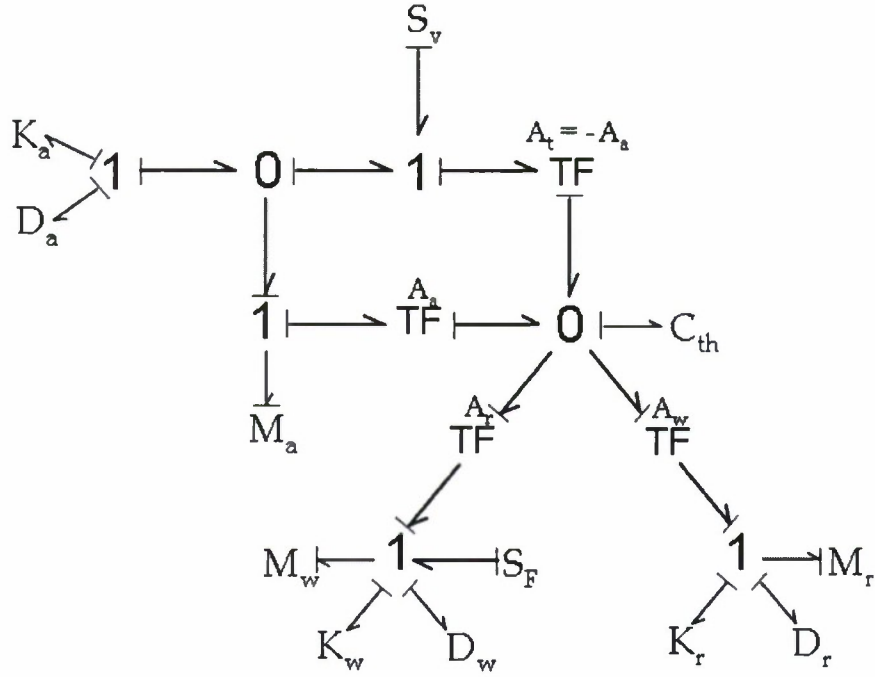


Figure 4.5: Reduced bond graph of von Gierke's model after source placement decisions were made.

$$\left. \begin{aligned}
 x_1 &= v_{M_a}, \text{ abdominal mass velocity} \\
 x_2 &= x_{K_a}, \text{ abdominal spring displacement} \\
 x_3 &= v_{M_w}, \text{ chest wall mass velocity} \\
 x_4 &= x_{K_w}, \text{ chest wall spring displacement} \\
 x_5 &= v_{M_r}, \text{ respiratory mass velocity} \\
 x_6 &= x_{K_r}, \text{ respiratory spring displacement} \\
 x_7 &= V_{C_{th}}, \text{ thoracic cavity volume}
 \end{aligned} \right\} \quad (4.5)$$

The matrix \mathbf{A} is

$$\mathbf{A} = \begin{bmatrix} -D_a/M_a & K_a/M_a & 0 & 0 & 0 & 0 & -A_a/C_{th}M_a \\ -1 & 0 & 0 & 0 & 0 & 0 & 0 \\ 0 & 0 & -D_w/M_w & -K_w/M_w & 0 & 0 & A_w/C_{th}M_w \\ 0 & 0 & 1 & 0 & 0 & 0 & 0 \\ 0 & 0 & 0 & 0 & -D_r/M_r & -K_r/M_r & A_r/C_{th}M_r \\ 0 & 0 & 0 & 0 & 1 & 0 & 0 \\ -A_a & 0 & A_w & 0 & A_r & 0 & 0 \end{bmatrix} \quad (4.6)$$

and the input vector \mathbf{b} is

$$\mathbf{b} = \begin{bmatrix} (D_a/M_a)u_{in} \\ u_{in} \\ F_{app} \\ 0 \\ 0 \\ 0 \\ -A_a u_{in} \end{bmatrix} \quad (4.7)$$

4.4 Lung Resonance

Using the reduced state equations given in Equations (4.4)–(4.6), the author is able to plot the predicted responses of the body elements in von Gierke's model. In particular, the response of the thoracic cavity, which is assumed to represent the change in lung volume, can be compared to measurements of lung resonance. Relevant measurements are found from experiments by Martin, Rogers, and Cudahy [1], in which they use a pool inside a hyperbaric chamber to simulate varying ambient pressure conditions and measure resonances of the water-loaded lung. Results from

their experiment are shown in Figure 4.6. The measurements show that at a depth

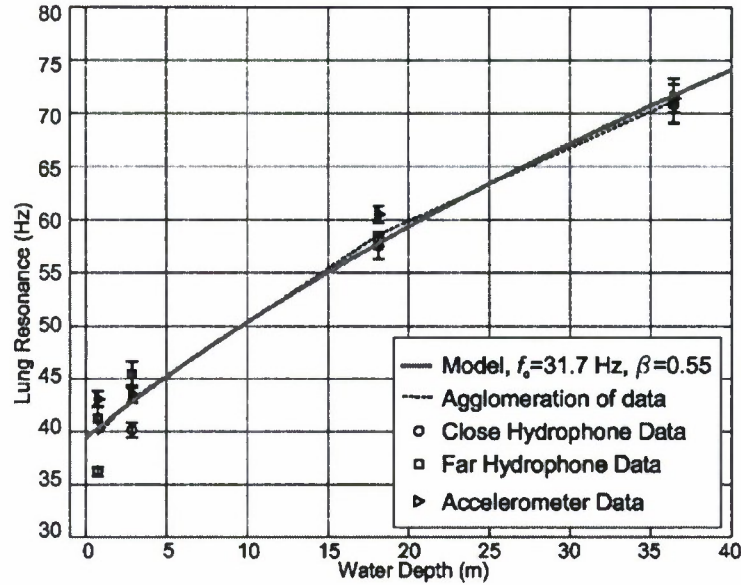


Figure 4.6: Experimental results for lung resonance as a function of water depth. After Martin et al. [1].

of 0 m the lung resonance is around 40 Hz, and at a depth of 36.4 m the lung resonance is around 71 Hz. Quality factors of these resonances are 1.8 for the resonance at 0 m and 2.5 for the resonance at 36 m. Figure 4.7 shows the response of the thoracic cavity predicted by the augmentation of von Gierke's model, in which the predicted resonances are approximately 11 Hz and 35 Hz at depths of 0 m and 36 m, respectively.

These predicted resonances are much lower than those measured by Martin et al., and the quality factors are 0.9 and 0.5 at 0 m and 36 m, respectively. In order to have the model fit the measured lung resonances, different numerical values of the parameters in Table 4.1 were considered. It turns out that the subsystem that affects the thoracic cavity response most is the abdomen, so changes in the abdominal mass, area, spring, and damper were made to adjust the cavity resonance. Figure 4.8 shows

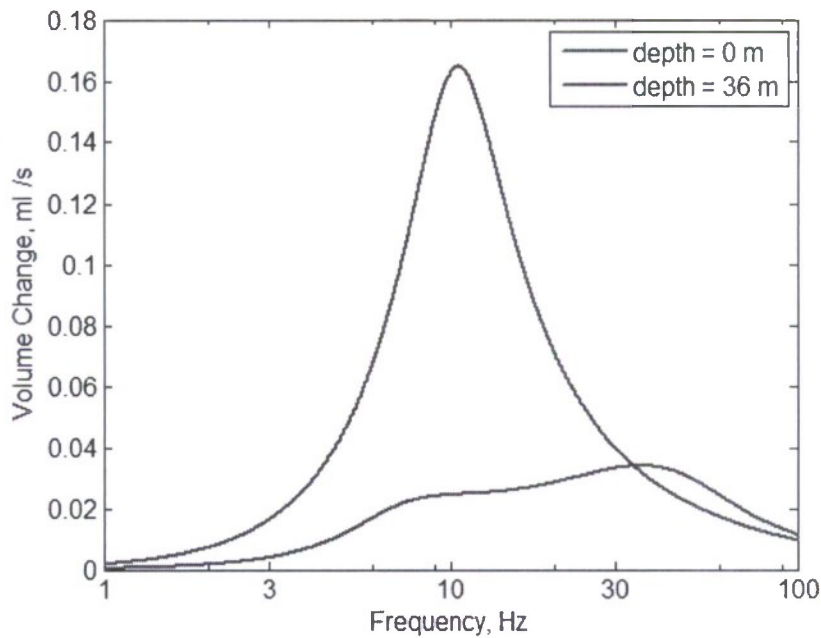


Figure 4.7: Thoracic cavity response from von Gierke's model at depths of 0 and 36 m.

the effects of changing either the abdominal mass or area to move the resonances closer to the measured values. Although these changes can increase the resonance frequencies, the separation of the resonance peaks is too wide for both peaks to be at the measured lung resonances simultaneously. However, increasing the abdominal spring stiffness moves these peaks closer together. In addition, the changes that move the resonances higher cause the quality factors of the resonances to increase dramatically, which must also be addressed.

Figure 4.9 shows the predicted thoracic cavity response from the combination of changes to the abdominal mass, area, and spring constant that optimize agreement of resonance frequencies with measurements. The optimal combination is an attempt to match the measured resonances as closely as possible while minimizing the change to each individual element. When the optimal parameters are used in the model, the

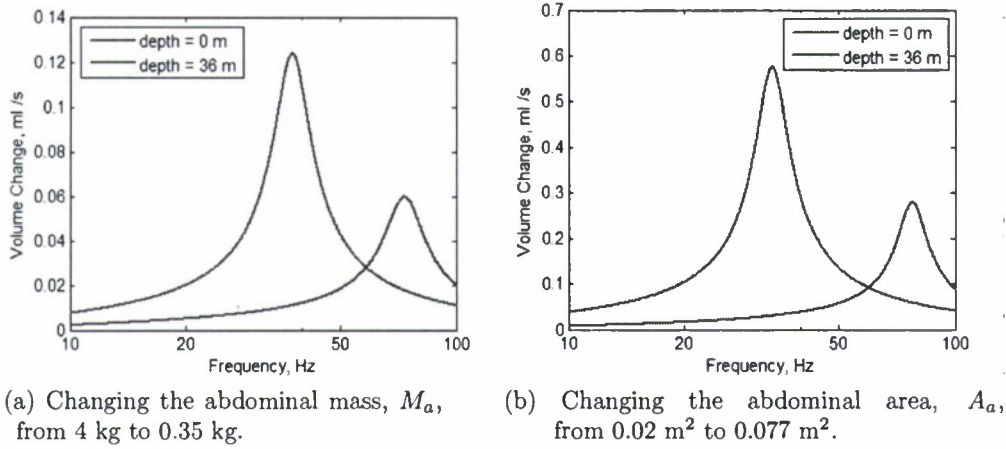


Figure 4.8: Possible changes to abdominal characteristics.

resonance frequencies are 40.6 Hz at 0 m and 71.8 Hz at 36 m. The quality factors for the resonances are 5.9 and 2.89 at 0 m and 36 m, respectively, but increasing the abdominal damping value from 10 N-s/m to 100 N-s/m brings them down to 2.2 and 2.1, which are more reasonable. The constants deemed optimal by the author are $M_a = 1.9$ kg, $A_a = 0.043$ m², $K_a = 70,000$ N/m, and $D_a = 100$ N-s/m; these values are used for the predicted thoracic cavity response shown in Figure 4.9.

It is important to keep the model physiologically realistic when varying parameters as described above. The abdominal mass should include all abdominal organs: the liver, kidneys, stomach, intestines, spleen, gallbladder, appendix, and pancreas. The masses of these individual organs added together should be at least 3.2 kg [48]. So, whereas an abdominal mass around 4 kg is reasonable, decreasing it below 2 kg is physically unrealistic for a standing mass. However, as a moving mass, it may not be true that each of the organs listed above moves together in the way that was modeled, and the actual moving mass may be lower than predicted by von Gierke. Increasing the contact area between the abdomen and the lungs from 0.02 to 0.043 m² corresponds to changing the portion of the lungs that is in contact

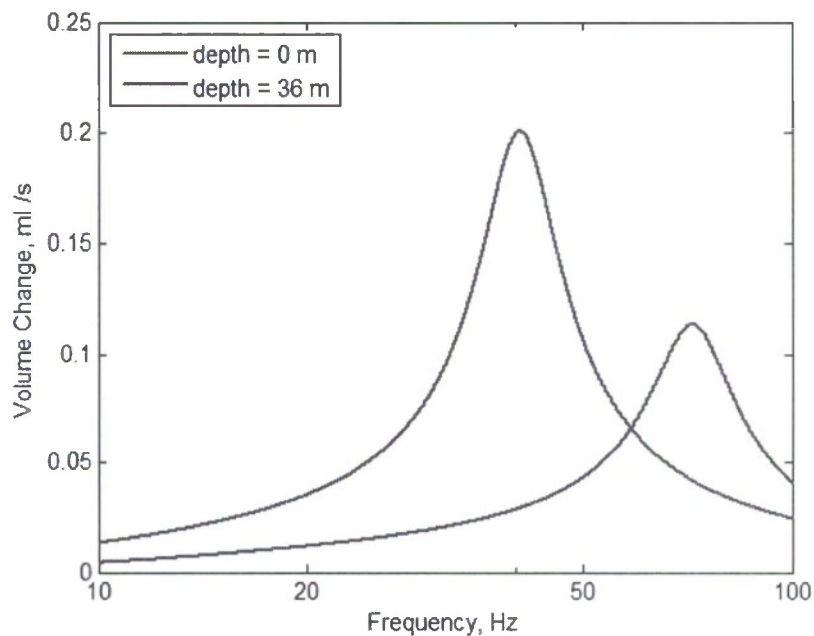


Figure 4.9: Thoracic cavity response from model with parameters optimized for agreement of predicted resonance frequencies with measurements by Martin et al. [1].

with the abdomen from a circle of diameter 16 cm to a circle of diameter 23 cm. Although a circle of diameter 23 cm seems large at the bottom of the lungs, the area of contact is not a flat circle, but more like a curved surface which might well have an even larger area in contact with the lungs. Increasing the parameters for both the spring and damper by a whole order of magnitude is also a large change. Although the changes made could be seen as physically inaccurate, it is impossible to know exactly what occurs within the body during vibration, and the changes proposed are not drastically unreasonable.

4.5 Results from the Model

As far as the author is aware, the previous sections have incorporated changes to the model that are necessary to accomodate the assumptions stated in the Introduction and further assumptions about this particular model. With these changes in place, frequency responses calculated for the acceleration, velocity, and displacment associated with each mass element in the model are shown in Figures 4.9–4.11, and the volume change response for the thoracic cavity is shown in Figure 4.12. Table 4.3 gives a summary of the maximum values for each element. The plots were made using Equations (4.5)–(4.7) with the acceleration source due to sound fields with sound pressure levels of either 190 or 230 dB applied to both the torso and pelvic masses. The diver depth for the plots is 20 m, which was taken into account in the stiffness of the lung cavity. Changes to the model parameters include an increase in the chest wall mass to account for the inertial load of the water against it and the changes made in the previous section to the abdominal elements, so that the lung resonance agrees with measured values. These changes are detailed in Table 4.2.

Parameter	von Gierke value	current value
M_W	1 kg	1.33 kg
A_A	0.02 m ²	0.043 m ²
M_A	4 kg	1.9 kg
D_A	10 N-s/m	100 N-s/m
K_A	8,000 N/m	70,000 N/m

Table 4.2: Table of parameter values for the 5-DOF model with 70 kg body mass [15].

The plots show that while each element has a slightly different frequency response, all of the elements have a resonance at approximately the same frequency as the lung resonance seen in the thoracic cavity response, which is around 60 Hz at a depth of 20 m. Also, the response generated from the input SPL of 230 dB is

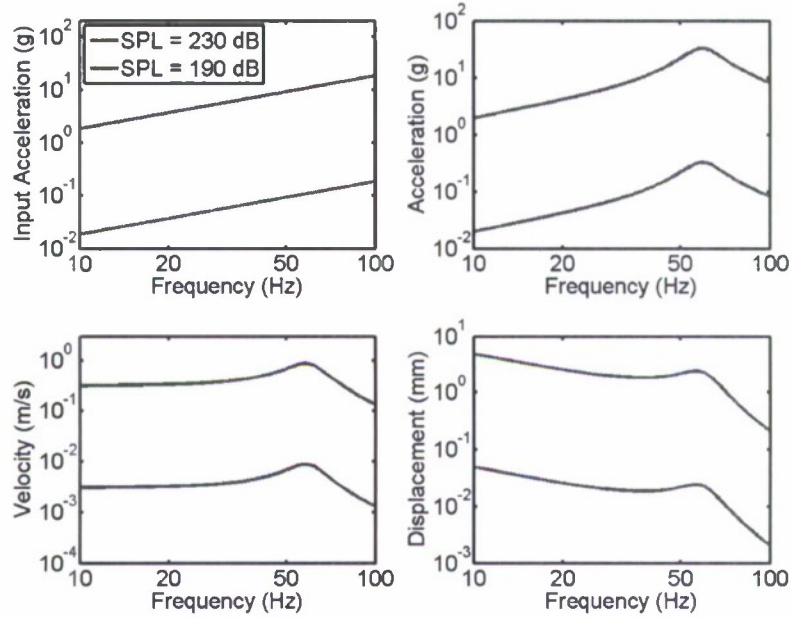


Figure 4.10: Response of the abdominal mass.

two orders of magnitude higher than that generated from the 190 dB input, which seems to be a significant difference when referring to organ motion within the body. It is, however, difficult to glean real meaning from these responses. For example, the response of the respiratory mass at resonance seems exceedingly high, but recall that the respiratory mass is not a mass element in the same way as the chest wall or torso, but the slug of air between the lungs and mouth. The displacement of this air at 13.8 cm is comparable to the length of the trachea, and is not unreasonably large. It is a reasonable assumption that air could move faster and farther than a skeletal mass element, so that the respiratory mass response does not seem so extreme.

As mentioned before, one of the problems with this method is that there is little means available for interpretation of the data. The author has not been able to find information on individual organ motion under either normal or extreme circumstances. Thus, more data are necessary on the motion of individual organs

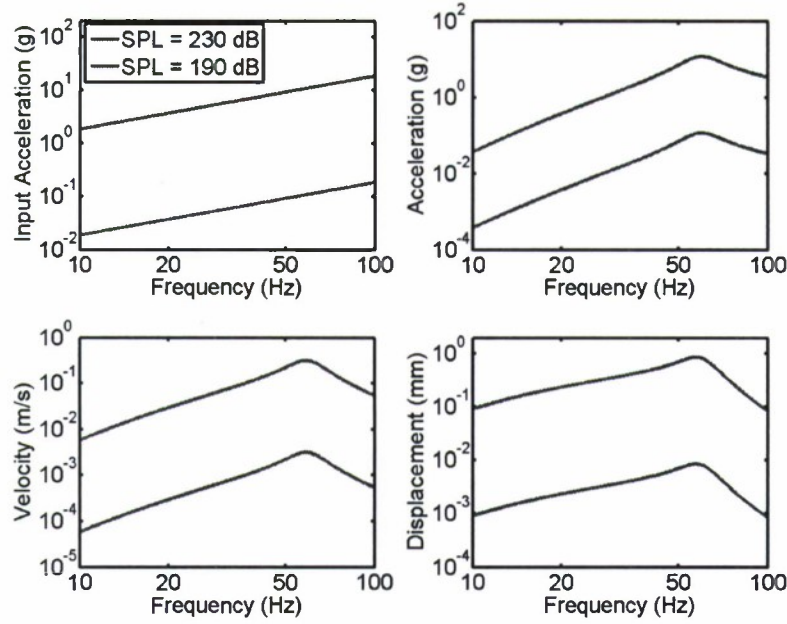


Figure 4.11: Response of the chest wall mass.

to conclude whether or not the fluid acceleration in the sound field is likely to cause significant discomfort, if not injury, at the sound pressure levels under consideration here. The maximum displacement of each element does not seem high enough to cause injury, but data on rats have shown that hemorrhaging occurs at an acoustic pressure of about 2 kPa [49], which, assuming a spherical lung, creates a radial strain of about 5%, while a mouse's breathing creates a strain of 25%. With these numbers, it is assumed that it is not strain alone, but rather rate of strain that will cause injury, so the maximum velocity or acceleration of the mass elements are the more important data.

One inference that can be drawn from the responses involves the relative amplitude of motion of one organ compared to those of others. In particular, note that the abdominal mass has a more severe response than the chest wall, from which a tentative conclusion can be drawn that any possible injury would occur around

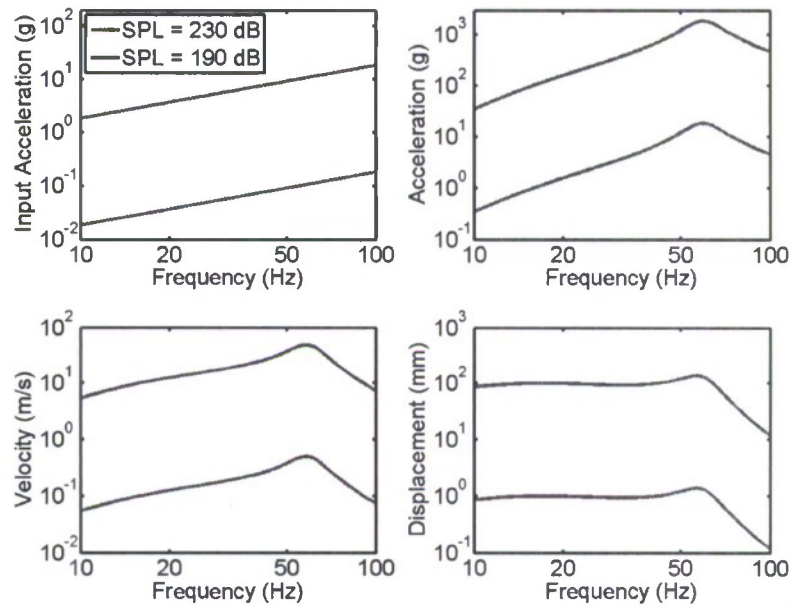


Figure 4.12: Response of the respiratory mass.

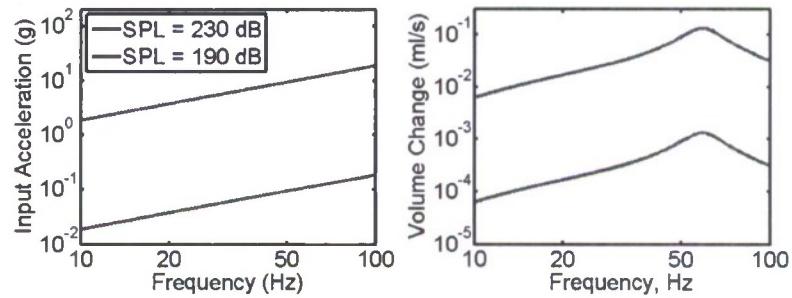


Figure 4.13: Response of the thoracic cavity.

the abdomen and the tips at the bottom of the lungs rather than in the middle of the lungs at the front of the body. Again, results of unpublished experiments on rats at The University of Rochester support this supposition, and have shown that damage to the lungs occurs most often at the tips.

Finally, if the pressure source on the chest wall is included as before to ob-

	Abdomen	Chest Wall	Respiratory	Thoracic Cavity
acceleration at 190 dB	0.33 <i>g</i>	0.12 <i>g</i>	18.72 <i>g</i>	Volume change at 190 dB is 0.00232 ml and volume change at 230 dB is 0.232 ml
acceleration at 230 dB	33 <i>g</i>	11.8 <i>g</i>	1872 <i>g</i>	
velocity at 190 dB	0.0088 m/s	0.0031 m/s	0.5 m/s	
velocity at 230 dB	0.88 m/s	0.31 m/s	50 m/s	
displacement at 190 dB	0.025 mm	0.0085 mm	1.38 mm	
displacement at 230 dB	2.46 mm	0.85 mm	138 mm	

Table 4.3: Maximum values for the response of mass elements and thoracic cavity to a sound field with SPL of 190 or 230 dB. The *g*'s appearing in the table represent the acceleration of gravity, 9.81 m/s²

tain the complete response, it is again clear that the acoustic pressure dominates the particle acceleration. Figure 4.13 shows the acceleration responses for the abdominal, chest wall, and respiratory masses and the volume change of the thoracic cavity with the pressure source included along with the acceleration source. The maximum responses with the inclusion of the pressure source are almost two orders of magnitude above those with the acceleration source alone. The resonances are generally not affected by the addition of the pressure source, so the lung resonance is still in the appropriate place. The maximum accelerations, now 715*g* and 7.15*g* for the abdominal mass at 190 dB and 230 dB, respectively, 8.9*g* and 890*g* for the chest wall (both now at 100 Hz instead of resonance), and 430*g* and 43,000*g* for the respiratory mass, seem very high. Although there is still no way to interpret these results, it seems much more likely that injury would occur at these levels, and it is a reasonable conclusion that the response due to the particle acceleration is sufficiently small, and dominated by the acoustic pressure, to assume that it will not be an important factor in the response of the human body to the underwater

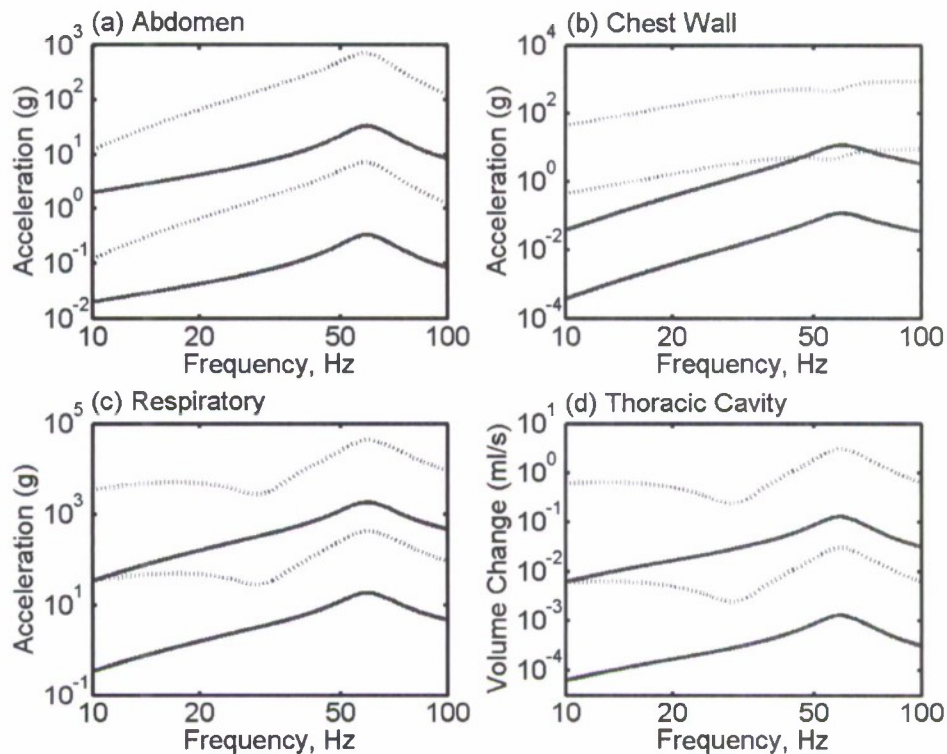


Figure 4.14: Responses with both acoustic pressure and particle acceleration applied as sources. Solid lines are with the particle acceleration input alone, and dotted lines are with both pressure and particle acceleration applied. Blue lines have an excitation source SPL of 230 dB and red lines have an excitation source SPL of 190 dB.

sound field.

4.6 Comparison to ISO 2631

Although there were no data on individual organ motion found to use in comparison with the predicted responses from the model, it is possible to use the International Standard 2631, discussed in Section 2.2, as a basis for comparison. This is done using the one-minute exposure limit for vertical vibration as an input for von Gierke's

model. Between 8 and 80 Hz, the exposure limit is linear with acceleration, and thus has a constant velocity which is calculated to be 0.1575 m/s. Because these standards are for vibration in air, the responses due to the ISO exposure limit are calculated using the unsimplified bond graph shown in Section 4.1, with the input on the buttocks system. In addition, the changes made to the model because the diver is underwater—the thoracic cavity stiffness increase and the chest wall mass loading—are not used. The changes made to the abdominal properties to adjust the lung resonance, however, are retained, as these were true changes to the model rather than adjustments for underwater effects. Then, the predicted responses of the abdomen and chest wall masses to the ISO exposure limit can be compared to the responses of the abdomen and chest wall masses to the underwater sound excitation, as shown in Figures 4.9 and 4.10. This comparison for the acceleration response of the two masses is shown in Figure 4.14.

It must be stressed that the international standard was not intended for this type of comparison. The standard sets limits for workplace and home environments, and the exposure times presented are for exposure within a twenty-four hour period. In the context of a diver deterrent, the diver will only be exposed to the sound for a minute or less before the desired effects should occur. However, as this is the only method found to give context to the calculated responses in Section 4.5, it will be considered.

This comparison shows that the response of the body to the underwater sound field as put forth in this thesis is much different than its response to vibrations in air. At 190 dB, the responses are well below the responses of the exposure limits in the low frequencies, but towards the lung resonance, the 190 dB responses do exceed the responses from the exposure limit. This shows the possibility that there will be an effect in the target frequency range of 40 to 80 Hz. The responses to the 230 dB input are well above the responses experienced by the body when exposed to

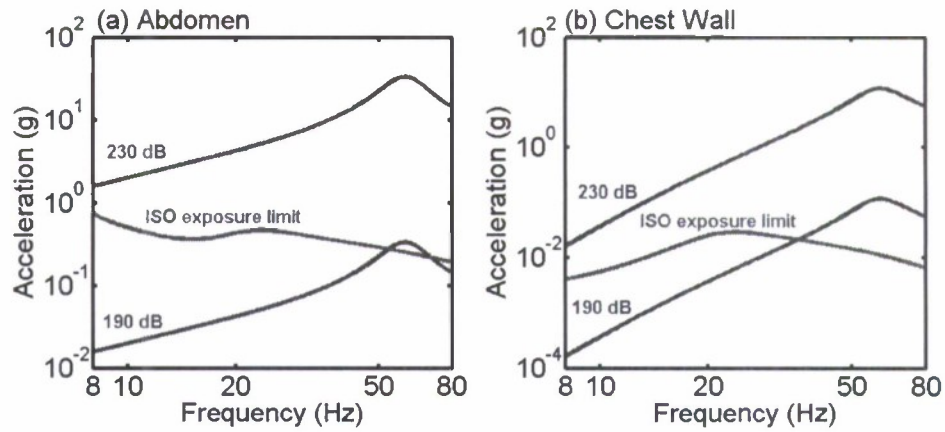


Figure 4.15: Acceleration responses of the abdomen and chest wall to input from ISO 2631 exposure limit compared with responses calculated in Section 4.5.

the exposure limit, which shows that if 230 dB can be achieved, the diver will most likely be affected by the wave. It is important to note that the accuracy of both the responses and limits in the 40–80 Hz range is questionable, as the author has not found any vibration experimentation done at frequencies above 20 Hz. Further experimentation would be necessary to draw any more concrete conclusions.

Chapter 5

Circuit Model of Coermann et al.

The circuit model of Coermann et al. [3], shown in Figure 3.10, is a model of a supine subject that includes lung and airways properties. Although the model includes fewer body parts than most of the other models, of all models that have been reviewed it takes into account the most assumptions stated in Chapter 1. With a supine subject, the organs within the body are oriented similarly to the way they would be in a horizontal diver, and the input is applied to the outer shell of the body, rather than just the feet or buttocks. This chapter details the methods used to find parameter values for the model and to obtain responses from the model.

In their discussion of the model, Coermann et al. [3] state that the thorax-abdomen system has been found to be of extreme if not vital importance with respect to the ability of the human body to tolerate vibration exposure. They proceed to take measurements focused on the thorax-abdomen system by measuring the air flow in and out of the mouth, the expansion of the chest wall, and the motion of the abdominal wall. The experimental setup is shown in Figure 5.1, and the frequency responses from the different measurements are shown in Figure 5.2. From these experimental results, Coermann et al. attempt to construct a model of the thorax-abdomen system that generates the measured response. The model they created is

shown in Figure 5.3 (same as Figure 3.10), and the frequency response of the model is shown in Figure 5.4.

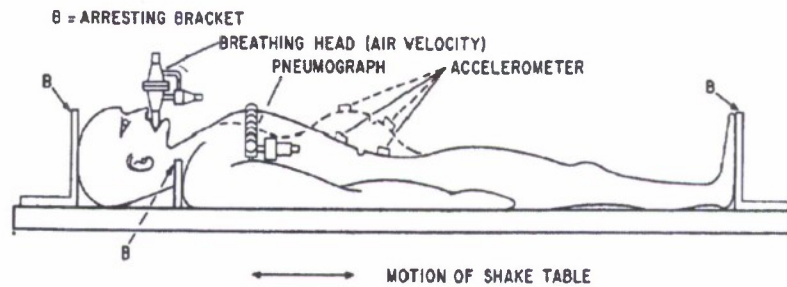


Figure 5.1: Experimental setup for Coermann et al. [3].

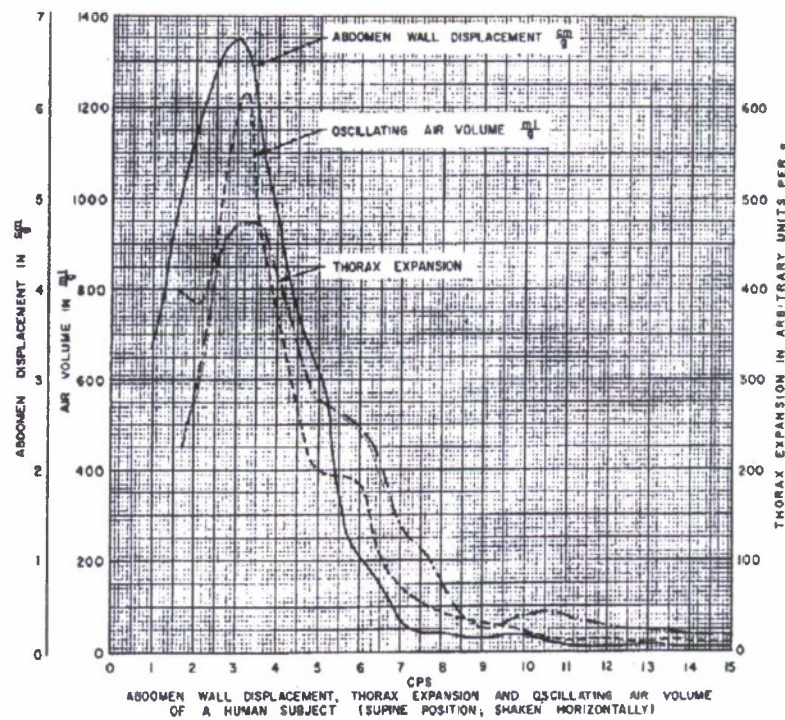


Figure 5.2: Results of experiment by Coermann et al. [3].

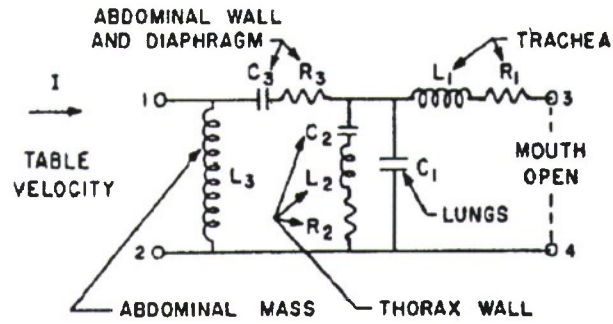


Figure 5.3: Circuit model used by Coermann et al. [3].

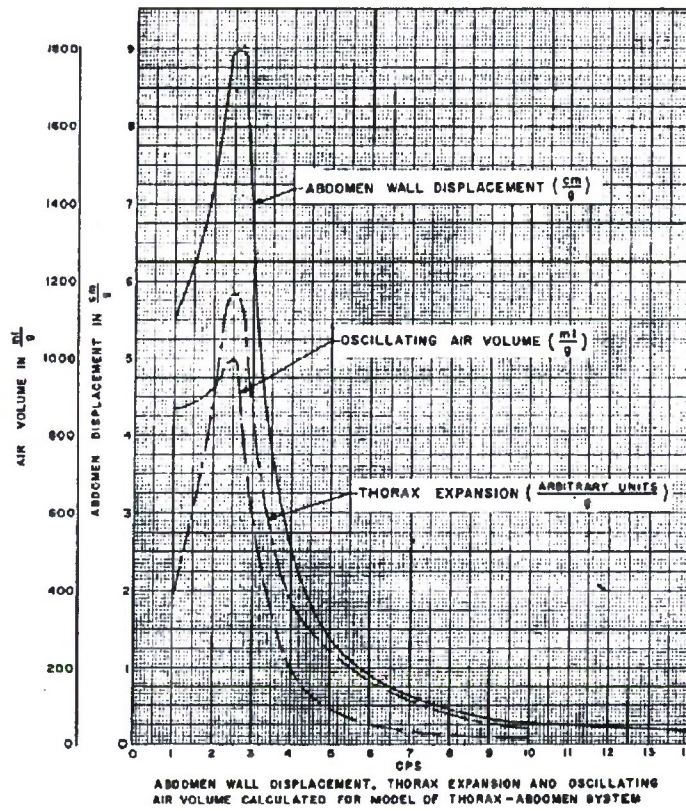


Figure 5.4: Frequency response of circuit model used by Coermann et al. [3].

It is necessary to state that the paper by Coermann et al. has insufficient information to allow replication of these results. Specifically, parameter values for the model are not included in the paper, and the method for obtaining these values is not described in any detail. The work that follows is the present author's best attempt at recreating the work done by Coermann et al., and a description of the difficulties that were encountered.

5.1 Finding the Parameter Values

According to Coermann et al. [3], the data collected did not provide enough information to assign parameter values to each element in his model, but they were able to use additional information from a paper by DuBois et al. [50] to make the complete model. DuBois et al. use the model shown in Figure 5.5 to study the airway

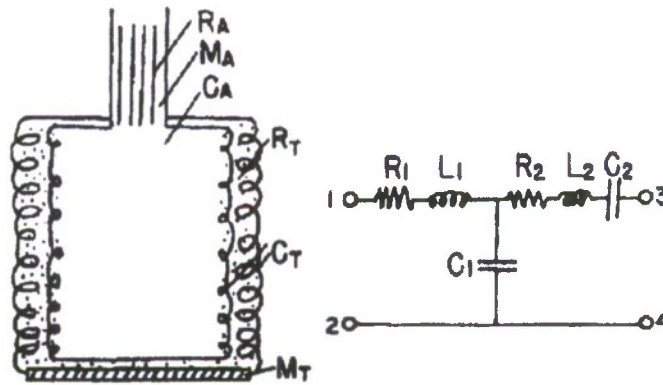


Figure 5.5: Mechano-acoustic analogue of the chest with equivalent electrical circuit. R_A , M_A and C_A are the airway resistance, inertance, and alveolar air capacitance, and R_T , M_T , and C_T are the tissue resistance, inertance, and compliance. In the electrical analogue, the airway elements correspond to elements with subscript 1, and the tissue elements correspond to elements with subscript 2. After DuBois et al. [50].

to the lungs and the lungs, including only airway properties and tissue properties. An electrical circuit analogue is also given, where the airway properties correspond to the elements with subscript 1, and the tissue properties correspond to elements with subscript 2. Although no indication of how this model corresponds to that by Coermann et al., the present author assumes that R_1 , L_1 , C_1 and R_2 , L_2 , C_2 match up with their counterparts in the circuit model by Coermann et al.. The paper by Coermann et al. states that the values for these six parameters were “chosen within the range measured” by DuBois et al..

Unfortunately for the purposes of this thesis, the paper by DuBois et al. does not clearly direct the reader to a range of values for the parameters needed. In the paper, an experiment for studying the response of the chest to sinusoidal pressure oscillations is described. During this experiment, magnitude and phase frequency responses were recorded for the impedance of the mouth-chest system. From this, an attempt was made to determine the values of the parameters in Figure 5.5. First, physiological properties from previous literature were discussed for both airway and tissue properties. From the physiological properties, DuBois et al. assigned the values (all are acoustic impedances) $R_1 = 1.5 \text{ (cm H}_2\text{O)/(l/sec)}$, $C_1 = 0.0035 \text{ l/(cm H}_2\text{O)}$, R_2 between 0.2 and 3.9 $\text{(cm H}_2\text{O)/(l/sec)}$, and C_2 between 0.07 and 0.13 $\text{l/(cm H}_2\text{O)}$. Then, calculations using the experimental data were made that show that $L_2 = 0.042 \text{ (cm H}_2\text{O)/(l/sec}^2\text{)}$ and $C_2 = 0.018 \text{ l/(cm H}_2\text{O)}$, which is contradicted by the physiological range for C_2 stated previously. DuBois et al. then concluded that this is due to the chest having a nonhomogeneous response, and uses the resonance at 5.8 Hz with $C_2 = 0.13 \text{ l/(cm H}_2\text{O)}$ to calculate another value for L_2 , $L_2 = 0.0058 \text{ (cm H}_2\text{O)/(l/sec}^2\text{)}$, which is significantly different from the other value. Then, using the values of $L_2 = 0.0058 \text{ (cm H}_2\text{O)/(l/sec}^2\text{)}$, $C_2 = 0.13 \text{ l/(cm H}_2\text{O)}$, and $C_1 = 0.0035 \text{ l/(cm H}_2\text{O)}$ and the measured amplitude ratio, a specific value for R_2 , $R_2 = 3.8 \text{ (cm H}_2\text{O)/(l/sec)}$, is given. Although this

value is within the physiological range proposed, DuBois et al. state that this value seems excessively high. No calculations are performed to determine L_1 , nor is L_1 even mentioned in the section where the other values are computed.

It is clear from the conclusions drawn by DuBois et al. that the simple system they proposed is not adequate to model the full response of the chest, and a more complicated model is needed. Also, they thought that frequency would have an effect on the parameter values. However, since Coermann et al. claimed to use the values from this paper for his model, the values of $R_1 = 1.5 \text{ (cm H}_2\text{O)/(l/sec)}$, $C_1 = 0.0035 \text{ l/(cm H}_2\text{O)}$, $R_2 = 3.8 \text{ (cm H}_2\text{O)/(l/sec)}$, $C_2 = 0.13 \text{ l/(cm H}_2\text{O)}$, and $L_2 = 0.0058 \text{ (cm H}_2\text{O)/(l/sec}^2\text{)}$ will be used in the model by Coermann et al. In MKS units, these values are (noting that $1 \text{ cm H}_2\text{O} = 98.1 \text{ N/m}^2$ and $1 \text{ m}^3 = 1000 \text{ liters}$)

$$\left. \begin{aligned} R_1 &= 147,000 \text{ N-s/m}^5 \\ C_1 &= 3.5 \times 10^{-8} \text{ N/m}^5 \\ R_2 &= 372,400 \text{ N-s/m}^5 \\ C_2 &= 1.3 \times 10^{-6} \text{ N/m}^5 \\ L_2 &= 568 \text{ kg/m}^4. \end{aligned} \right\} \quad (5.1)$$

It is important to note that the units of the parameter values indicate that the model is interpreted to be in the acoustic, or fluid, domain. However, in Figures 5.2 and 5.4, the curve labeled abdomen wall displacement has units of centimeters, which cannot be a direct response of the model; responses from a model with fluid elements are volume velocities and volumes. So in order to match the response predicted by Coermann et al., there must also be an area transformer that was incorporated into the model for at least the abdominal properties. This is an example of how Coermann et al. do not include enough detail to repeat their work, as they clearly used a model that was partially in the mechanical domain, but does not include this model or give any indication of which elements should be in the mechanical

domain. The area transformer, A , as well as values for L_1 , R_3 , C_3 , and L_3 must be extrapolated from the data collected by Coermann et al.

To do this, it can be noted in Figure 5.2 that the measured response curves have a sharp resonance around 3 Hz and a smaller resonance around 6 Hz. The resonance around 6 Hz was used by DuBois et al. to determine the value of L_2 from C_2 , so the other values must be chosen to make the resonance at 3 Hz. To aid in the process, a bond graph for the circuit model was created which is shown in Figure 5.6. In this figure, each L , R , and C element corresponds to the same element in the model in Figure 5.3. The input is a velocity (or acceleration) source, S_v , which will also be called u_{in} . From the bond graph it is possible to obtain the state equations

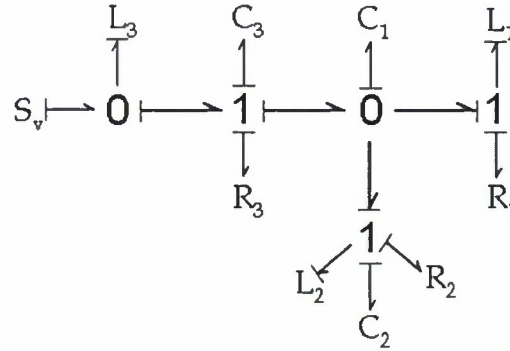


Figure 5.6: Bond graph of circuit model in Figure 5.3.

governing the system. As with von Gierke's model, the state equations are a system of first order linear ordinary differential equations that can be written in the form of Equation (4.1). In this case, the system is sixth order, and the vector \mathbf{x} is

$$\left. \begin{aligned}
x_1 &= v_{L_1}, \text{ trachea mass velocity} \\
x_2 &= x_{C_1}, \text{ lung spring displacement} \\
x_3 &= v_{L_2}, \text{ thorax wall mass velocity} \\
x_4 &= x_{C_2}, \text{ thorax wall spring displacement} \\
x_5 &= v_{L_3}, \text{ abdominal mass velocity} \\
x_6 &= x_{C_3}, \text{ abdominal wall spring displacement}
\end{aligned} \right\} \quad (5.2)$$

The 6×6 matrix is

$$\mathbf{A} = \begin{bmatrix} -R_1/L_1 & 1/C_1 & 0 & 0 & 0 & 0 \\ -1/L_1 & 0 & -1/L_2 & 0 & -1/L_3 & 0 \\ 0 & 1/C_1 & -R_2/L_2 & -1/C_2 & 0 & 0 \\ 0 & 0 & 1/L_2 & 0 & 0 & 0 \\ 0 & 1/C_1 & 0 & 0 & -R_3/L_3 & 1/C_3 \\ 0 & 0 & 0 & 0 & -1/L_3 & 0 \end{bmatrix} \quad (5.3)$$

and the input vector is

$$\mathbf{b} = \begin{bmatrix} 0 \\ u_{\text{in}} \\ 0 \\ 0 \\ R_3 u_{\text{in}} \\ u_{\text{in}} \end{bmatrix} \quad (5.4)$$

As in Chapter 4, a time harmonic solution is assumed with $\mathbf{x}(t) = \mathbf{X}(\omega)e^{j\omega t}$ and $\mathbf{b}(t) = \mathbf{B}e^{j\omega t}$, so the differential equations can be simplified to $(j\omega\mathbf{I} - \mathbf{A})\mathbf{X} = \mathbf{B}$. The frequency response from model elements can be obtained using Cramer's rule, so the responses of the abdomen displacement, the oscillating lung volume, and the thorax displacement are plotted using the parameters determined from DuBois

et al. The values for L_1 , R_3 , C_3 , and L_3 and a transformer area A are now free parameters that can be used to make the frequency response from the model look like the frequency response given by Coermann et al. in Figure 5.4. The most prominent feature of the frequency response in Figure 5.4 is the resonance around 3 Hz in each of the three responses. This resonance is determined by L_3 and C_3 , and there are an infinite number of combinations of these two values that can be used. R_3 is the parameter that determines the width of the resonance maximum value achieved at that resonance. However, using the parameters that were taken from DuBois et al., there is no value of R_3 that gives appropriate maximum value of the oscillating lung volume without making the abdominal resonance so wide that it disappears. Figure 5.7 shows a predicted response where the abdomen wall and thorax displacements have the proper shape and maximum values, but the maximum value of the oscillating lung volume response is about 3 times too high. The values used for the model are given in Table 5.1

Parameter	Value
L_1	1000 kg/m ⁴
C_1	3.5×10^{-8} N/m ⁵
R_1	147,000 N-s/m ⁵
L_2	568 kg/m ⁴
C_2	1.3×10^{-6} N/m ⁵
R_2	372,400 N-s/m ⁵
L_3	350,000 kg/m ⁴
C_3	8×10^{-9} N/m ⁵
R_3	195,000 N-s/m ⁵
A	0.5 m ²

Table 5.1: Table of parameter values used for the model by Coermann et al.

The author can only conclude that there is some misinterpretation of the model or of the method to obtain the parameter values. As stated earlier, the paper by Coermann et al. does not give sufficient information to recreate their method of obtaining parameter values.

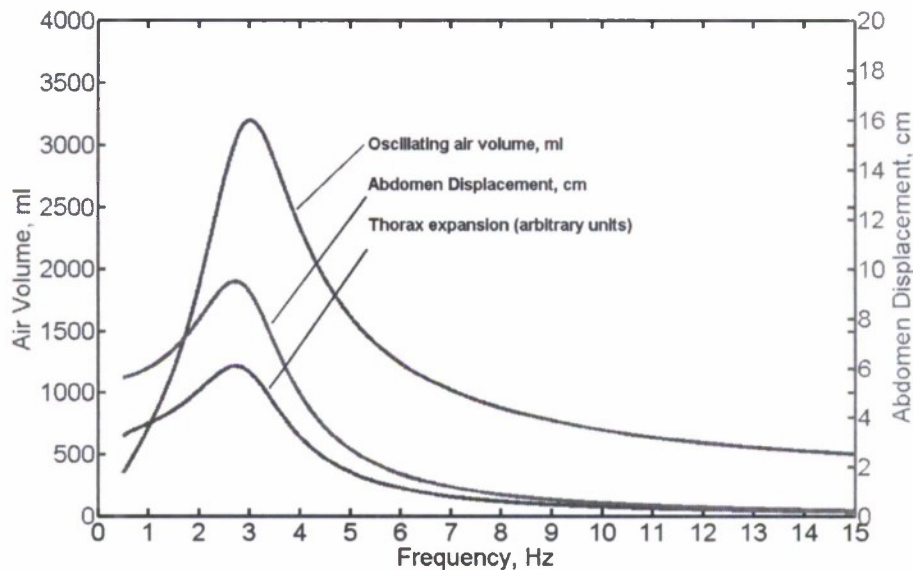


Figure 5.7: Attempt to re-create frequency response calculations [3] shown in Figure 5.4, using parameter values from DuBois et al. [50].

5.2 Physical Interpretation of the Model

In order to gain a greater understanding of the model, it is noted that when the model is represented as a circuit the connection to the anatomy of the human body is somewhat lost. There is no distinction between fluid elements and mechanical elements, so transformers must have been folded into the model. To account for this in Section 5.1, an area was added ad hoc, which is not actually an accurate fix. There is no way to know which elements Coermann et al. [3] originally interpreted to be in the mechanical domain, or what values they used for the transformers. To visualize these problems, it is helpful to see a possible mechanical analogue of the circuit model. The author's interpretation of an equivalent mechanical system for the circuit model is presented in Figure 5.8. It is stressed that this is not a unique analogue, and this particular analogue was created to resemble von Gierke's model

as closely as possible.

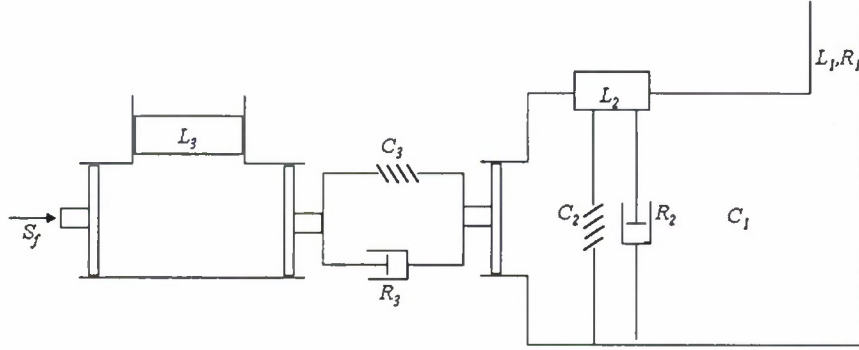


Figure 5.8: Mechanical analogue developed by the present author for the circuit model by Coermann et al. [3].

Figure 5.8 shows the input for the model as a massless piston pushing into a branching tube, where the flow is divided between L_3 , the abdominal mass, and the R_3, C_3 pair which is coupled to the lung cavity C_1 through another massless piston. L_3 and each of the massless pistons have the same contact area with fluid elements. C_1 , which is analogous to the thoracic cavity in von Gierke's model, is also coupled to the chest wall elements, L_2, R_2 , and C_2 , in the same way as they are coupled in the von Gierke model, and to a tube element with resistance and inertance L_1 and R_1 that represents the trachea. These trachea elements correspond to the respiratory mass and damper in von Gierke's model, and as von Gierke's respiratory spring constant is zero, its omission in the circuit model is not an issue.

With this mechanical analogue, it is necessary that L_2, C_2, R_2, L_3, C_3 , and R_3 all have transformers to be in the mechanical domain. For example, the chest wall area, A_w specified by von Gierke and given in Table 4.1 can be used along with the value of L_2 , which is labeled as the thorax wall, to find a value for the mass of the thorax wall; $L_2 \cdot A_w^2 = 568 \text{ kg/m}^4 \cdot (0.02 \text{ m}^2)^2 = 0.23 \text{ kg}$, which is about one order of magnitude smaller than von Gierke's chest wall mass. As these area transformers

are not even alluded to by Coermann et al., there is no way to come close to guessing what values were used, so the mechanical analogue cannot be taken further. It is not possible to separate out specific physical elements of the body without these transformers, as was possible for von Gierke's model in Chapter 4.

To summarize this chapter, it must again be stressed that Coermann et al. did not give enough information to reproduce their results or to correctly interpret the model anatomically. The parameter values in Table 5.1 have little meaning without areas to translate into the mechanical domain, so there is no way to know whether they are reasonable values. When dealing with these problems, several courses of action were taken, including using von Gierke's parameters in the mechanical analogue presented in Figure 5.8. The responses, however, could not be reconciled with the responses provided by Coermann et al. or with the responses obtained in Chapter 4. Although these difficulties have prevented a thorough use of the circuit model used by Coermann et al. in this thesis, the work done by the author and the mechanical analogue are presented as a possible starting point for future work. The topology of the model is very valid, and it seems to be very well suited to this problem, so the present author believes that the model warrants additional work if different methods of determining the parameter values are available.

Chapter 6

Other Models

The two models discussed in detail in Chapters 4 and 5 are clearly the most representative of the lung and internal organs, which are the focus of this project. However, there is still value in obtaining frequency responses from other models catalogued in Chapter 3, which can contribute to a greater understanding of the effects of the whole-body vibration due to the sound field. The models in the present chapter do not have any lung elements, and often do not have specific body parts labeled, so the adjustments that were made earlier for the body being underwater can no longer be made. Thus, it is response to vibration alone that the results will represent.

6.1 Plan of Action

Although there are no changes to make to account for the body being underwater, source placement is still an issue for these models. For most of the models, the input is either on the buttocks, or a seat if the model is of a seated subject, or the feet if the model is of a standing subject. When obtaining the response of the models in the context of this thesis, any seats and other external elements will be ignored. Body parts not attached directly to the main body, such as legs on a seat,

are ignored as well. The acceleration source is then applied to the largest mass in the model, which is often a mass labeled ‘torso’ or ‘spine’. If there are two masses that are comparable in size and clearly dominate the rest of the model elements, the source is applied to both masses.

Another thing that varies from model to model is the mass element for which it is most interesting to obtain the response. Since it is the response of the inner organs that is most relevant to this project, the masses of interest will be labeled with names that imply internal organs, such as ‘viscera’, ‘abdomen’, or ‘thorax’. In general, these masses are smaller and tend to be located towards the center of an anatomically-based model. Responses of seven relevant models from Chapter 3 are given in the next section, following these guidelines.

Once the source placement is determined, the bond graph can be made and state equations derived, as with the models in Chapters 4 and 5. From the state equations, the frequency responses of the masses of interest can be found, again using Cramer’s rule. As with the previous models, the velocity responses of the mass elements in the models can be found, and then the acceleration and displacement can be found by multiplying and dividing, respectively, by the angular frequency. The acceleration, velocity, and displacement responses of the mass(es) of interest for each model are plotted for 190 dB and 230 dB in the following section. Each of these models had parameter values given by the creator of the model so responses could easily be obtained.

6.2 Results

6.2.1 Wan and Schimmels [38]

This model, shown in Figure 3.2(g), was found to best simulate the compilation of experimental results put together by Liang and Chiang [34]. It includes a seat,

which will be ignored, and the acceleration source when obtaining the responses for this thesis will be applied to the largest mass, which is the lower torso. The response

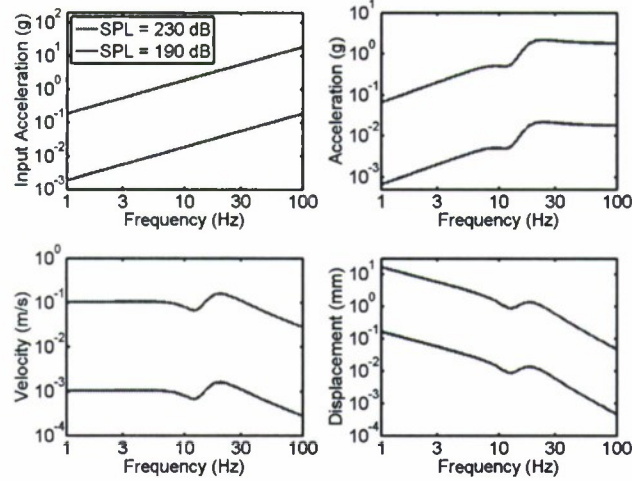
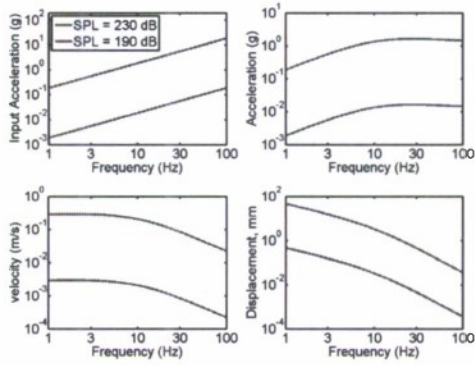


Figure 6.1: Response of the ‘viscera’ from Wan and Schimmels [38]. Parameter values used are [34]: $m_1 = 36$ kg, $m_2 = 5.5$ kg, $m_3 = 15$ kg, $m_4 = 4.17$ kg, $c_1 = 2,475$ N-s/m, $c_2 = 330$ N-s/m, $c_3 = 200$ N-s/m, $c_{31} = 909.1$ N-s/m, $c_4 = 250$ N-s/m, $k_1 = 49,340$ N/m, $k_2 = 20,000$ N/m, $k_3 = 10,000$ N/m, $k_{31} = 192,000$ N/m, $k_4 = 134,400$ N/m.

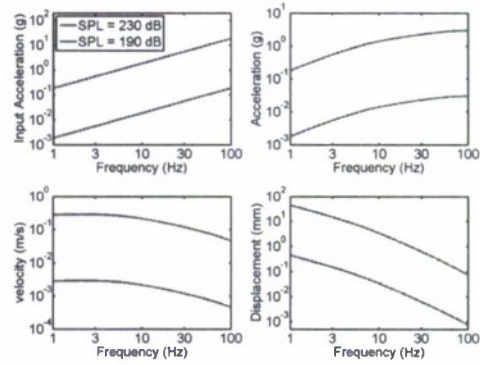
of interest is that of the viscera, shown in Figure 6.1, which has a resonance at 21 Hz.

6.2.2 Muksian and Nash [40] and Quassem et al. [41]

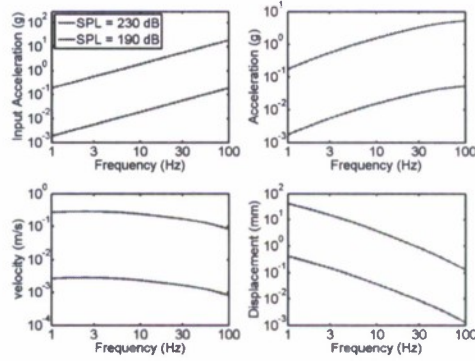
The two models in this section are from the same collection as the model in Section 6.2.1, and were also selected by Liang and Chiang [34] as models that correspond well with experimental data. The models are shown in Figure 3.2(h) and (i), where it can be seen that the model by Quassem et al. [41] is an expansion of the model by Muksian and Nash [40], with extra spine elements and added arm elements. For both models, the largest masses are the pelvis and torso, and the masses of interest are the abdomen, diaphragm, and thorax.



(a) Response of the abdomen.



(b) Response of the diaphragm.



(c) Response of the thorax.

Figure 6.2: Responses from Muksian and Nash's model [40]. Parameter values used are [34]: $m_1 = 27.23$ kg, $m_2 = 5.921$ kg, $m_3 = 0.455$ kg, $m_4 = 1.362$ kg, $m_5 = 32.762$ kg, $m_6 = 6.82$ kg, $m_7 = 5.45$ kg, $c_2 = c_3 = c_4 = c_5 = 292$ N-s/m, $c_{56} = c_6 = c_7 = 3,580$ N-s/m, $k_2 = k_3 = k_4 = k_5 = 877$ N/m, $k_{56} = k_6 = k_7 = 52,600$ N/m.

Closer inspection reveals that with respect to the interactions between these five masses, the two models are the same, as the expansions and additions included in the model by Quassem et al. do not affect those masses. Therefore, the responses of interest will be identical for these two models. The frequency responses for the abdomen, diaphragm, and thorax are given in Figure 6.2. These responses do not have a resonance in the frequency range that was looked at, and in most cases responses are monotonically increasing or decreasing.

6.2.3 Smith [43]

The seated subject model created by Smith [43] can be seen in Figure 3.4. When obtaining the frequency responses for this section, the leg section consisting of M_4 and M_5 is ignored and the input is applied to M_1 , the pelvis. The response of interest, shown in Figure 6.3, is that of the torso/chest, or M_3 . There are two

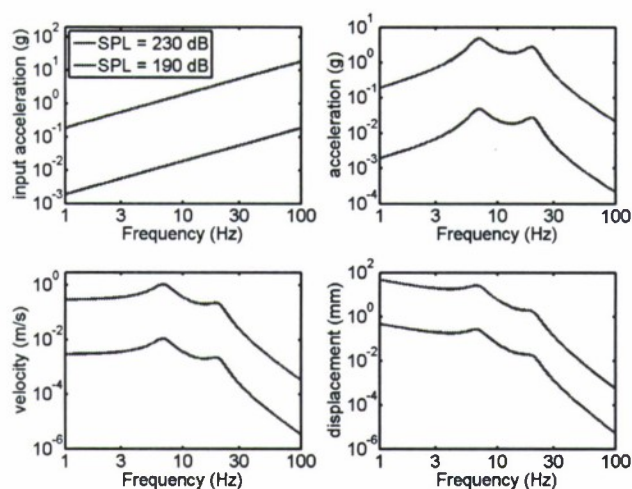


Figure 6.3: Response of the torso/chest mass in Smith's model. Parameter values are [43]: $M_1 = 28.1$ kg, $M_2 = 11.8$ kg, $K_2 = 162,671$ N/m, $C_2 = 17.5$ N-s/m, $M_3 = 17.2$ kg, $K_3 = 37,230$ N/m, $C_3 = 332$ N-s/m.

resonances for this response, at 7 Hz and at 20 Hz.

6.2.4 Mertens [42]

As with the last model, this model created by Mertens [42] has a leg component that will be ignored for the purposes this thesis. Seen in Figure 3.3, the model also does not have any main 'outer' masses, so the acceleration source will be applied to the massless connections between the C_3 - K_3 pair and the C_5 - K_5 pair, and between the C_5 - K_5 pair and the C_7 - K_7 pair. The responses of M_4 , described as the abdomen, and M_6 , the chest, are plotted in Figure 6.4. M_4 , the abdominal mass, has a resonance

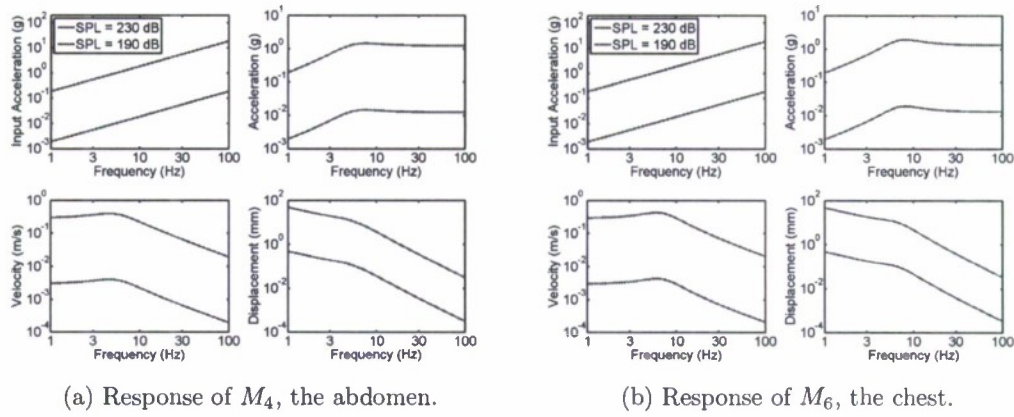


Figure 6.4: Responses from Mertens's model. Parameter values are [42]: $M_1 = 15$ kg, $K_1 = 47,966$ N/m, $C_1 = 678$ N-s/m, $M_2 = 10$ kg, $K_2 = 250,000$ N/m, $C_2 = 4,000$ N-s/m, $K_3 = 200,000$ N/m, $C_3 = 1,000$ N-s/m, $M_4 = 15$ kg, $K_4 = 17,913$ N/m, $C_4 = 622$ N-s/m, $K_5 = 160,000$ N/m, $C_5 = 2,000$ N-s/m, $M_6 = 22$ kg, $K_6 = 42,558$ N/m, $C_6 = 968$ N-s/m, $M_7 = 7$ kg, $K_7 = 89,537$ N/m, $C_7 = 633$ N-s/m.

at about 7.5 Hz, and M_6 , the chest, has a resonance around 9 Hz.

6.2.5 Yue and Mester [46]

The model by Yue and Mester [46] is for a standing subject, and can be seen in Figure 3.7. For this model, the input will be on the outer mass, M_3 , and the interest is in the frequency response of M_4 , the internal 'wobbling' mass. Thus, it is the response of the inner mass to an outer shell that is shown in Figure 6.5, and M_1 and M_2 in the model are effectively ignored. There is not a clear resonance in the response so most of the responses are monotone increasing or decreasing, thus the maximum accelerations are only over the frequency range included in the plot. These maximum accelerations occur at 100 Hz, and are 0.56 g for the input of 190 dB and 56.3 g for the input of 230 dB. These accelerations are much higher than other responses seen in this section, which follows from the fact that the spring and damping constants

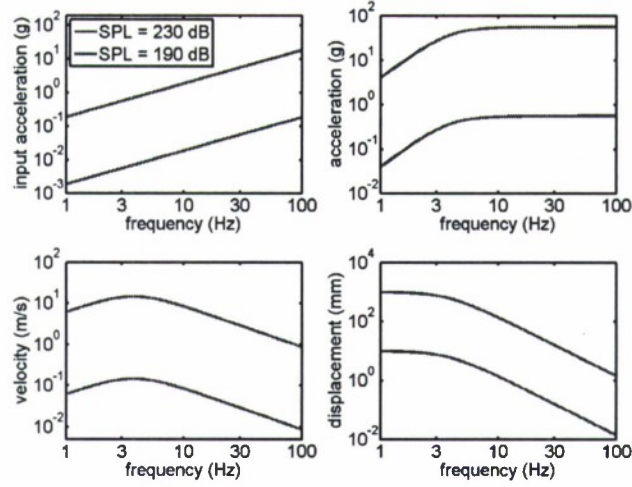


Figure 6.5: Response of the wobbling mass in the model by Yue and Mester [46]. Parameter values are: $M_1 = 6.15$ kg, $M_2 = 6$ kg, $M_3 = 12.58$ kg, $M_4 = 50.34$ kg, $k_1 = 6$ kN/m, $k_2 = 6$ kN/m, $k_3 = 10$ kN/m, $k_4 = 10$ kN/m, $k_5 = 18$ kN/m, $c_1 = 300$ N-s/m, $c_2 = 650$ N-s/m, $c_4 = 1900$ N-s/m.

are generally much lower in this model. In addition, the purpose of the model was to study the impact on the inner organs when the foot hits the ground, not vertical vibration like the rest of the models. Thus, the model parameters seem to have been chosen with a different motivation that makes it less applicable to this situation, so the responses will not be considered when drawing conclusions for this thesis.

6.2.6 Garg and Ross [44]

The final model is the standing model by Garg and Ross [44] which is shown in Figure 3.5. For this model, the internal organs are lumped together into one mass, which is the most meaningful mass for the purposes of this thesis. The input is applied to both the upper torso and the lower trunk, so it is similar to the model in Section 6.2.5, where the mass of interest receives the input from two sides, and a set of springs and dampers in between each input. The frequency response, shown

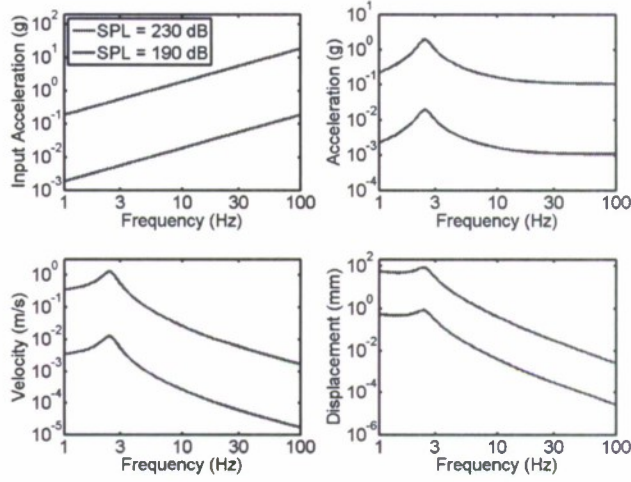


Figure 6.6: Response of the inner organs in Garg and Ross's model. Parameter values are [44]: Masses (kg): $M_1 = 4.76544$, $M_2 = 0.0544872$, $M_3 = 0.05450472$, $M_4 = 23.1264$, $M_5 = 7.48104$, $M_6 = 7.48104$, $M_7 = 3.04848$, $M_8 = 3.04848$, $M_9 = 2.4528$, $M_{10} = 2.04984$, $M_{11} = 2.04984$, $M_{12} = 1.161576$, $M_{13} = 1.161576$, $M_{14} = 4.09968$, $M_{15} = 4.09968$, $M_{16} = 0.001752$. Springs (N/m): $k_{115} = 175200$, $k_{1415} = 35040$, $k_{415} = 3153.6$, $k_{414} = 2277.6$, $k_{514} = 359160$, $k_{614} = 359160$, $k_{57} = 359160$, $k_{68} = 359160$, $k_{79} = 359160$, $k_{89} = 359160$, $k_{1015} = 26280$, $k_{1115} = 26280$, $k_{1012} = 26280$, $k_{1113} = 26280$, $k_{212} = 26280$, $k_{313} = 26280$, $k_{116} = 129.648$. Dampers (N-s/m): $c_{115} = 17.52$, $c_{1415} = 350.4$, $c_{415} = 52.56$, $c_{414} = 31.536$, $c_{514} = 963.6$, $c_{614} = 963.6$, $c_{57} = 963.6$, $c_{68} = 963.6$, $c_{79} = 963.6$, $c_{89} = 963.6$, $c_{1015} = 175.2$, $c_{1115} = 175.2$, $c_{1012} = 175.2$, $c_{1113} = 175.2$, $c_{212} = 175.2$, $c_{313} = 175.2$, $c_{116} = 0.00876$.

in Figure 6.6, has a resonance at 2.5 Hz.

6.3 Generalizations

For the purposes of this thesis, none of the models in this chapter are ideal representations of the human body, especially when considering the lungs and internal organs. However, to maintain the greatest possible understanding of whole-body vibration, the responses of the models are obtained. To generalize the responses found in this chapter, the shapes and the maximum values of the responses are interesting

characteristics. It is important to note that the responses plotted in this chapter are from different elements of the body, often nondescriptive or lumping many body parts together. Just as with von Gierke's model, no data have been found on the motion of internal organs, so there is very little that can be said to interpret these results.

Looking at the shapes of the plots, there are several responses without a resonance, and some with one or two very sharp resonances. There can be no generalization because the responses are so different. In several responses, there is no prevalent resonance, and maximum values are found at the edges of the frequency range—at 1 or 100 Hz. In most cases, if there is a resonance it is below 10 Hz, which is common for the resonance of internal organs found in vibration experiments in air. The one exception to this is the model by Wan and Schimmels [38], which has a visceral response resonance closer to 20 Hz. One generalization that can be drawn about the response shape is that the displacement response is almost always monotonically decreasing, with its maximum value at 1 Hz, even if there is a resonance.

The maximum acceleration response values, excluding the one outlier for the model of Yue and Mester [46], fall under $0.1g$ for the input at 190 dB and under $10g$ for the input at 230 dB. These values are lower than those for von Gierke's model, which were $33g$ for the abdomen and $11g$ for the chest wall at 230 dB. With smaller responses than that of von Gierke's model, it is even more likely that these models will not show responses that would generate any discomfort or injury to the diver. The maximum velocity responses from the models are mostly on the order of 0.001 m/s and 0.1 m/s for the inputs at 190 dB and 230 dB, respectively. These values are very close to the values obtained with von Gierke's model. The maximum displacement responses are consistently between 0.45 and 0.5 mm for the input at 190 dB and 45 and 50 mm for the input at 230 dB. These values are actually much

higher than the displacements of the organs in von Gierke's model. However, as discussed in Section 4.5, it is unlikely that discomfort or injury in this circumstance will be caused by strain, so higher displacements probably do not signify more probability for injury. It follows that the responses from von Gierke's model, from which it was concluded in Chapter 4 that the responses were not going to cause significant effects, are worst case scenarios to the responses from these models. Thus, this chapter supports previous conclusions that the whole-body vibration response would be too small to have a major effect on a diver.

Chapter 7

Conclusion

In this thesis, the human bioresponse to whole-body vibration was studied in the context of an underwater acoustic wave excitation. For the low frequencies in this work (40–80 Hz), a person is small compared to a wavelength and can be considered an entrained particle. Under these circumstances, a diver assumed to be neutrally buoyant will experience the particle velocity and acceleration of the incident wave as a translational vibration known as whole-body vibration. A review of previous work on the subject of whole-body vibration was conducted, and steps were taken to draw conclusions about the effects of whole-body vibration experienced as a result of the underwater sound wave excitation. Throughout the thesis, the excitation is assumed to be a time-harmonic progressive plane wave, and sound pressure levels used for the source are 190 dB, an expected level for underwater sonar devices, and 230 dB, a maximum level before cavitation occurs in water.

In Chapter 2, experimental results were presented along with two standards that propose whole-body vibration exposure limits for workplace environments. Conclusions were drawn by comparing the underwater vibration source to the vibration sources in the experiments and standards. Unfortunately, most of the experiments were conducted in frequencies under 20 Hz, which is optimal for vehicle

vibration, and cannot be applied to this thesis. When comparing to the standards, it was found that the input level of 190 dB is well below the discomfort limit, while the input level of 230 dB exceeds the exposure limits. Although the standards seem to show conclusive results, it is important to note that the standards were made to set limits for long-term vibration exposure in the workplace, so applying them to the situation assumed in this thesis took them out of context. In addition, it was difficult to draw conclusions from the standards because of the ambiguity and inconclusiveness of the standards themselves. The standards and experiments both made it clear that different people are affected differently by vibration, and it is virtually impossible to set a specific point where the effects of vibration will have a specific effect on every person in every situation.

Another method used to study whole-body vibration involves lumped-parameter models of the human body that were created to generate responses similar to data measured in whole-body vibration experiments. A compilation of several such models is included in Chapter 3, where the background and context of each model is discussed. It was concluded that the best models were those that include lung properties as fluid elements, and that focus more on inner organs than limbs. Using these criteria, the best two models found by the author are a five-degree-of-freedom model created by Henning von Gierke [14], and a circuit model created by Ralph Coermann et al. [3].

Chapter 4 goes into detail about the use of von Gierke's model in the context of this thesis. Because the diver is underwater, some adjustments were made to account for features of the different environment. Results from von Gierke's model showed that the 190 dB input generates responses that are close to exposure limits, and could possibly have an effect in the higher frequencies between 40 and 80 Hz, while the 230 dB input gives high responses, that show the possibility of injury. Results also showed that when the acoustic pressure is included as a source, the

responses are completely dominated by this input, from which it can be concluded that the effects of the acoustic pressure are much greater than that of the particle acceleration, so the effects of the particle velocity will most likely be unimportant.

The circuit model by Coermann et al. is studied in detail in Chapter 5, although the model is much more difficult to interpret than von Gierke's model, as Coermann et al. did not provide sufficient documentation in the original work to apply it to this work. Finding parameter values for the model proved to be difficult, and did not yield corroboration with results from Coermann et al. A possible mechanical analogue of the model is proposed that is very similar to von Gierke's model, and it is seen that area transformers are necessary for the mechanical analogue to have meaning. With insufficient information, it was impossible to obtain response plots for the model, but further work in understanding the model and obtaining correct parameter values is encouraged, as the topology of the model seems to be good. In Chapter 6, responses from several of the other models presented in Chapter 3 are obtained without making changes to the models for the underwater environment. The responses from the models were varied and difficult to interpret in any detail, but the responses seemed low enough, especially for the 190 dB input, to conclude that the effects would not be significant.

In general, from looking at many models and experiments, it seems reasonable to conclude that the whole-body vibration effects of the particle velocity of the excitation wave will not be significant, and will clearly be dominated by the effects of the acoustic pressure on the lungs. However, since most of the work in whole-body vibrations is done under 20 Hz, the accuracy of the extrapolations and applicability of the results is unclear. Further experimentation and data for whole-body vibration over 20 Hz as well as additional information on individual organ motion would be required to make a more certain conclusion.

Appendix A

Derivation of Added Mass

The added mass due to the inertial load of the water on the chest wall is derived by approximating the motion of the chest wall as a vibrating cap on a sphere. Justification of this simple model is the very low frequencies, with wavelengths very long in comparison with the human body. Under these circumstances, the specific geometries of the radiating surface and of the body on which it is mounted are unimportant. Instead, it is found that relative size matters most. The reactance of the desired mechanical impedance is $j\omega M$, where M is the added mass sought. First, the radiation from a general axisymmetrical spherical source is considered, assuming the geometry shown in Figure A.1. Next, the general solution is applied to the vibrating cap, following the treatment by Morse and Ingard [51] but with more convenient notation.

The wave radiates into a medium with density ρ_0 and sound speed c_0 . It is assumed that the excitation is time harmonic and that the radiated field is axisymmetric, so a boundary condition for $u_r(a, \theta)$, the radial velocity on the surface of the sphere, is given in by

$$u_r(a, \theta) = u_0 f(\theta) e^{j\omega t}, \quad (\text{A.1})$$

where r and θ are the spherical coordinates shown in Figure A.1, and $f(\theta)$ is an

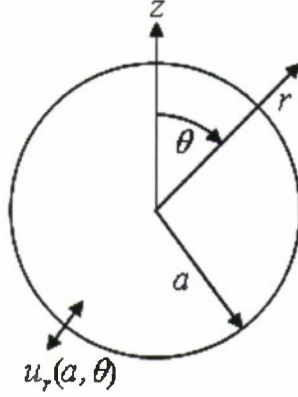


Figure A.1: Geometry for a general axisymmetric spherical source.

arbitrary function that will be used to make the solution specific to the vibrating cap problem. The general solution for the acoustic pressure of an outgoing, time-harmonic spherical wave for the axisymmetric geometry shown in Figure A.1 is

$$p = \sum_{n=0}^{\infty} A_n P_n(\cos \theta) h_n(kr) e^{j\omega t}, \quad (\text{A.2})$$

where P_n is the n^{th} order Legendre polynomial, h_n is the n^{th} order spherical Hankel function of the second kind, A_n is a coefficient to be determined by the boundary condition, and $k = \omega/c_0$. Hankel functions of the second kind are used for outward-radiating waves when the time dependence is $e^{j\omega t}$, and they are usually denoted $h_n^{(2)}$. However, the superscript is cumbersome and will be suppressed in the following, as only Hankel functions of the second kind are used.

To satisfy the boundary condition, the pressure must be converted to particle velocity, which is accomplished with the momentum equation:

$$u_r(r, \theta) = -\frac{1}{j\omega\rho_0} \frac{\partial p}{\partial r}, \quad (\text{A.3})$$

or

$$u_r(r, \theta) = -\frac{1}{j\rho_0 c_0} \sum_{n=0}^{\infty} A_n P_n(\cos \theta) h'_n(kr) e^{j\omega t}, \quad (\text{A.4})$$

where the prime on $h'_n(kr)$ denotes the derivative of the Hankel function with respect to its argument. The boundary condition in Equation (A.1) can then be expanded, using the orthogonality of the Legendre polynomials, as

$$u_r(a, \theta) = u_0 e^{j\omega t} \sum_{n=0}^{\infty} U_n P_n(\cos \theta), \quad (\text{A.5})$$

where

$$U_n = \left(n + \frac{1}{2}\right) \int_0^\pi f(\theta) P_n(\cos \theta) \sin \theta \, d\theta. \quad (\text{A.6})$$

Setting Equation (A.5) equal to Equation (A.4) at $r = a$ gives

$$A_n = -j\rho_0 c_0 u_0 \frac{U_n}{h'_n(ka)}. \quad (\text{A.7})$$

The general solution with the boundary condition from Equation (A.1) is thus

$$p = -j\rho_0 c_0 u_0 e^{j\omega t} \sum_{n=0}^{\infty} \frac{h_n(kr)}{h'_n(ka)} U_n P_n(\cos \theta), \quad (\text{A.8})$$

with U_n as defined in Equation (A.6).

Now, consider a radially vibrating piston in the form of a cap on a sphere, as shown in Figure A.2. The angle θ_0 defines the edge of the piston, which has radial velocity $u_r(a, \theta) = u_0 e^{j\omega t}$. For this geometry, $f(\theta)$ from Equation (A.1) is

$$f(\theta) = \begin{cases} 1 & \text{if } 0 \leq \theta \leq \theta_0 \\ 0 & \text{if } \theta_0 \leq \theta \leq \pi \end{cases}. \quad (\text{A.9})$$

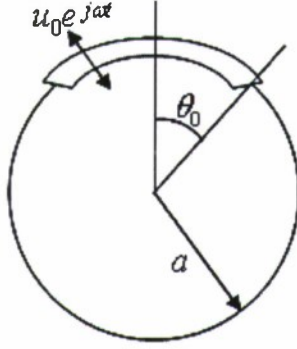


Figure A.2: Geometry for the vibrating cap.

Then, U_n , from Equation (A.6), is

$$U_n = \left(n + \frac{1}{2}\right) \int_0^{\theta_0} P_n(\cos \theta) \sin \theta d\theta = \frac{1}{2} [P_{n-1}(\cos \theta_0) - P_{n+1}(\cos \theta_0)], \quad (\text{A.10})$$

where $P_{-1} \equiv 1$. In order to find the mechanical impedance, $Z_{\text{mech}} = F/u_r$, it is necessary to find F , the force exerted by the piston, and u_r , the radial velocity of the piston, which is prescribed by the boundary condition. The force exerted by the piston can be written $F = \int p dS$ at $r = a$. For the piston, $dS = 2\pi a^2 \sin \theta d\theta$, so the force can be calculated as follows:

$$F = \int_0^{\theta_0} \left[-j\rho_0 c_0 u_0 e^{j\omega t} \sum_{n=0}^{\infty} \frac{h_n(ka)}{h'_n(ka)} U_n P_n(\cos \theta) \right] 2\pi a^2 \sin \theta d\theta \quad (\text{A.11})$$

$$= -j2\pi a^2 \rho_0 c_0 u_0 e^{j\omega t} \sum_{n=0}^{\infty} \frac{h_n(ka)}{h'_n(ka)} U_n \int_0^{\theta_0} P_n(\cos \theta) \sin \theta d\theta. \quad (\text{A.12})$$

It is noted from Equation (A.10) that the integral is equal to $2U_n/(2n+1)$. F can then be written

$$F = -j4\pi a^2 \rho_0 c_0 u_0 e^{j\omega t} \sum_{n=0}^{\infty} \frac{h_n(ka)}{h'_n(ka)} \frac{U_n^2}{2n+1}, \quad (\text{A.13})$$

and

$$Z_{\text{mech}} = \frac{F}{u_0 e^{j\omega t}} = -j4\pi a^2 \rho_0 c_0 \sum_{n=0}^{\infty} \frac{h_n(ka)}{h'_n(ka)} \frac{U_n^2}{2n+1}. \quad (\text{A.14})$$

Now, in the long wavelength limit it is assumed that $ka \ll 1$. Under this assumption, the $n = 0$ term dominates, and in the small ka limit

$$\frac{h_n(ka)}{h'_n(ka)} \approx -ka. \quad (\text{A.15})$$

So, with $ka \ll 1$,

$$Z_{\text{mech}} \approx jka\rho_0 c_0 4\pi a^2 U_0^2. \quad (\text{A.16})$$

From Equation (A.10),

$$U_0 = \frac{1}{2}[P_{-1}(\cos \theta_0) - P_1(\cos \theta_0)] = \frac{1 - \cos \theta_0}{2}. \quad (\text{A.17})$$

Now, consider the surface area of the cap, which is found as

$$S_{\text{cap}} = \int_0^{\theta_0} 2\pi a^2 \sin \theta \, d\theta = 2\pi a^2 (1 - \cos \theta_0) = 4\pi a^2 U_0. \quad (\text{A.18})$$

Then, with $U_0 = S_{\text{cap}}/4\pi a^2$, it follows that

$$Z_{\text{mech}} = j\omega\rho_0 a (4\pi a^2) \left(\frac{S_{\text{cap}}}{4\pi a^2} \right)^2 = j\omega\rho_0 \frac{S_{\text{cap}}^2}{4\pi a}, \quad (\text{A.19})$$

and the added mass is

$$M = \rho_0 \frac{S_{\text{cap}}^2}{4\pi a}. \quad (\text{A.20})$$

Bibliography

- [1] J. S. Martin, P. H. Rogers, and E. A. Cudahy. Measurement of the depth-dependant resonance of water-loaded human lungs. *Journal of the Acoustical Society of America*, 117(4):2291–2300, 2005.
- [2] E. B. Magid, R. R. Coermann, and G. H. Ziegenruecker. Human tolerance to whole body sinusoidal vibration; short-time, one-minute and three-minute studies. *Aerospace Medicine*, 31(11):915–924, 1960.
- [3] R. R. Coermann, G. H. Ziegenruecker, A. L. Wittwer, and H. E. von Gierke. The passive dynamic mechanical properties of the human thorax-abdomen system and the whole body system. *Aerospace Medicine*, 31(6):443–455, 1960.
- [4] H. E. von Gierke and A. J. Brammer. Effects of shock and vibrations on humans. In Cyril M. Harris, editor, *Shock and Vibration Handbook*, chapter 44. McGraw-Hill, 1961.
- [5] Jr. G. H. White, K. O. Lange, and R. R. Coermann. The effects of simulated buffeting on the internal pressure of man. *Human Factors*, 4(5):275–290, 1962.
- [6] R. R. Coermann, E. B. Magid, and K. O. Lange. Human performance under vibrational stress. *Human Factors*, 4(5):315–324, 1962.
- [7] K. O. Lange and R. R. Coerman. Visual acuity under vibration. *Human Factors*, 4(5):291–300, 1962.

- [8] W. S. Clark, K. O. Lange, and R. R. Coerman. Deformation of the human body due to uni-directional forced sinusoidal vibration. *Human Factors*, 4(5):255–273, 1962.
- [9] R. R. Coermann. The mechanical impedance of the human body in sitting and standing position at low frequencies. *Human Factors*, 4(5):227–254, 1962.
- [10] H. E. von Gierke. Biodynamic response of the human body. *Applied Mechanics Reviews*, 17(12):951–958, 1964.
- [11] G. C. Mohr, J. N. Cole, E. Guild, and H. E. von Gierke. Effects of low frequency and infrasonic noise on man. *Aerospace Medicine*, 36(9):817–824, 1965.
- [12] H. L. Vogt, R. R. Coermann, and H. D. Fust. Mechanical impedance of the sitting human under sustained acceleration. *Aerospace Medicine*, 39(7):675–679, 1968.
- [13] H. E. von Gierke. Response of the body to mechanical forces- an overview. *Annals of the New York Academy of Sciences*, 152:172–186, 1968.
- [14] I. Kaleps and H. E. von Gierke. A five-degree-of-freedom mathematical model of the body. In *Symposium on Biodynamic Models and Their Applications*, pages 211–231, Oct 1970.
- [15] H. E. von Gierke. Biodynamic models and their applications. *Journal of the Acoustical Society of America*, 50(6):1397–1413, 1971.
- [16] H. E. von Gierke and C. W. Nixon. Effects of intense infrasound on man. In W. Tempest, editor, *Infrasound and Low Frequency Vibration*, chapter 6, pages 115–150. Academic Press, 1976.
- [17] H. E. von Gierke. To predict the body's strength. *Aviation, Space, and Environmental Medicine*, 59(11):A107–115, 1988.

- [18] H. E. von Gierke. Effects of vibration and shock on people. In Malcolm J. Crocker, editor, *Encyclopedia of Acoustics*, chapter 145, pages 1761–1779. John Wiley and Sons, Inc., 1997.
- [19] M. J. Griffin. Vibration and visual acuity. In W. Tempest, editor, *Infrasound and Low Frequency Vibration*, pages 263–298. Academic Press, 1976.
- [20] M. J. Griffin. *Handbook of Human Vibration*. Academic Press, 1990.
- [21] S. Kitazaki and M. J. Griffin. A modal analysis of whole-body vertical vibration, using a finite element model of the human body. *Journal of Sound and Vibration*, 200(1):83, 1997.
- [22] M. J. Griffin. A comparison of standardized methods for predicting the hazards of whole-body vibration and repeated shocks. *Journal of Sound and Vibration*, 215(4):883–914, 1998.
- [23] L. Wei and M. Griffin. The prediction of seat transmissibility from measures of seat impedance. *Journal of Sound and Vibration*, 214(1):121–137, 1998.
- [24] H. K. Jang and M. J. Griffin. Effect of phase, frequency, magnitude and posture on discomfort associated with differential vertical vibration at the seat and feet. *Journal of Sound and Vibration*, 229(2):273–286, 2000.
- [25] Y. Matsumoto and M. J. Griffin. Comparison of biodynamic responses in standing and seated human bodies. *Journal of Sound and Vibration*, 238(4):691–704, 2000.
- [26] Y. Matsumoto and M. J. Griffin. Mathematical models for the apparent masses of standing subjects exposed to vertical whole-body vibration. *Journal of Sound and Vibration*, 260:431–451, 2003.

- [27] M. Morioka and M. J. Griffin. Magnitude-dependence of equivalent comfort contours for fore-and-aft, lateral, and vertical whole-body vibration. *Journal of Sound and Vibration*, 298:755–772, 2006.
- [28] D. Dieckmann. A study of the influence on vibration on man. *Ergonomics*, 1(4):437–355, 1958.
- [29] D. M. Cowley. Appendix: International standards in the vibration field. In W. Tempest, editor, *Infrasound and Low Frequency Vibration*, pages 349–357. Academic Press, 1976.
- [30] D. J. Sass. Mechanisms of injury due to intense gz vibration in water-immersed cats. *Journal of Applied Physiology*, 26(6):819–826, 1969.
- [31] J. T. Reason. Motion sickness and associated phenomena. In W. Tempest, editor, *Infrasound and Low Frequency Vibration*, pages 299–348. Academic Press, 1976.
- [32] E. J. Lovesey. The occurrence and effects upon performance of low frequency vibration. In W. Tempest, editor, *Infrasound and Low Frequency Vibration*, pages 235–262. Academic Press, 1976.
- [33] S. J. Parvin and J. R. Nedwell. The effects of low frequency sonar transmissions on divers and ichthyofauna: literature survey and initial experimental results. Technical Report DRA(AWL)TM93721, Defense Research Agency, 1993.
- [34] C.-C. Liang and C.-F. Chiang. A study on biodynamic models of seated human subjects exposed to vertical vibration. *International Journal of Industrial Ergonomics*, 36:869–890, 2006.
- [35] R. Muksian and C. D. Nash. On frequency-dependant damping coefficients in

- lumped parameter models of human beings. *Journal of Biomechanics*, 9:339–342, 1976.
- [36] G. Allen. A critical look at biomechanical modeling in relation to specifications for human tolerance of vibration and shock. *AGARD Conference Proceedings No. 253*, pages 6–10, 1978.
- [37] C. W. Suggs, C. F. Abrams, and L. F. Stikeleather. Application of a damped spring-mass human vibration simulator in vibration testing of vehicle seats. *Ergonomics*, 12:79–90, 1969.
- [38] Y. Wan and J. M. Schimmels. A simple model that captures the essential dynamics of a seated human exposed to whole body vibration. *Advances in Bioengineering, ASME*, 31:333–334, 1995.
- [39] P. E. Boileau, S. Rakheja, and X. Wu. A body mass dependant mechanical impedance model for application in vibration seat testing. *Journal of Sound and Vibration*, 253(1):243–264, 2002.
- [40] R. Muksian and C. D. Nash. A model for the response of seated humans to sinusoidal displacements of the seat. *Journal of Biomechanics*, 7:209–215, 1974.
- [41] W. Quassem, M. O. Othman, and A. Abdul-Majeed. The effects of vertical and horizontal vibrations on the human body. *Medical Engineering Physics*, 16:151–161, 1994.
- [42] H. Mertens. Nonlinear behavior of sitting humans under increasing gravity. *Aviation, Space, and Environmental Medicine*, 49(1):287–298, 1978.
- [43] S. D. Smith. The development of a lumped-parameter model for simulating the vibration response of the human body. Technical Report RTO-MP-20, AC/323(HFM)TP/7, Air Force Research Laboratory, 1999.

- [44] D. P. Garg and M. A. Ross. Vertical mode human body vibration transmissibility. *IEEE Transactions on Systems, Man, and Cybernetics*, SMC-6(2):102–112, 1976.
- [45] T. C. Gupta. Identification and experimental validation of damping ratios of different human body segments through anthropometric vibratory model in standing posture. *ASME Journal of Biomechanical Engineering*, 129:566–574, 2007.
- [46] Z. Yue and J. Mester. A model analysis of internal loads, energetics, and effects of wobbling mass during the whole-body vibration. *Journal of Biomechanics*, 35:639–647, 2002.
- [47] Dean C. Karnopp, Donald L. Margolis, and Ronald C. Rosenberg. *System Dynamics: Modeling and Simulation of Mechatronic Systems*. Wiley, 2006.
- [48] W. S. Snyder. *Report of the Task Group on Reference Man*. Pergamon Press, 1974.
- [49] D. Dalecki, S. Z. Child, and C. H. Raeman. Effect of exposure duration on lung hemorrhage from low-frequency underwater sound. *Journal of the Acoustical Society of America*, 116(4), 2004.
- [50] A. B. DuBois, A. W. Brody, D. H. Lewis, and B. F. Burgess. Oscillation mechanics of lungs and chest in man. *Journal of Applied Physiology*, 8:587–594, 1956.
- [51] P. M. Morse and K. U. Ingard. *Theoretical Acoustics*. McGraw-Hill Book Company, 1968.

Vita

Sarah Gourlie was born on January 31, 1984 and raised in Wethersfield, Connecticut along with her brother Donald, by her parents William and Kathleen Gourlie. She graduated from Wethersfield High School in 2002 and recieved her Bachelor of Science in Mathematics from American University in May 2006. She was admitted to The University of Texas at Austin in the Fall of 2006. In Fall 2008 she will become employed by the Office of Naval Intelligence.

Permanent Address: 84 Judd Road
Wethersfield, CT 06109

This thesis was typeset with $\text{\LaTeX} 2_{\epsilon}$ ¹ by the author.

¹ $\text{\LaTeX} 2_{\epsilon}$ is an extension of \LaTeX . \LaTeX is a collection of macros for \TeX . \TeX is a trademark of the American Mathematical Society. The macros used in formatting this thesis were written by Dinesh Das, Department of Computer Sciences, The University of Texas at Austin, and extended by Bert Kay, James A. Bednar, and Ayman El-Khashab.

Copyright
by
Paul Allen Waters
2008

**Two-Dimensional Microscopic Model of Lung Tissue
Response to Acoustic Excitation**

by

Paul Allen Waters, B.S.

THESIS

Presented to the Faculty of the Graduate School of
The University of Texas at Austin
in Partial Fulfillment
of the Requirements
for the Degree of

MASTER OF SCIENCE IN ENGINEERING

THE UNIVERSITY OF TEXAS AT AUSTIN

December 2008

**Two-Dimensional Microscopic Model of Lung Tissue
Response to Acoustic Excitation**

APPROVED BY

SUPERVISING COMMITTEE:

Mark F. Hamilton, Supervisor

Mark S. Wochner

Dedicated to the 2006 Texas 4000 Rockies Team,
the most magnanimous group of people I have ever known.

Acknowledgments

I am deeply indebted to the careful attention and thoughtful advisement of my supervising professor, Dr. Mark Hamilton. His guidance, perception, and patience proved to be my guiding light in turbulent times. I would also like to thank Dr. Mark Wochner for his day to day assistance with all things lung related. His patience and suggestions provided me with the insight required to complete this work. Thanks to Dr. Yurii Ilinskii for his help on this thesis. I will always admire his brilliant ability to observe the simplest connections between two vastly different things. Thanks to Dr. David Blackstock. As a student in his course, I learned the importance of clarity, detail, and pedagogical reproduction. He is the best and hardest teacher I have ever known.

Lastly I would like to thank my parents, Michael and Laura Waters. There are not enough words to describe my appreciation for their love, sacrifice, and support. I only hope this accomplishment can be a small measure of their success and my gratitude.

This work was supported by the Office of Naval Research and the Cockrell School of Engineering Thrust Fellowship.

Two-Dimensional Microscopic Model of Lung Tissue Response to Acoustic Excitation

Paul Allen Waters, M.S.E.
The University of Texas at Austin, 2008

Supervisor: Mark F. Hamilton

This thesis describes a two-dimensional discrete element model of lung tissue designed to investigate micromechanical tissue strains induced by macroscopic hydrostatic excitation of the lung. The overall goal of this work is to develop a tool which may assist in determining damage thresholds for submerged divers exposed to high-intensity low-frequency acoustic waves by providing a better means to visualize deformation of the tissue than current three-dimensional models. The model utilizes a square cell geometry consisting of four point masses and six interconnecting spring elements as its fundamental unit. The geometry is motivated by the morphometry of lung tissue. The constitutive relationship used for each spring element is motivated by elasticity of collagen and elastin fibers in the parenchyma. The anisotropic elastic moduli are derived as a function of the bar element spring constant and the total strain induced on the cell (hydrostatic and shear strain). A survey of damage modes of the lung is included in the thesis and concludes that hemorrhage along the lung tips and at the rib-lung interface is a likely damage

mechanism induced by high-intensity low-frequency acoustic excitation of the lung. A visualization of the response of the lung tips and rib-lung interface to hydrostatic deformation is developed and demonstrated.

Table of Contents

Acknowledgments	v
Abstract	vi
Chapter 1. Introduction	1
Chapter 2. Biology	4
2.1 The Respiratory System	4
2.2 The Lung	7
2.3 Alveoli	8
Chapter 3. Mechanical Properties of the Lung	11
3.1 Volume Pressure (VP) Relationships	12
3.2 Volume Limits	13
3.3 Elasticity and Hysteresis	15
3.3.1 Tissue Response	16
3.3.2 Surface Forces	18
3.3.3 Collapsing Airways	19
3.4 Macroscopic Effects	20
3.4.1 Gravity Suspension	21
3.4.2 Support Cell Distribution	21
Chapter 4. Lung Modeling	24
4.1 Modeling Approaches	24
4.1.1 Static vs. Dynamic Modeling	25
4.1.2 Forward, Inverse, and Black Box Modeling	26
4.1.3 Microscopic vs. Macroscopic Modeling	27
4.1.4 Fung's Approach	28
4.2 Review of Models in the literature	29

4.2.1 Alveolar Geometry	29
4.2.2 Geometrical Arrangement and Materials of Construction	33
Chapter 5. Model Assumptions	45
5.1 Scenario	46
5.2 Damage Mechanisms	49
5.3 Model Geometry	58
5.3.1 Motivation for a two-dimensional model	59
5.3.2 Chosen Geometry	59
5.4 Material Properties	83
5.5 Boundary Conditions	85
5.5.1 Pleural Lining	85
5.5.2 Lung Tips	86
5.5.3 Rib-Lung Interface	87
Chapter 6. Numerical Model	90
6.1 Discrete Numerical Analysis	90
6.2 Excitation Methods	93
6.2.1 Lung Tips	93
6.2.2 Rib-Lung Interface	95
6.3 Graphical Interpretation	97
Chapter 7. Summary and Conclusions	102
Bibliography	106
Vita	116

Chapter 1

Introduction

A considerable amount of research has been focused on connecting the microscopic structures of lung parenchyma to the macroscopic properties of the lung. The first paper of the modern era, published in 1970 by Mead et al. [1], utilized tessellating geometries to bridge the dynamic properties of the lung with morphometric information in an effort to investigate stress distribution in the lung. Finite element methods were introduced into the field by West and Matthews [2] in 1972. In 1980, Dale et al. [3] generated the first model of a single alveolus. Notable research on lung modeling has been performed in a series of papers by Denny and Schroter [4–7] who have produced a three-dimensional model of an alveolar duct using a 14-sided polyhedron as the fundamental unit. Each of these models is developed to improve basic understanding of lung mechanics. Fundamental understanding of lung mechanics lends itself to numerous applications.

In 2002, a technical report released by Applied Research Laboratories [8] investigated the feasibility of non-lethal diver deterrent technologies for application to submerged divers. The report, which reviewed common technologies used by law enforcement, concluded that high-intensity low-frequency

acoustical technology is one feasible option for a non-lethal underwater diver deterrent system. Given the relatively low attenuation in water and the nearly equivalent acoustic impedances of tissue and water, acoustic waves in water can travel great distances and penetrate targets in such a manner to cause discomfort and disorientation.

More recently, a group of researchers at the Applied Research Laboratories of the University of Texas at Austin have begun an investigation of tissue damage thresholds for high-intensity low-frequency acoustic excitation of submerged divers as reported in a series of meeting abstracts. [9–14] The work has focused primarily on the development of a model capable of indentifying lung damage thresholds since the lung is intrinsically fragile by nature. The model derived in this thesis is intended to be a visualization tool for observing deformation at the micromechanical level along regions most affected by hydrostatic excitation of the lungs. Some preliminary work by Diane Dalecki [15] revealed that acoustic excitation near lung resonance causes lung hemorrhage in submerged mice for sound pressure levels between 160 and 190 dB (re 1 μ Pa). The biological differences between man and mice, and the lack of understanding about why and how damage occurs in the lungs illustrates a need for further research into human lung bioresponse to low-frequency acoustic excitation for the development of successful acoustic non-lethal diver deterrent systems.

The purpose of this thesis is to develop a two dimensional lung model which examines the connection between macroscopic hydrostatic deformation

of lung tissue and the micromechanical strain on alveolar units. This model can potentially be used in conjunction with macroscopic models which couple human lung response to underwater acoustic excitation in order to obtain a better understanding of lung damage induced by low-frequency excitation underwater. This thesis consists of six chapters. Chapter 2 examines the biology of the human respiratory system with emphasis on the geometric features which are relevant to the development of a lung tissue model. Chapter 3 details important mechanical features of the lung on both a macroscopic scale (the volume-pressure relationship) and the microscopic scale (single fiber elasticity). Chapter 4 reviews the history of lung modeling techniques. This chapter illustrates the methodologies commonly used in the field of modern lung mechanics to solve the problems associated with tissue modeling including geometry, tissue constitutive relationships, and assumptions regarding surface tension. Chapter 5 begins the development of the two-dimensional lung tissue model. At the beginning of the chapter, focus is placed on identifying the purpose of the model. Next the single cell geometry is analyzed in detail to obtain generalized constitutive relationships. To conclude the chapter, a model of two lung structures (the lung tip and the rib-lung interface) is proposed and discussed. Finally, Chapter 6 outlines the numerical method used to solve a dynamic excitation of each structural model and the graphical representation of the stresses and strains.

Chapter 2

Biology

The anatomy and physiology of the respiratory system are documented extensively in biological and medical texts. Since the aim of this thesis is to generate a mechanical model of lung tissue, this section presents only the relevant biology necessary to understand the basic assumptions used to develop the model. The discussion begins with basic anatomy and physiology of the human respiratory system, followed by a discussion of lung tissue structures and alveoli.

2.1 The Respiratory System

The primary function of the human respiratory system is to provide adequate oxygen to the body's tissues and to dispose of carbon dioxide. The system is divided into two regions, the upper and lower respiratory tracts. The upper tract is composed of the mouth and nose, nasal turbinates, pharynx, and larynx. The lower respiratory tract is made up of the trachea, main bronchi, and the lungs. Figure 2.1 illustrates the location of each structure of the respiratory system within the body.

The respiratory system works in a cyclic breathing pattern, pulling air

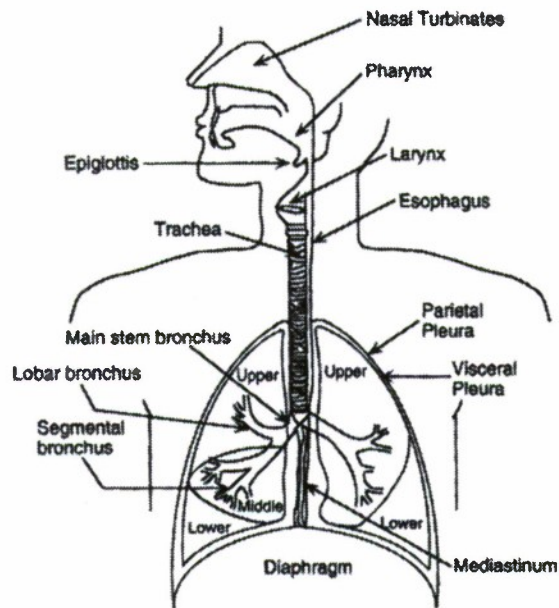


Figure 2.1: Illustration of the major features of the human respiratory system, taken from Hlastala and Berger. [16]

in during inspiration, and forcing air out upon expiration. During inspiration, the chest cavity is pulled open by the diaphragm at the bottom of the lung and the intercostals between the ribs. This expansion lowers the intra-alveolar pressure, which draws air in from the atmosphere, through the respiratory tracts, to the lungs. During expiration, the natural recoil of the lung tissue and ribcage typically provides the force to push air out of the lungs. In active breathing, the abdominals, intercostals and diaphragm compress the cavity to expel air. Figure 2.2 illustrates the muscles involved in breathing.

Between each lung and its surrounding structures, there are two thin

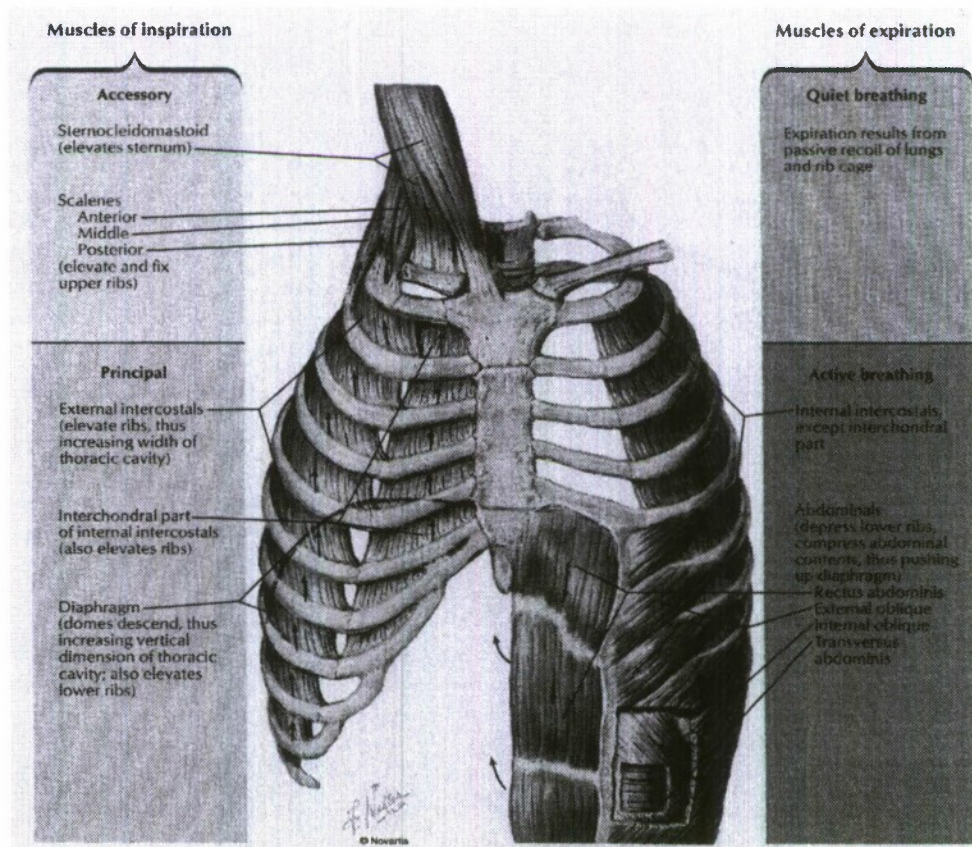


Figure 2.2: Illustration of the muscles attached to the ribcage that aid in respiration, taken from *Atlas of Human Anatomy* by Netter. On the left: muscles used in inspiration. On the right: muscles used in expiration. [17]

tissue layers known as the parietal pleura and visceral pleura. The visceral pleura attaches to the parenchyma tissue via the pleural connective tissue, while the parietal pleura attaches to the surrounding structures. These layers are actually one continuous piece of tissue that forms a thin sac around each lung. There is a small amount of fluid between the pleura that allows the lung to slide freely against the chest wall, heart, and arteries; each pleural sac also maintains a negative pressure on the cavity to overcome the surface tension within the lung and prevent collapse.

2.2 The Lung

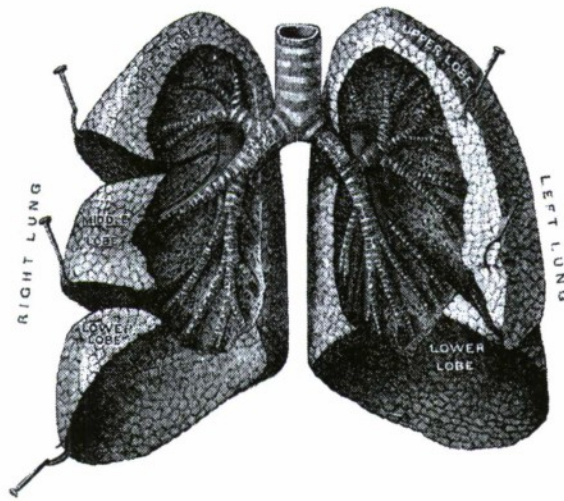


Figure 2.3: Illustration of human lungs with large bronchi exposed, taken from Gray. [18]

There are two lungs in the human body, which are located in the thoracic cavity between the ribs and the heart (see Figure 2.1). The left lung has

two lobes, while the right lung has three lobes (see Figure 2.3). The structure of each lung begins at the bifurcation of the trachea into two main bronchi. Each main bronchus bifurcates into smaller generations, feeding the lobes of each respective lung, until it terminates at an alveolar sac (see Figure 2.4).

There are approximately twenty-three total generations of bronchi. The first sixteen generations are known as conducting airways and consist of bronchi, bronchioles, and terminal bronchioles. These columnar airways contain either c-shaped cartilage structures or smooth muscle fibers to help them remain open during intense respiration. There are no sites of gas exchange in this region. The remaining seven generations are known as the respiratory airways. These bronchioles number in the hundreds of thousands to more than eight million at the final bifurcation. At the 17th generation, alveoli begin to protrude from the columnar structure of the bronchi. By the last few generations the airway is composed only of alveolar mouths. These airways are known as alveolar ducts, while the collection of alveoli around the duct is known as an alveolar sac.

2.3 Alveoli

As the smallest and most abundant tissue structure in the lung, alveoli are the site of gas exchange in the body. They are tiny air-filled sacs ventilated through respiratory bronchioles and packed tightly together to form the parenchyma. Several morphometric estimates predict that there are more than 250 million alveoli in the adult human lung. [20–22] The average size of

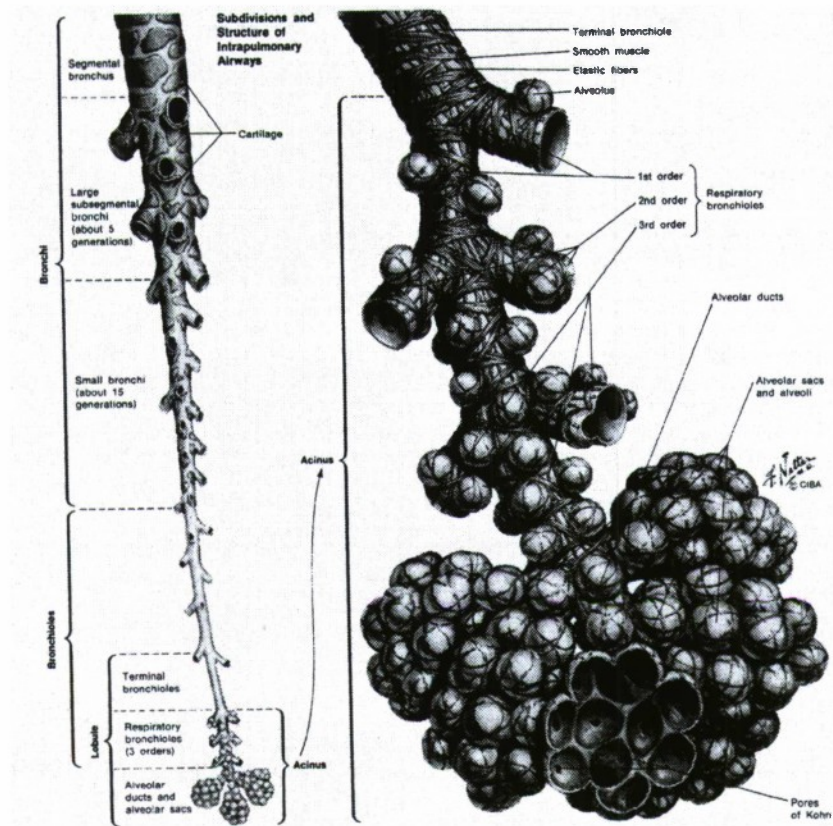


Figure 2.4: Illustration of a single airway from bronchus to alveolar sac with exploded view of the acinus, taken from volume 7 of the *The Ciba Collection of Medical Illustrations* by Netter. [19]

an alveolus is around 300 microns at 75% lung volume. [16] Alveolar walls, unlike bronchiole walls, are characterized by a squamous epithelium and are covered by a thin layer of surfactant to reduce the surface tension. Alveoli are ingenuous structures which help maximize the capillary surface area to air volume ratio for optimal gas exchange within the lung; in an adult human lung there are approximately 70 m^2 of alveolar surface at 75% lung inflation. [22]

The membrane around alveoli contains several cell types to promote gas exchange, circulate blood, and maintain shape for optimal lung performance. Most alveolar walls within the parenchyma are shared by two alveolar spaces and are known as alveolar septum. These quasi-planar features are only a few microns in thickness and contain networks of capillaries, support tissues, and macrophages. Each alveolar membrane connects to other septum at thicker junctions known as septal borders, where larger networks of support cells and circulatory cells reside. [23]

Chapter 3

Mechanical Properties of the Lung

The history of lung mechanics extends back to 1849, when Donders published an article on the major structures of the human lung. He was the first to note that inflated lungs collapse from their own elastic forces and that the force of retraction increases with increasing airway pressure. [24] Since that time, extensive experimental and theoretical work has been dedicated to characterizing the elastic properties of healthy and diseased lungs. This section aims to present the important mechanical features of the lung, as presented in the literature, necessary to develop the author's model.

Experimental observations can be divided into two types: those measured *in vivo* and those measured *in vitro*. *In vivo* measurements, taken from living subjects, are natural observations that provide important information about the respiratory system as a whole. While *in vivo* experiments provide certain key information about the natural state of the lung, the most useful experiments are performed *in vitro*, using excised lungs. The advantage of using excised lungs is that researchers can attribute mechanical behavior directly to tissue properties without having to rule out effects due to gravity suspension in the chest cavity, reaction of the chest wall, uneven pleural pressure, or in the

case of dried lungs the surfactant along the alveolar walls. Most of the features discussed in the following sections are *in vitro* observations, but important *in vivo* observations are also highlighted.

3.1 Volume Pressure (VP) Relationships

The very first volume pressure relationships for human lungs were published by Hutchinson [25] in the 1850's. He measured lung volume as a function of trachea pressure for two excised human lungs immediately post mortem. While Hutchinson's curves were ultimately incorrect and only showed measurements for the inflation of the lung, they provided the first tools for extrapolating mechanical characteristics of lung tissue. [24]

In the 1950's, researchers adopted consistent methods for measuring VP curves in excised lungs. As a result of these methods and the introduction of electronic data recording devices, common features appeared in measurements from many different species and researchers. [26–28] Figure 3.1 illustrates a representative pressure volume curve of an excised dog lung. The volume is presented as a percentage relative to the total volume at the maximum pressure measurement (30 cmH₂O, 3 kPa) to allow for comparison with lungs of different sizes. Each data point was taken by progressively increasing or decreasing the tracheal air pressure at discrete intervals, waiting several minutes, and measuring the volume. The arrows on the plot indicate the time history of pressures used to measure the data. This method eliminates relaxation forces from the measurement to show the average mechanical properties of the entire

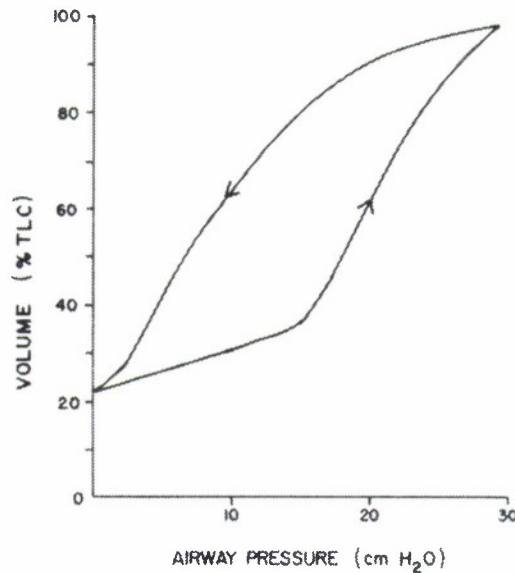


Figure 3.1: Representative static volume-pressure curve of an excised dog lung for a cycle from 0 cmH₂O to 30 cmH₂O, taken from Hoppin and Hildebrandt. [29]

organ. Several features of the plot indicate certain characteristics about the lung and its tissues. These properties are discussed in detail below. The following section defines some characteristic volumes that are used commonly in the field of lung research.

3.2 Volume Limits

The upper and lower limits of the volume pressure curve indicate the maximum and minimum volumetric size of the lung. At the maximum lung volume, or total lung capacity (TLC), further increase in pressure shows negligible increase in volume and may cause rupture of the tissue. Most researchers

attribute the sudden volume limit experienced during *in vitro* measurements to a network of inextensible collagen fibers found throughout the lung. [29] *In vivo*, the intercostal muscles, ribcage and diaphragm also provide support. At the lowest lung volume, tiny airways in the bronchiole tree collapse, trapping air inside the lung; [30,31] reducing pressure below this limit only causes the larger airways of the bronchiole tree to collapse without extracting any of the trapped air.

While Figure 3.1 illustrates an *in vitro* measurement of an entire lung volume cycle, it is important to note that the lungs do not typically operate from bronchiole collapse to TLC *in vivo*. Respiratory scientists have defined a number of terms to describe mammalian breathing patterns. Figure 3.2 illustrates the definitions of respiratory nomenclature with reference to a typically mammalian breathing cycle. During relaxed inactive breathing, a person begins inspiration at the functional residual capacity (FRC) and breathes a regular amount of air known as a tidal volume (V_T). When a full breath is taken, such that the lungs are fully expanded, TLC is reached. The maximum volume of air expelled from TLC is known as the vital capacity (VC). The maximum amount of air expelled from FRC is known as the expiratory reserve volume (ERV), and the volume remaining in the lungs after complete forced exhalation (from TLC or FRC) is known as the residual volume (RV). While it may seem that the low volume limit in excised lungs should correspond to RV, the method of obtaining the value is dissimilar. *In vitro* measurements reduce pressure on the lungs through the trachea, while *in vivo* the chest cavity and

diaphragm force air out of the lungs. The differences may be subtle, but a connection cannot easily be inferred.

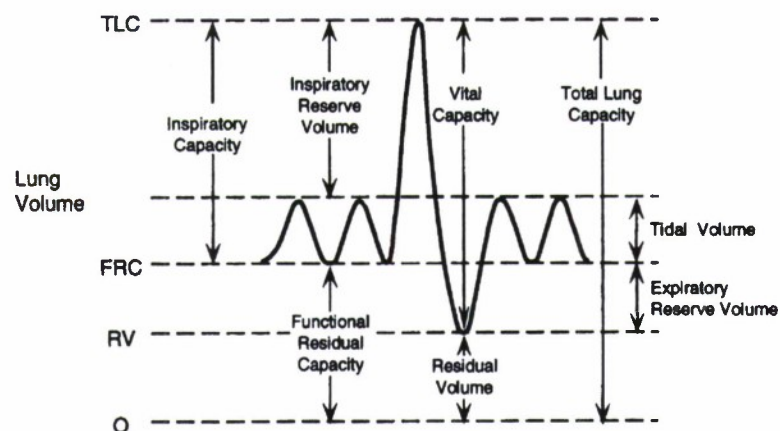


Figure 3.2: Typical mammalian breathing pattern denoted by lung volume nomenclature, taken from Hlastala and Berger. [16]

3.3 Elasticity and Hysteresis

In Figure 3.1 the volume and pressure loops around in the given pattern, returning to the same value over a cycle. This looping relationship is known as a thermodynamic cycle. This resilient part of the cycle is known as elasticity in mechanics. However, in Figure 3.1 there is a distinct separation of pressure experienced at a given volume depending on whether the lung is in the process of inflating or deflating. The relationship between pressure and volume in the lung is therefore dependent on the time history of the process, known as hysteresis. The elastic nature of the curve is typically attributed

to tissue elasticity from deformation of the parenchyma. The hysteresis is believed to be caused by surface tension along the alveolocapillary membrane, inelasticity in tissue, and, at low lung volumes, the reopening of collapsed airways during respiration. The following sections review the role of tissue response, surface tension, and collapsing airways in the nonlinear, hysteretic relationship between volume and pressure in the lungs.

3.3.1 Tissue Response

Observations about tissue elasticity date back to Donders' original publications when he noted that excised, inflated lungs tend to collapse from the recoil of the tissue. [24] Over 150 years later, an extensive volume of work has identified and characterized the primary contributors to elastic recoil in the tissue. The literature agrees that the stress bearing constituents within the lung are fibrous proteins known as elastin and collagen. [32] These fibers are distributed throughout the lung in alveolar ducts, septa, septal borders, and in the pleura. Fibers located in the alveolar parenchyma are believed to be the primary recoil force in the lung, although some research [33–35] contends that fibers in the pleural tissue may contribute up to 20% of the resistive force *in vivo*.

Collagen and elastin fibers have drastically different characteristics. In 1962, Carton et al. measured the stress-strain properties of 5 single elastin fibers extracted from the ligamentum nuchae of an ox. [36] The group reported the maximum strain of a single elastin fiber to be approximately 130% of its

unstretched length. In addition to maximum strain, Fung reports the Young's modulus of elastin to be 0.6 MPa. [37] These properties characterize elastin as a highly extensible fiber with a relatively significant resistance. Fung contends that elastin has a larger Young's modulus than the ground substance, smooth muscle or any other cell-type within the parenchyma. [37]

Compared to elastin, collagen is extremely stiff and inelastic. In 1969, Stromberg and Wiederhielm measured the stress-strain response of collagen fibers extracted from the tails of Swiss-Webster mice and found the maximum strain of the fiber does not exceed around 2%. [38] Additionally, Fung reports that collagen has a Young's modulus of around 1000 MPa, more than 3 orders of magnitude greater than elastin. Due to its highly inextensible and resistive nature compared with elastin or any other tissue in the lung, collagen fibers likely provide support only at maximal lung volumes. [23, 29]

In addition to elastic response, support structures within the parenchyma have been shown to exhibit hysteretic behavior themselves. Fukaya et al. [39] demonstrated the hysteretic nature of tissue parenchyma by stretching excised strips of cat lung, submerged in a saline solution, by up to 90% of the original length. By extending the time scale of the experiment to remove time-dependent stress relaxation from the behavior, a small amount of hysteresis still remained in the strain-force relationship. [39] Hoppin et al. reported similar results when stretching cuboidal blocks of excised lung tissue in dogs. [40] Though small, this type of hysteresis acts over the entire range of tissue stretch.

3.3.2 Surface Forces

In 1929, Neergaard was the first to call attention to the role of surface forces in lung tissue recoil. [24] He proposed that a bubble on the end of a tube is analogous to an alveolus at the end of a bronchiole. Geometrically, a bubble is simply a sphere truncated by a disc. Therefore Neergaard argued that the pressure exerted by the surface is given simply by [24]

$$P = \frac{2\gamma}{r}, \quad (3.1)$$

where P is pressure, γ the surface tension, and r is the radius. Based on these calculations, he determined that the surface tension should cause alveolar collapse. Since the phenomena would not be limited to a single alveolus, these predictions imply that entire sections of the lung may collapse, which is known as atelectasis. The inherent instability of this kind of system led Neergaard to propose the existence of a pulmonary surfactant, which reduces the magnitude of surface tension along the alveolocapillary membrane to allow for normal lung function. Thirty years later, Pattle and Clements confirmed this hypothesis when they discovered a substance inside of lung edema fluid that significantly reduced surface tension. [41]

Following his postulation, Neergaard wanted to test the relative contribution of surface tension to the elastic recoil. He measured VP curves for lungs inflated with air and then with liquid. In liquid-filled lungs, the role of surface tension is almost completely eliminated. Therefore, VP curve comparison with air-filled lungs allows for an estimate of the relative contribution

of surface tension to the recoil of lung tissue. Neergaard's experiment has become a standard technique, repeated by several authors, for measuring relative force and pressure contributions of surface tension on elastic recoil. The original experiment was performed with excised sheep, pig, and human lungs. Neergaard reported that surface forces generate between $2/3$ and $3/4$ of the total resistive pressure in lung recoil. [24]

Since the addition of surface forces to lung mechanics, a great deal of understanding has been gained about the role of surface tension and surfactant in the normal function of the lung. However, debate still exists about the relative contribution surface tension provides to the restoring force *in vivo*. [42] Since the force contribution from surface tension is proportional to the curvature of a membrane, a purely two-dimensional model cannot incorporate the phenomena. Therefore, a more detailed discussion of surface tension is neglected. For more information about surface tension, the author recommends a review by Fung [43], or for surfactant, a review by Hamm et al. [41]

3.3.3 Collapsing Airways

In 1882, Heynsius [44] noticed that once parts of an excised lung had collapsed, inflation was uneven and depended upon the number of open ducts and alveoli. In 1907, Leibermeister [24] made similar observations by inflating excised and collapsed cat lungs, noting that a critical pressure seemed to exist, around 8-10 cmH₂O (780-980 Pa), where the collapsed alveoli would reopen and volume would increase rapidly with small increases in pressure. These

results indicate that a significant hysteresis in the VP relationship of lungs can be attributed to collapsing airways in the tissue.

During a full breath, air fills the lung up to, or near, TLC. Upon expiration, lung volume decreases along with the characteristic dimensions of the microscopic parenchyma structure. At some critical transpulmonary pressure, known as closing pressure (CP), airways begin to close, trapping gas in the dependent regions of the parenchyma. While some debate exists in the literature about the value of the CP, [30, 45, 46] each author agrees that upon reinflation from pressures below CP, pressures exceeding CP are required to reopen closed airways. This state-dependent discontinuity contributes significantly to the hysteresis evident in VP curves for breathing cycles that reach an end-expiratory pressure below CP. Very few models of alveolar recruitment have been generated, and therefore the author assumes that the operating range examined in the model does not include end-expiratory pressures below CP.

3.4 Macroscopic Effects

In addition to the forces discussed in the previous section, there are two important macroscopic effects observed and discussed within the literature on lung mechanics: the gravity suspension of the lung, and the distribution of support cells within the parenchyma. This section discusses each of these factors and relates their contributions to the author's model.

3.4.1 Gravity Suspension

When a human is standing upright, a vertical gravity-related pressure gradient exists within the lung. [29] *In vivo* the lung is attached to the surrounding tissue only through the hilum, but it is also suspended within the chest cavity by the transpulmonary pressure difference between the alveolar cavities and the pleural space. Therefore spatial gradients in tissue deformation must compensate for the uneven pressure from apex to base. Evidence from frozen dog lungs shows a fourfold difference in volume from apex to base with the dog in head up position. [2] Evidence from radioactive gas measurements, taken from a standing man, also shows that alveoli at the bottom of the lung (near the diaphragm) have a small resting volume and large volume change on inspiration relative to the upper regions of the lung (near the trachea). [2] Though the literature emphasizes this effect, the author is attempting to model a diver's lung whose orientation is likely prone. In this position, the differences between the apex and base of the lung are much smaller and therefore the effect is neglected.

3.4.2 Support Cell Distribution

The distribution of collagen and elastin within the lung provides some additional knowledge about the expected tissue response to deformation. Prior to 1988, several authors believed that most of the elastin in the human lung was located in the alveolar ducts and mouths. This belief was confirmed by experiments on canines and rats. [23, 47] However, in 1988, Sobin, Fung and

Tremer [48] examined the distribution of collagen and elastin fibers in 34 excised human lungs. They showed that most of the elastic fibers in human lungs are actually located in the alveolar septa, rather than in the mouths and ducts. In 1990, Mercer and Crapo [47] confirmed this observation by examining lungs from rats and humans. Their results showed that elastin was more prevalent in the alveolar septa of humans and in the alveolar ducts in rats. Mercer et al. [49] explain, in a more recent paper, that species with larger alveoli require a more substantial tissue support structure due to a smaller contribution from surface tension than lesser endowed species. This observation implies that species with heavier lungs contain more support structure around the alveoli than species with less massive lungs. In the most extreme case of an elephant, the alveoli are compartmentalized by thick elastic septa extending from an even thicker pleural connective tissue (composed of elastin) which encases lung. Brown et al. [50] believe this evolutionary development is compensation for a greater gravitational force acting on a very long lung. In the case of humans, elastin is believed to be the primary support mechanism at regular lung volumes, [23, 29] and since elastin is more densely packed in the alveolar septa, the measured elasticity of human lung tissue should be attributed primarily to deformation of the alveolar septa. [29]

This chapter has provided a review of the known mechanical features of mammalian lungs which are to be incorporated into a model of lung parenchyma. The next chapter will review the history of lung modeling to date and outline an approach for a model of submerged lung tissue exposed to low-frequency

acoustic excitation.

Chapter 4

Lung Modeling

Modern lung modeling techniques date back to 1970, when Mead et al. [1] examined stress distribution in the lungs by supposing the tissue is an elastic network of interconnected membranes idealized as springs. Since then, numerous lung models have been developed to investigate particular behavior observed in health and disease. This chapter presents a review of lung models within the literature. The discussion is broken into two sections. The first reviews general modeling methods. The second reviews specific applications of these methods as found in the literature on lung modeling.

4.1 Modeling Approaches

There are many different ways to approach a modeling problem; therefore, it is important to understand the merits of each model type in order to select the most appropriate methodology. This section examines several methodological choices in lung modeling as well as presents Fung's [43] basic outline for generating a lung tissue model.

4.1.1 Static vs. Dynamic Modeling

In the literature on lung mechanics, models typically examine either the static elastic response of lung tissue or the dynamic mechanical impedance during a breathing cycle. [42] In a static approach, the objective of the model is usually to derive elastic constants of lung tissue, like bulk and shear modulus. Initially, these models are derived from an assumption that the tissue is an elastic continuum or that finite element methods can be used, primarily to incorporate inhomogeneity. Next, a geometric structure is generated to represent the tissue. The model is then deformed, in an appropriate manner, to obtain an incremental stress-strain relationship that can be used to derive elastic constants. Finally, the derived constants are compared to similar experimental observations to determine model accuracy.

Dynamic models are typically used by lung researchers to examine the change in mechanical impedance of the airway, usually with some frequency dependent excitation. This type of model can help characterize the effects of inhomogeneity that occur from gravity loading or uneven pleural pressure. Dynamic models can also be used to investigate impedance changes for increased breathing amplitude or for different operating volumes. The author utilizes a static approach and therefore very little attention is given to dynamic models of lung tissue in the following sections.

4.1.2 Forward, Inverse, and Black Box Modeling

Another concern in modeling is how to use known information about the lungs to construct a model that outputs useful data. Three approaches used in the literature are forward, inverse and black box modeling.

A forward model is generated using empirical values and constitutive equations obtained from isolated experiments on various tissue components. These components are used to construct a geometrical representation of the lung or a portion of the lung. The model is then tested and results are compared to experimental data for the modeled structure (often volume-pressure curves for the entire lung). Static lung models typically use a forward approach. [42]

Inverse models begin with a general structure composed of elements that are characterized by free parameters. The parameters are then adjusted until the response of the model mimics the response of the system under study. Dynamic models of lung tissue typically use an inverse approach. [42]

Inverse models are similar to forward models in that each modeling approach uses physiological information about the system to generate a reasonable structure. Black box modeling, on the other hand, assumes very little about the structure of the system and focuses primarily on obtaining a transfer function between the system input and output. Very few black box models have been utilized in lung modeling. [42] Therefore, the author omits further review of these models. For more information about black box modeling ap-

plications in lungs research, see Maksym. [42]

4.1.3 Microscopic vs. Macroscopic Modeling

The purpose of this work is to develop a model of tissue damage mechanisms within lung parenchyma due to an acoustic excitation of the lung. The damage mechanisms under study are on the microscopic scale reaching alveolar dimensions while the excitation occurs at a macroscopic scale, the size of the lung. Therefore the model must appropriately connect microscopic deformations with macroscopic excitation.

At the micromechanical level, researchers attempt to simulate lung parenchyma, either as a continuum or as a finite section along an interface (e.g., an alveolar duct or rib). These models require detailed information about parenchyma morphometry, the distribution of support tissue, and the role of surface tension in lung dynamics. If the information is incomplete, a reasonable assumption must be made to obtain an accurate model. Micromechanical static models in the literature either use a finite-element approach, which assumes various size/shape distributions to describe the tissue, or they use analytically solvable geometrical configurations, like spheres or cylinders.

At the macroscopic level, models must capture either the characteristic volume-pressure relationships reported throughout the literature, or the stress-strain behavior measured from samples of parenchyma. In order to achieve this type of comparable data from a micromechanical structure, authors in the literature take one of two approaches. The analytical continuum models

utilize appropriate averaging schemes, [43] while finite element models typically assume that the volumetric strain vs. pressure curve of the micro-scale model is directly proportional to the volume-pressure curve of the entire lung. [32]

4.1.4 Fung's Approach

When writing a review of lung models, it would be insufficient to neglect mention of one of the greatest contributors to the field of lung mechanics. Fung is popularly known as the "Father of Biomechanics" [51] and his work with lungs has been particularly revolutionizing. In his treatise on biomechanics, [43] Fung presents a complete guide to generating detailed lung models. His focus in the discussion is on the connection between the mechanical properties of individual alveoli and the mechanical properties of the entire lung. The approach is broken into 5 steps: [43]

1. Identify the geometry of the alveoli and/or alveolar ducts.
2. Identify the materials of construction and the geometric configurations of the materials.
3. Determine the rheological properties of the materials of construction and the interfacial energy or surface tension.
4. Derive the constitutive equations of the alveolar walls, alveolar mouths, and the lung parenchyma.
5. Validate the derived constitutive equations and solve useful problems of the lung.

Each step requires adequate experimental data, rigorous theoretical derivation, or ad hoc hypothesis. For the author's model, surface tension is neglected; therefore step 3 is eliminated from the process. The following sections review several popular approaches used to solve these steps in the literature.

4.2 Review of Models in the literature

Section 4.1 discussed the most common modeling approaches used by lung researchers. This section demonstrates the manifestation of these approaches through a detailed look at several lung models in the literature. The outline of the discussion is separated into two subsections. Section 4.2.1 discusses various choices for basic alveolar geometry. As the fundamental cellular unit of the parenchyma, this geometry has far-reaching implications to the validity and applicability of the model. Section 4.2.2 examines solutions for the geometrical arrangement of supporting structures, common formulas for structural components (elastin and collagen), and applications which incorporate surface tension.

4.2.1 Alveolar Geometry

A number of geometrical approximations have been used in models of alveoli, and alveolar ducts. Figure 4.1 illustrates several representations from the literature. The simplest representation is given by Neergaard [24] [Figure 4.1(e)], who proposed that alveoli are like tiny bubbles ventilated along a common tube structure. As mentioned in Chapter 2, this model shed light on

the contribution of surface tension to the mechanics of the lung. However, Fung showed that the model is unrealistic since it implies an inherently unstable lung. [52] The one instance in which Fung approves of Neergaard's model is along the pleural lining [Figure 4.1(f)]. [52] Neergaard's model was primarily an ad hoc approximation of lung tissues based on dated illustrations of lung parenchyma that showed alveoli hanging freely from branches of the bronchiole tree, like grapes from a vine. [43] More recent morphometric studies of the lung have shown that the outside of one alveolus is the inside of another, except of course along the pleural wall. Therefore the collapse from differential pressure between the alveoli, predicted by Neergaard, is improbable due to shared support structures.

In 1970 Mead, Takishima, and Leith [1] proposed a lung parenchyma model that is arguably the most influential model of the last 50 years. In this groundbreaking paper, they proposed that the parenchyma is composed of a network of interconnected membranes which can be modeled by an idealized network of springs or elastic membranes. They used an irregular hexagonal structure to approximate individual alveoli [Figure 4.1(e)]. In their theoretical development, this geometric assumption held very little relevance since the fine structure of the angular elements were averaged out by an assumption that the regions and deformations under study were significantly larger than alveolar dimensions. However, they tested their theoretical conclusions by creating two physical models: one composed of a network of springs arranged in a hexagonal array, and another composed of 19 condoms glued together with their primary

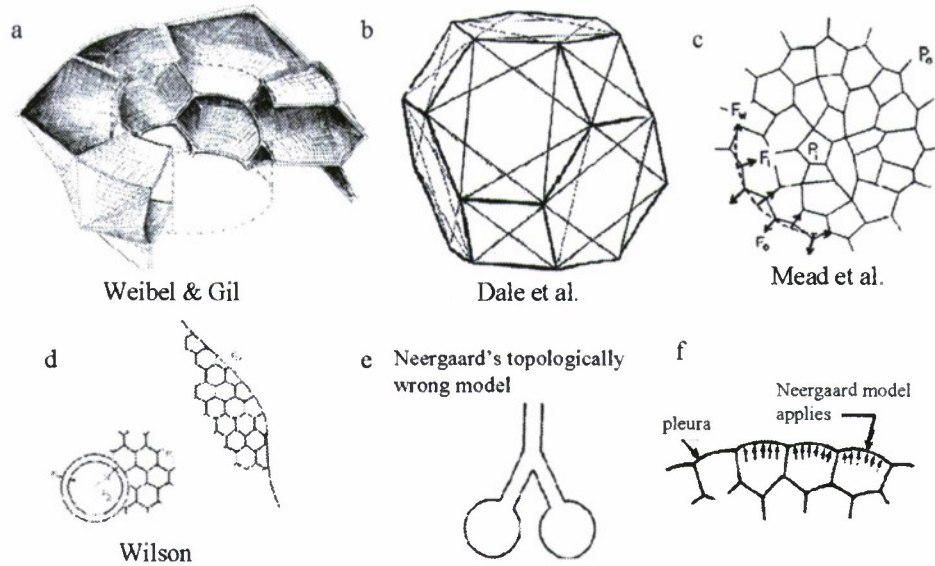


Figure 4.1: Six illustrations describing models of lung alveoli. (a) A hand-drawn image of an alveolar duct taken from Weibel and Gil's morphometric study of lungs. [22] The cylindrical dotted outline indicates a duct while each polyhedron is an alveolus. (b) An image of the tetrakaidecahedron with idealized support structure drawn across each face used to model a single alveolus, taken from Dale et al. [3] (c) An illustration, taken from Mead et al., [1] of a randomized array of hexagons used to model lung parenchyma as a continuum. (d) An illustration taken from Wilson. [53] (e) An illustration of Neergaard's proposed model of two alveoli connected to a bronchiole, taken from Fung. [52] (f) An illustration of Fung's model of the parenchyma boundary at the pleura, taken from Fung. [52]

axes in parallel. These idealized, space-filling geometrical models incorporated the concept of interdependent alveolar spaces, improving Neergaard's model and demonstrating inherent stability in lung structure. These models also confirmed that polygons and polyhedra are realistic geometries to approximate lung tissue.

Several years after the publication by Mead et al., Wilson [53] utilized a similar hexagonal arrangement to investigate the stresses surrounding an alveolar duct. His work derived constitutive equations for a thin-walled elastic tube placed in an elastic continuum of hexagonal structures. While still an incomplete model, the assumptions regarding geometry of the lung parenchyma were improved from Neergaard's original work.

Since the hexagonal model was introduced, many models in the literature have been based on tessellating regular polygon geometries. For two-dimensional models only 3 regular shapes tessellate space: a square, a triangle, and a hexagon. Most two-dimensional models within the literature use hexagonal arrays. The benefit of two-dimensional hexagonal geometry is that there are only two independent elastic moduli, which implies the system is isotropic. Therefore the derivation of standard elastic coefficients, like Poisson's ratio or Young's modulus, is trivial. In three dimensions, there are 4 regular space-filling polyhedra: the cube, the nonregular octahedron, the garnet-shaped rhombic dodecahedron, and the tetrakaidecahedron, also known as a truncated octahedron. Within the literature, cubic models are rare and considered a crude representation of the tissue. Octahedron models have re-

ceived little to no attention, while dodecahedron models are only slightly more represented. [42] To date, tetrakaidecahedron models are the dominant three-dimensional geometry used to model lung parenchyma. Morphometric studies performed by Weibel and Gil [43] [Figure 4.1(a)] showed that alveolar walls are typically hexagons, rectangles, and occasionally pentagons. Therefore, the tetrakaidecahedron, shown in Figure 4.1(b), is proven an ideal polyhedron choice since it is composed of squares and hexagons. [3, 4, 54] The first mention of the tetrakaidecahedron in lung modeling dates back to Mead et al. [1] in 1970, but it remained untested until 1980 when Date et al. [3] applied a finite element method to the lung, utilizing the tetrakaidecahedron as the fundamental alveolar unit.

4.2.2 Geometrical Arrangement and Materials of Construction

When constructing a lung model, the goal of material selection is to mimic the behavior of lung parenchyma; however, due to the complex arrangement of support structures, ground substance, liquid surfactant, and alveolar geometry, material assumptions about lung tissue properties are difficult to make. During the era of Mead et al., [1] researchers modeled the lung as an isotropic continuum using extrapolated coefficients from stress-strain measurements on macro-scale lung tissue segments. More recently, researchers have relied on finite-element approaches to incorporate complex surface forces and sophisticated fiber recruitment models into micro-scale models. This section reviews these two approaches.

One of the more notable continuum models of the lung was generated by Lambert and Wilson in 1973. [55] The model explored mathematically the concept proposed by Mead et al. that the lung is composed of a network of interconnected tissue membranes that can be modeled by an idealized network of springs or membranes. Lambert and Wilson derived continuum equations for lung tissue by averaging the stress and strain experienced by a uniformly expanded array of randomly-oriented, homogeneous, incompressible, plane elastic membranes. [55] The use of averaging allowed Lambert and Wilson to obtain both a bulk and shear modulus from the model, a requirement for the application of continuum mechanics. Lambert and Wilson presented the derived elastic parameters as functions of the membrane thickness, the prestress state, and the number of membranes per linear distance. The primary advantage of using a continuum model is the maturity of continuum mechanics. A wealth of solutions has been developed to solve a vast number of boundary value and initial value problems given a continuous media. The weakness of this model is the number of assumptions that link actual parenchyma geometry to the idealized geometry that is the foundation for the continuum derivation. Another weakness is the validity of the continuum assumption along lung boundaries, where the structure of the lung is largely affected by the boundary (e.g., along the pleura).

Since Lambert and Wilson's derivation, many different idealized geometries have been used to derive elastic constants for a continuum including cubes, spheres, dodecahedrons, and circular line elements. [42] Most of

these models included a strain energy function obtained from empirical data from tissue samples *in vitro*. In 1982, Wilson and Bachofen [35] extended the work of Lambert and Wilson by applying a similar continuum approach to modeling the alveolar duct. The primary assumption underlying Wilson and Bachofen's model was the existence of two networks of force-bearing line elements, as opposed to membrane elements. The first was an interdependent part of the peripheral connective tissue system extending from the pleura into the parenchyma. The second was a network of fibers that form alveolar mouths. They assumed the alveolar duct, formed by the mouths of alveoli, could be modeled geometrically by intersecting helical line elements. After an empirical fit, the results of the model accurately predicted surface-area relationships in the alveolar duct for lung volume between 40% and 80% total lung capacity. However, some claim Wilson and Bachofen's model, along with similar models, overestimate the shear modulus of the tissue. [42] Stamenovic and Wilson [56] improved upon Wilson and Bachofen's work by including the effects of nonuniform distortion. The resultant shear modulus estimates from the model agreed with experimental data between 20% and 80% of total lung capacity.

In 1987, Budiansky and Kimmel [57] improved upon previous continuum modeling techniques by incorporating linear incremental stress-strain behavior into line elements of a pin-jointed dodecahedron. This improvement meant the bulk and shear modulus of the model would be dependent on the level of prestress in the structure. This dependence marks a significant im-

provement on continuum modeling since experimental evidence suggests that parenchymal resistance to shear deformation increases with increasing pre-stress. [42]

As mentioned in introduction to section 4.2.2, finite element models have been the favored methodology in recent lung modeling research. The first appearance of finite element methods in lung research was in 1972, in a paper by West and Matthews [2] that investigated the effect of gravity loading on the lung. They modeled three-dimensional deformations for vertical wedges of lung tissue by breaking the system up into smaller wedges and trapezoids. They assumed the tissue to be a homogenous nonlinear elastic material by utilizing a nonlinear stress-strain relationship based on empirical relationships originally reported by Radford [26] in the 1950's. Though the model would later be improved by Liu and Lee, [42] it applied modern engineering methodology to the field of lung mechanics.

In 1980, Dale, Matthews, and Schroter [3] modeled a single lung alveolus using finite element methods. As mentioned in Sec. 4.2.1, they were the first to use the tetrakaidecahedron as geometric approximation of lung alveoli. Like previous authors, Dale et al. proposed that the mechanics of the lung can be modeled using an idealized pin-jointed geometry where forces can be averaged and applied to each node. Since the tetrakaidecahedron is composed of regular hexagons and squares, Dale et al. proposed an idealized distribution of support fibers along the edges and across each face of the structure. This idealized network is shown in Figure 4.1(b). Dale et al. then derived a

pressure dependent relationship for the nodal forces based on regular polygon geometry assumptions and applied a stress-strain relationship for each fiber element based on reported empirical relationships by Carton et al. [36] Volumetric strain was then measured as a function of transmural pressure using parameter values reported for saline-filled cat lung parenchyma. Results from the model proved promising enough to spark interest in the development of tetrakaidecahedron-based finite element models of lung parenchyma.

The primary weakness of Dale’s model was the failure to include surface tension effects into the dynamics of the alveolus. In 1986 Kowe and Schroter [32] improved upon Dale’s model by applying several surface tension formulas to the mechanics of the tetrakaidecahedron alveolus. These formulas calculate surface tension based on relative surface area, and a set of constants derived from curve fits to experimental data. In order to account for the hysteresis induced by surface tension, Kowe and Schroter used three different surface tensions formulas: one for inflation and two for deflation. The resultant volume-pressure curves agreed qualitatively with data for whole lungs, but since the model incorporated only a single alveolus, no quantitative comparison was performed.

In 1988, Fung [54] extended the single alveolus model used by Dale et al. to investigate the properties of an alveolar duct. In this model, Fung proposed that a unit of alveolar duct can be modeled by a single pin-jointed, faceless, tetrakaidecahedron, surrounded by 14 identical tetrakaidecahedra. Each surrounding tetrakaidecahedron represents an alveolus that is ventilated to the

central faceless tetrakaidecahedra. Since the geometry is tessellating, units of alveolar duct can be connected to each other by simply removing more faces from the adjacent polyhedrons. Figure 4.2 shows a vertical array of two alveolar duct units. Fung focused only on the morphometric accuracy of this geometrical approximation. He concluded that the proposed geometry may help unravel the complex relationship between alveolar deformation, surface tension, and the curvature of support fibers of the alveolar duct.

Since Fung's proposed model of an alveolar duct, two lung models have been developed by Denny and Schroter from the Imperial College of Science, Technology and Medicine in London. They have published a series of papers [4-7,58] that expands on the tetrakaidecahedron finite element model originally proposed by Dale et al. [3]. The seminal paper, published in 1995, combined the work of Dale et al. [3] and Kowe et al. [32] into Fung's proposed alveolar duct geometry [Figure 4.2(b)]. The goal of the paper was to develop an adaptable model of a lung tissue duct that accounted for changes in collagen and elastin fiber distribution based on experimental observations of actual lungs (or the lungs of a given species). Like Dale et al. [3], Kowe et al. [32], and Fung [54], Denny and Schroter [4] believed the tetrakaidecahedron is the most ideal polyhedra for lung modeling purposes. They proposed a vertical tower of 36 tetrakaidecahedrons as a model for an alveolar duct. The structure is composed of 4 central, faceless tetrakaidecahedrons surrounded axially by semi-closed tetrakaidecahedrons (only the face connecting to the central tetrakaidecahedron is removed). The dynamic support structure has two com-

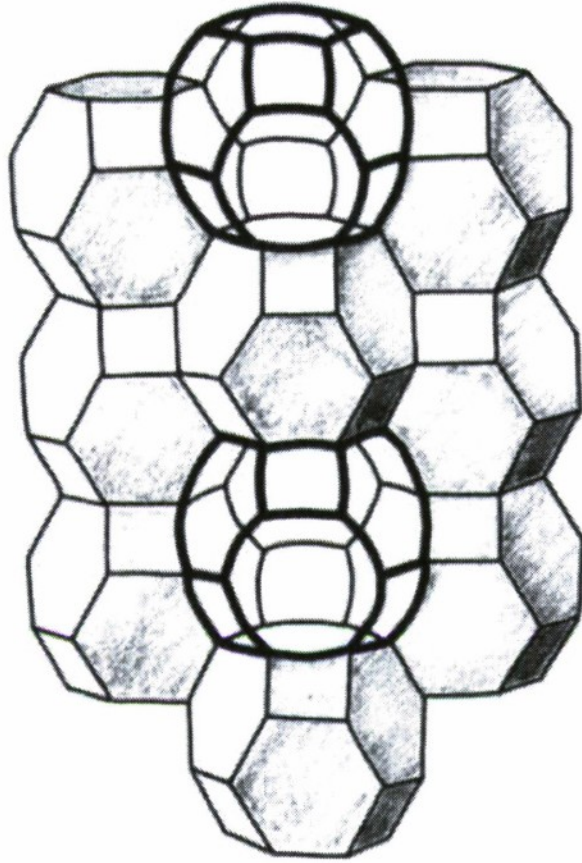


Figure 4.2: An illustration, taken from Fung, [54] of the alveolar duct model consisting of 2 central faceless tetrakaidecahedra surrounded completely by adjacent tetrakaidecahedra. In this illustration the front half of the duct has been removed to show the central faceless polyhedrons highlighted in bold.

ponents: pin-jointed bar elements which compose all edges of the geometry and lie across each face in an idealized structure [Figure 4.1(b)], and surface tension forces applied to all of the faces which have not been removed from the model. Each pin-jointed bar element was assigned two constitutive equations designed to model the participation of elastin and collagen bundles independently. Elastin bundles were assigned a linear stress-strain relationship with a Young's modulus of 6×10^5 Pa. Collagen bundles were given a nonlinear stress-strain relationship taken from Kowe and Schroter's work [32] in 1986. The relationship used in the model is given mathematically by [4]

$$\sigma = 10^5 \left(e^{a_1 \epsilon_A} + \epsilon_A^2 e^{(a_2 + \epsilon_A)^m} - 1 \right), \quad (4.1)$$

where σ is stress in Pa, ϵ_A is the sum of the increments of strain, and a_1 , a_2 , and m are constants. While some experimental data are known for collagen at its extreme values (low and high strain), Denny and Schroter [4] admit that the choice of constants in Equation (4.1) is "fairly arbitrary". The second component of the support structure, surface tension, was modeled using a set of equations taken from Kowe and Schroter [32]. For surface forces applied during inflation, the relationship is given by

$$\gamma = \gamma_{\max} (1 - d_1 e^{-d_2 A/A_0}), \quad (4.2)$$

where γ is the current surface tension, γ_{\max} is its maximum value, A is the current surface area, A_0 is the initial surface area, and d_1 and d_2 are constants. During deflation, the surface force relationship is given by

$$\gamma = c_1 \left(1 - c_2 e^{-c_3 A/A_0} \right)^n + c_4, \quad (4.3)$$

where c_1 , c_2 , c_3 , and c_4 are constants and n is an integer ≥ 12 . Constants for both surface area relationships as well as those used in the collagen bundle constitutive equation can be obtained from the caption of Figure 4 in Denny and Schroter's paper [4]. The reader should note that in Equation (4.3), the constant 'e' in the reference has been changed to 'c' in this text in order to avoid confusion with Euler's number. After defining the geometry and support structure of the model, Denny and Schroter [4] applied a nonlinear, large-displacement finite element method to the alveolar duct model and compared it to results obtained for a single closed alveolus (Kowe and Schroter's model [32]). In particular, volume vs. pressure curves are presented for the alveolar duct model, a single alveolus model, and experimental measurements of the entire lung for comparison. Denny and Schroter [4] also generated volume vs. pressure curves for different distributions of elastin and collagen in the model. Both comparisons agreed qualitatively with experimental observations.

In 1997, Denny and Schroter [5] published an extension of their duct model which focused on characterizing the changes induced in the computed static VP behavior from variation of alveolar dimensions and fiber volume densities. Three primary conclusions are drawn from the second publication: (1) surface tension plays a more important role for lungs with smaller alveoli, or lower fiber density; (2) the distribution of connective tissue between alveolar mouths and alveolar septa affects the anisotropic expansion of alveolar ducts; (3) variation of fiber density within the tissue affects the distensibility of the tissue. These conclusions help explain the morphometric variation between

mammalian lungs from different species based on their size. It should be noted that a third paper utilizing the same duct model was published by Denny and Schroter [6] in 2000. However, this paper focused on the dynamic viscoelastic response of the model as opposed to the static volume vs. pressure response. Therefore the authors utilized frequency dependent relaxation functions in conjunction with the stress-strain curves used in previous models to define constitutive equations for elastin and collagen bundles. Another advancement in this model was the use of a time-dependent surface force equation proposed and tested by Otis et al. [59]

The second model, introduced by Denny and Schroter in 1996, [58] aimed to expand the applicability of the close-packed tetrakaidecahedron shape to model an entire ventilatory unit, or acinus. By ventilatory unit they mean a final respiratory bronchiole and the subsequent alveolar ducts and alveolar sacs ventilated through the same bronchiole. Denny and Schroter proposed a cuboidal block of tetrakaidecahedrons as the ideal model of a pulmonary acinus. Though a cube may seem a crude approximation of the complex branching structure of acinus, morphometric data supports the use of discrete separable units to describe individual acinus. [58] The primary concern in this type of geometrical approximation is the validity of the branching pattern and arrangement of alveolar sacs and ducts within the cube. To address this concern, Denny and Schroter use a simulated annealing technique. The process is similar to alveolar duct models in that each duct or bronchiole is formed by removing common faces with the connecting duct or alveoli. However face-removal

is governed by a set of rules which define “permissible configurations”. [58] The paper presented a set of rules designed to replicate morphological measurements for a rat ventilatory unit, as presented most completely by Mercer and Crapo. [60] A set of ventilatory unit models were generated and several averaged features were compared with morphological measurements. Given the simplifications within the model, including the assumption that all ducts, bronchioles and alveoli must have the same dimensions, reasonable agreement with morphometric data was realized.

In 2006, Denny and Schroter [7] published a second paper using a cuboidal block of tetrakaidecahedrons as a model of lung parenchyma. However, instead of investigating the pulmonary acinus, Denny and Schroter modeled the non-uniform distortion of general lung parenchyma. The objective of the model was to determine the variation of anisotropic continuum coefficients with the degree of non-uniform distortion. In this scenario, the presence of ducts was argued as superfluous by the authors, and the model contained only complete tetrakaidecahedrons (no faces removed). In the model, Denny and Schroter utilized the same pin-jointed structure as in previous models but substituted the updated constitutive equations for elastin, collagen and surface forces from their dynamic duct model. [6] As in all of their previous models, they used a finite element method with an incremental non-uniform loading procedure to test the model. However, instead of generating volume vs. pressure curves for comparison, they computed familiar continuum coefficients (Poisson’s ratio and shear modulus) of the cuboidal block. Conclusions

from the model indicated that linear theory cannot properly predict stresses and strains in the presence of non-uniform distortion.

This chapter has provided a review of modeling approaches and application in lung modeling literature from the earliest concepts of Neergaard to the complex finite element models of Denny and Schroter. Several of the techniques, modeling equations, and conclusions developed in the models above are important for the development of a two-dimensional lung model in the next chapter.

Chapter 5

Model Assumptions

The last three chapters have presented a review of the biology, mechanics, and techniques involved in lung modeling. The goal of this chapter is twofold: to provide the motivation for a two-dimensional lung tissue model and to develop the assumptions to be incorporated into a numerical model (presented in Chap. 6). The discussion follows a development similar to Fung's [43] proposed methodology wherein the purpose and objective of the model is identified, the alveolar geometry is defined, and the material properties are assigned to the elastic components. Section 5.1 presents a general scenario envisioned by the author which motivates a number of basic assumptions about the model's purpose and excitation parameters. Section 5.2 discusses a number of potential damage mechanisms within the lung that may be due to high-intensity acoustic excitation near resonance and eliminates several of the more common failure modes from the potential causes of damage. Section 5.3 identifies the geometry of a single cell of the model and derives the elastic characteristics of a continuous medium of cellular units. Section 5.4 discusses the chosen constitutive equations assigned to each elastic component in the numerical model. Lastly, Section 5.5 describes the structural arrangement of cells used to model regions of interest in the lung and the restrictions applied

at the edges used to approximate *in vivo* response.

5.1 Scenario

Due to the complex nature of lung modeling, an objective must be clear prior to theoretical derivation in order to generate valid assumptions. A carefully chosen scenario can often illustrate the objective of the model and help generate some basic assumptions. The objective of the author's model is to investigate the following scenario: *A diver in the water submerges and begins swimming toward a restricted area. Once the diver enters the restricted region, a low-frequency tone is emitted into the water. The tone induces discomfort which alerts the diver of danger. If the diver continues to trespass, the tone increases in amplitude until the diver feels compelled to surface or turn around without experiencing fatal injury.* The objective of the author's research group at the University of Texas at Austin is to determine the damage threshold for a low-frequency, waterborne, acoustic signal below which injury is avoided.

If the objective of the tone is to cause discomfort, the frequency of the tone should be chosen to exploit the most sensitive part of the body to underwater vibration. In the literature, the lung is often cited as the most sensitive organ to damage or discomfort from low-frequency waterborne sound, and therefore a range of source frequencies corresponding to lung resonance at appropriate depths is used. According to measurements made by Martin et al. [61], the resonance frequency of the lung varies from approximately 40 Hz at the water surface to 73 Hz at a depth of 36 m. Unsurprisingly, this depth

dependence appears to correlate with the equation for the natural frequency of a bubble in an incompressible liquid, given by [62]

$$f_0 = \frac{1}{2\pi R_0} \sqrt{\frac{3\gamma P_g}{\rho_{\text{eff}}}}, \quad (5.1)$$

where P_g is the gas pressure in the bubble, γ the gas constant, R_0 the equilibrium bubble radius, and ρ_{eff} the effective density of the mass loading. A revealing feature of this frequency range is its wavelength compared to the size of the lung. At 40 Hz, the wavelength in seawater is approximately 37 m, while at 100 Hz, the wavelength is 15 m. A conservative estimate of the human respiratory tract length is 0.5 m. Since the lung is so small compared to the wavelength of the source, the pressure gradient across the length of the lung is also small. So small, in fact, that the pressure will tend to drive the lung in a pulsation (monopole) mode.

For excitation near resonance the degree of discomfort will be correlated directly with the amplitude of the signal. Obviously there exists a threshold at which discomfort begins, and at high amplitude, two limits are of interest. One limit is imposed by nature: the maximum acoustic pressure that can be radiated continuously underwater, which is known as the cavitation threshold. This threshold is determined by a variety of factors that include hydrostatic pressure and vapor pressure. A conservative approximation of the cavitation threshold is given by the peak acoustic pressure amplitude that causes the total pressure in the liquid to drop below vapor pressure and thus precipitate bubble growth. A conservative estimate of vapor pressure in liquid is given by

the hydrostatic pressure, therefore the cavitation amplitude, p_{cav} depends on depth and is given by

$$p_{\text{cav}} = P_0 + \rho gh, \quad (5.2)$$

where P_0 is atmospheric pressure at the water surface (at which 1 atm is taken to be 100 kPa), ρ is the density of the water, g the acceleration of gravity, and h the depth below the surface. At a depth of 10 m ($h = 10$), cavitation pressure, p_{cav} , is estimated to be 2 atm; at 30 m, p_{cav} is 4 atm. These values correspond to a sound pressure level of 223 dB and 229 dB (re 1 μPa), respectively. Therefore a conservative assumption of the maximum achievable sound pressure level of 230 dB is used.

The second upper threshold of interest is the sound pressure level at which lethal injury is incurred by the diver. Currently, there is little published information about the effect of high-intensity low-frequency underwater sound on divers. Pestorius [63] reported the effects of low-frequency sound on divers; however the research was related to specific low-frequency sonar technology and considered frequencies between 160 to 320 Hz and sound pressure levels not exceeding 160 dB. Within this parameter range, no adverse physiological effects were observed. More recently, Cudahy et al. [64] reviewed predictions that support a lung tissue damage threshold somewhere between 180 and 190 dB based on experimental studies of submerged mice and rats exposed to low-frequency sound near lung resonance. The report was generated to ensure that low-frequency sonar is safe for human divers. Since the thresholds identified in the paper are significantly higher than the anticipated diver exposure lev-

els from the low-frequency sonar, no further investigations into human lung response were performed. However, in order to develop an acoustic threat-neutralization technology, a more strict analysis of the human response to lung-resonance excitation is required. Given the difficulties associated with experimentation in this subject, each potential damage mechanism from excitation should be examined theoretically to determine the lowest threshold for damage to human lungs.

The assumptions and development discussed in this section have demonstrated the need for a lung model which can simulate damage mechanisms associated with a lung excited near resonance. The next section presents several potential resonant-mode damage mechanisms.

5.2 Damage Mechanisms

In general, lung tissue damage can manifest itself multiple ways: the alveolar spaces can collapse (atelectasis), air can be forced into the bloodstream (arterial embolism), pulmonary fluid can fill the alveolar spaces (pulmonary edema), and blood vessels can rupture and fill the alveolar space with blood (hemorrhaging). Each failure is associated with different mechanical factors and subsequently different excitation thresholds. This section reviews the potential for each type of failure to occur due to exposure to high-intensity resonant excitation with the intention of identifying the most likely cause of lung damage.

In the literature, atelectasis occurs primarily in two instances: when

air seeps into the pleural space, known as pneumothorax; and when the airways forcefully collapse and reopen at low lung volumes, which is known as atelectrauma. Pneumothorax occurs either spontaneously in weakened lung tissue or as a result of trauma. Traumatically induced pneumothorax occurs from two types of injury, a puncture to the chest wall, allowing air to enter the pleural space directly from the atmosphere, or extreme blunt-force trauma which induces a compression wave that forces air from the parenchyma into the pleural space. [65] In the case of a diver exposed to waterborne sound, the compression wave induced at the boundary of the air-filled lung would have to be large enough to rupture pleural-connective alveoli. Since the pressure fluctuations around the lung are uniform, the magnitude of the compression wave induced in the lung is significantly lower than in cases of blunt-force trauma where a compression wave is induced on one side of the lung and propagates to the opposite side of the lung, therefore hemorrhaging and edema should pose a greater threat at a much lower sound pressure level than pneumothorax. Pneumothorax is not unlikely cause of lung damage due to exposure to high-intensity waterborne sound.

The second instance of atelectasis in the lung is associated with atelectrauma and appears extensively in the literature on ventilator-induced lung injury. In modern medicine, the most common method of artificial ventilation is known as intermittent positive pressure ventilation (IPPV). In this technique, a tube is inserted into the throat and positive air pressure is used to force air into the lung. When the lung reaches a desirable volume the pressure

is released, allowing the natural recoil of the lung and chest cavity to drive exhalation. The most recent ventilation techniques incorporate very simple improvements on the IPPV procedure, namely the positive end expiratory pressure (PEEP) technique, which applies positive pressure over the entire range of the breathing cycle. It is well known (see Chapter 3) that a portion of the hysteresis demonstrated in the volume-pressure curve of mammalian lungs during a breathing cycle is attributed to the closing of distal airways during expiration and the subsequent reopening of airways upon inspiration. Researchers in artificial ventilation discovered that damage appears in lungs that are ventilated at low lung volumes. The damage typically consists of swelling in the parenchyma and the presence of lung fluid or blood in the air space. The damage is believed to be caused by large shear forces induced by the relatively high reopening pressure of collapsed distal airways. At a particular strain threshold, the pores in the interstitial tissue of the parenchyma become distorted enough to force liquid into the air space. The collection of fluid in the air space is known as edema. At an even larger strain threshold, blood vessels may rupture, leading to hemorrhaging in the lung, which was common in IPPV. Positive end expiratory pressure ventilators operate at a minimum pressure above atmospheric to prevent this type of damage. [66] In the case of a diver exposed to intense underwater sound at frequencies near lung resonance, atelectrauma may occur at low lung volumes. For a typical human at total lung capacity, transmural pressure is approximately 30 cmH₂O. [29] The magnitude of the pressure amplitude for a 180 dB re (1 μ Pa) signal in

seawater is approximately 15 cmH₂O. Therefore the magnitude of the pressure fluctuation experienced by the lung during a single cycle of a 180 dB tone underwater is half of the maximum transmural pressure experienced at TLC. The frequency of exposure also reveals an interesting feature. If a human typically breathes between 8 and 12 times per minute, [67] the frequency is less than 0.5 Hz. A diver at the surface has a lung resonance frequency around 40 Hz. [61] Therefore during a single breath cycle, a diver exposed to a 40 Hz tone will experience more than 80 complete acoustic pressure oscillations. This may seem extreme; however, the one factor neglected in this analysis is the magnitude of the strain induced on the tissue from such an excitation. If an assumption is made that the mass of air in the lungs during a single acoustic cycle remains the same, the corresponding volume change will be related to the magnitude of the induced pressure field. For a relative estimate of the strain, the displacement amplitude of a bubble wall at resonance, derived from a simple linearization of the Rayleigh-Plesset equation for bubble pulsations in an acoustic pressure field, is given by

$$\xi_{\max} = \frac{QR_0p_0}{3\gamma P_g}, \quad (5.3)$$

where Q is the quality factor, P_g is the gas pressure, R_0 is the equivalent radius for a sphere with a volume equal to that of a lung, and p_0 is the acoustic pressure amplitude. Martin et al. [61] have reported that Q is in the range of 2 to 3 for human lungs. For a sound pressure level of 180 dB ($p_0 = 15$ cmH₂O) at the surface ($P_g = 1$ atm), with $Q = 3$, and with lung volume taken to be 3 liters (such that $R_0 = 0.09$ m for an equivalent spherical cavity),

Equation (5.3) yields $\xi_{\max} \approx 1$ mm, or approximately 1% strain in the lung tissue. At 200 dB, this displacement increases to approximately 3 mm, or 3% strain. For comparison to typical operating parameters, a deep breath taken by an average male can increase lung volume from 3 to 6 liters, for which $\xi_{\max} = 11$ mm and the strain is 26%. Therefore the strain induced by intense underwater sound does not cause massive fluctuation of volume and direct strain damage. However, around the inspiratory bend in the VP curve (where alveolar recruitment occurs) and around the point of decruitment upon exhalation, rapid changes induced by intense waterborne sound may provoke the kind of trauma observed in the ventilator-induced condition discussed above. The complexity of analysis for this type of damage lies beyond the scope of this work.

A second potential mechanical failure associated with intense underwater sound exposure is air embolism. This phenomenon is primarily associated with divers as it is an acute manifestation of over-pressurization of the lung. Divers face a number of pressure concerns when descending and ascending in the water column. As depth increases, pressure increases linearly due to the increased hydrostatic load of the water column. From the adiabatic gas law, volume is going to vary with pressure according to

$$\frac{V_1}{V_0} = \left(\frac{P_0}{P_1} \right)^{\frac{1}{\gamma}}, \quad (5.4)$$

where γ is the ratio of specific heats, V_0 and P_0 are the initial volume and pressure, respectively, and V_1 and P_1 are the final volume and pressure. Schaeffer et al. [68] characterized air embolism from over expansion through canine

experimentation. The group reported a minimum threshold transpulmonary pressure difference for embolism of 81–95 cmH₂O (8–9.5 kPa). When a diver is exposed to acoustic pressure fluctuations, the only pressure differential experienced by the lung is the elastic recoil from the relative volumetric expansion/contraction of air compared to the incompressible fluids of the arteries and pleura. Therefore the likeliness of air embolism is small; however, for argument sake, if one assumes that the induced elastic pressure, and therefore transpulmonary pressure, is equal to the negative peak acoustic pressure, then a sound pressure level of 198 dB would be required to meet the minimum transpulmonary pressure threshold of 81 cmH₂O. To make an estimate of the volumetric change induced in the lung from a signal of 198 dB, a formula for volumetric strain can be derived directly from Equation (5.4) and is given by

$$\frac{\delta V}{V_0} = V_{\text{strain}} = \left(\frac{P_0}{P_1} \right)^{\frac{1}{\gamma}} - 1, \quad (5.5)$$

where $\delta V = V_1 - V_0$ is the relative volumetric strain induced by the pressure variation from P_0 to P_1 . If P_0 is atmospheric pressure and P_1 is taken to be -81 cmH₂O (8 kPa), with $\gamma = 1.4$, then $\frac{\delta V}{V_0} \approx 6\%$ of the original lung volume. This strain, despite being small, is the most conservative estimate of volumetric strain for a 198 dB sound source in water which can be calculated. As depth increases from the surface, the strain becomes even smaller as the ambient pressure rises. Even at the surface, the calculated strain is still an overestimate due to the highly resistive nature of lung parenchyma at high lung volumes where embolism might be possible. Therefore, air embolism is ruled

out as a primary failure mode associated with intense waterborne acoustic excitation near lung resonance.

The remaining failure modes, edema and hemorrhage, have been mentioned as potential damage mechanisms related to atelectasis, and, research into biophysical effects of intense underwater sound exposure cites hemorrhaging (non-atelectic) from the acoustic deformation of the tissue as the most likely manifestation of damage. [15, 63] Edema is included in this discussion since the processes are predictably similar. Fung, [54] in a paper discussing damage thresholds for impact loading of the lungs, proposed that extreme tensile strain induced in alveolar walls can cause the epithelium, cells which compose the surface of the alveolar wall, and endothelium, cells which separate the interstitium from the capillaries, to become permeable to solutes in the interstitium or capillaries. This permeability is the result of elongation of porous parts of the membrane, like cell-junctions, or through physical rupture of the squamous epithelial or endothelial cells. Upon sufficient elongation, solutes or even blood cells may diffuse through the opening and into the alveolar air space. Another potential is that the capillary walls may rupture while the epithelial cells remain intact, leading to blood accumulation in the interstitial space and subsequent swelling. Instances of swelling in the alveolar septa and solute accumulation in the air space are known collectively as pulmonary edema. If blood cells are introduced, the condition is known as pulmonary hemorrhage. The separate degree of deformation required to produce edema and hemorrhage imply that there are two sound pressure level thresholds at

which divers exposed to waterborne sound will experience pulmonary edema and pulmonary hemorrhage, respectively. An analysis of the support structure provides some further information about the severity of the damage, and the potential for fatality from divers exposed to sounds at these thresholds.

As mentioned in the discussion of pulmonary embolism, the primary effect of acoustic excitation of submerged air-filled cavities is the volume distortion of the air induced by the acoustic pressure. For a lung near total lung capacity, the tissue must compensate entirely for the acoustic pressure-induced expansion beyond the natural strain induced from breathing. Within the lung structure, the alveolar septum is the thinnest portion of the parenchyma tissue and therefore experiences the greatest pressure. Maina and West [69] have characterized the blood-gas barrier in the alveolar septum through an analysis of the support structure inherent in the biological design. An interesting feature of the alveolar septum is the polar composition of the membranes separating the air space from the capillaries. One side of the capillary is extremely thin, and composed only of a fine alveolar cell, a capillary endothelial cell, and a small extra cellular matrix in between. This thin side is likely to be the primary cite of gas diffusion in the lung. The opposite side of each septum is much thicker and contains a larger network of extra cellular material, which includes elastin and collagen. The thick side of the septum is where fluid exchange occurs across the pulmonary capillary. In cases of pulmonary edema, the thick side of the septum swells while the thin side remains unchanged. [69] The polar design of the septum may be an evolved defense to edema-related

lung failure since one side of the blood-gas barrier remains thin for efficient gas diffusion despite swelling of the entire septum. Given this feature, hemorrhage, rather than edema, is believed to be the primary damage mechanism that could lead to injury or fatality.

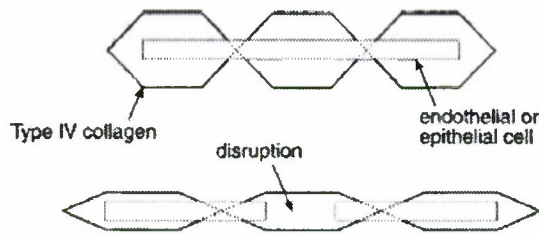


Figure 5.1: Diagram of the collagen support network in response to large deformation in the tissue, taken from Maina and West. [69]

With regard to hemorrhaging, another interesting feature of the septum is the vast network of type IV collagen fibers (dissimilar to the type II collagen fibers discussed in Chap. 2) in the interstitial region of the septum. These stiff fibers act as a safety net to prevent complete rupture of the septum under extreme elongation. Maina and West [69] propose that these fibers may allow the underlying capillaries and endothelial cells to rupture while maintaining the structural composition of the wall. Figure 5.1 illustrates Maina and West's concept of the collagen support during intense elongation of the septal membrane. All told, the fatal potential of hemorrhaging in the lung has yet to be quantified and, in the case of a diver exposed to sound, would be a function of exposure time at or above the hemorrhaging threshold. Therefore

the threshold of hemorrhage is purely the focus of this investigation.

This section has reviewed several potential failure modes of the lung including pneumothorax, atelectic hemorrhage and edema, and acoustically-induced hemorrhage and edema. Of the failure modes discussed, acoustically-induced hemorrhage is the most likely candidate for permanent or fatal damage to the lungs. The author bases this assumption largely on the focus in literature related to bioresponse of humans to high-intensity waterborne sound near lung resonance. [15, 63, 64] However, the remaining failure modes may become increasingly relevant as sonar technology evolve.

5.3 Model Geometry

In Chapter 4 a review was presented of the types of geometries used throughout the literature on lung modeling. This section examines the author's chosen alveolar geometry and the idealized support structure used to model lung parenchyma and the subsequent damage mechanisms, highlighted in Section 5.2, likely responsible for injury from exposure to high-intensity waterborne acoustic excitation near lung resonance. The section begins with the motivation for a two-dimensional model of particular regions of the lung. The discussion then proposes an idealized two-dimensional square tissue geometry highlighting the implications on the isotropy in the lungs.

5.3.1 Motivation for a two-dimensional model

Chapter 4 and Section 5.2 have highlighted the need for a microscopic lung tissue model that is capable of characterizing damage mechanisms within the lung. The model needs to incorporate boundary conditions, provide clear results, and remain expandable and computationally efficient. At first pass, a three-dimensional model meets a number of these criteria, however a two-dimensional simulation is capable of examining a significantly greater number of effective alveolar units for a given computation time. In addition to computational efficiency, similar research performed with a three-dimensional tetrakaidecahedron simulation showed that results are difficult to interpret and error checking can be nearly impossible; [70] while, results from the two-dimensional model are easy to interpret and immediately provide qualitative understanding of the underlying stress concentrations.

5.3.2 Chosen Geometry

Since the introduction of Mead et al.'s model in 1970, [1] regular polygons and polyhedra have become the standard fundamental unit of lung models (see Chap. 4). In two-dimensional space, the choice of regular tessellating polygons is reduced to three possible shapes: the square, the hexagon, and the equilateral triangle. The prevailing wisdom in the literature is to use the shape with the greatest number of sides, like the tetrakaidecahedron in three-dimensions [3, 4, 54] or the hexagon in two-dimensions [1, 53]. In the present work a square geometry is chosen for simplicity. Like the finite element mod-

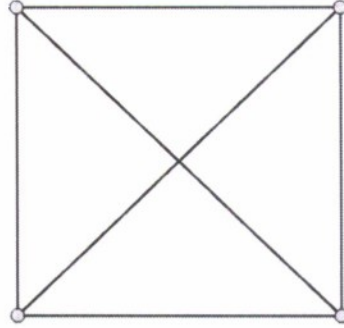


Figure 5.2: An image of the square unit geometry used in the model. Each line represents a pin-jointed bar element. Each circle represents a nodal point mass.

els of Dale et al. [3] the geometry is composed of bar elements assigned with constitutive equations mimicking either single elastic fibers, or an averaged behavior dictated by the scale and application of the model. An image of the model unit geometry is shown in Figure 5.2. The chosen material properties utilized in the two-dimensional lung model are discussed below; however, an analysis of the implications of a square geometry is presented first.

Once geometry is chosen and an idealized network of bar element springs has been contrived, a relationship between the individual constitutive equation for each bar element and the continuous membrane moduli is helpful to understand the characteristics of the chosen geometry. For a lung oscillating in a monopole mode, the primary deformation mode of the tissue will be hydrostatic expansion induced by volumetric expansion of the contained fluid. In this work, hydrostatic expansion is considered the equal deformation of all side lengths of a polygonal structure. In solid mechanics, a set of elastic

moduli can be used to characterize the response of a material under hydrostatic expansion. However, these moduli apply only to continuous media or crystallized solids, whereas lung tissue, and the author's proposed model, is composed of a fibrous support structure. The effective medium moduli must then be obtained by appropriate elasticity analysis. The simplest method is to first derive the generalized stress-strain relationship in terms of the elastic moduli for a square crystal geometry from the general equation of free energy for a crystalline solid, then relate the individual forces of the discretized model to the stresses and strains in the generalized equations. The result is a set of equations for the square crystal elastic moduli as a function of the bar element constitutive equation.

One of the concerns when applying the theory of elasticity is the common assumption of small strains. As mentioned in Chap. 2, lung tissue is highly extensible, capable of maintaining strains of nearly 130% of its equilibrium length. Therefore a small strain assumption applied to lung tissue is inappropriate. In order to utilize the equations from linear elasticity to capture the non-linear nature of the elastic moduli over the full range of hydrostatic expansion, an incremental analysis is utilized. First a prescribed hydrostatic deformation is applied to the square structure. The new deformed state is a reference stress state for the equations of linear elasticity. Infinitesimal deformations are then performed to obtain values for the elastic moduli at the current state of hydrostatic deformation. Then the infinitesimal deformations are removed and the model is again hydrostatically deformed to a new hydro-

static stress state. The equations of linear elasticity are then applied to the new stress state to determine the elastic moduli. This process can be repeated to completely define the elastic moduli of the lung over a large range of deformation. For a single square cell composed of Hookean springs, the process can be performed analytically to determine the equations based on any hydrostatic deformation value; however, a discrete process must be used in numerical models which incorporate more complex geometries or highly nonlinear springs.

General Stress-Strain Relationship

The derivation of a general stress-strain relationship for a square crystal geometry starts from the generalized equation of free energy for a deformed crystal [71]:

$$F = C_{iklm} u_{ik} u_{lm}. \quad (5.6)$$

In two-dimensional space, C is a sixteen-element elastic modulus tensor and u is a small-deformation strain tensor defined by [71]

$$u_{ik} = \frac{1}{2} \left(\frac{\partial u_i}{\partial x_k} + \frac{\partial u_k}{\partial x_i} \right). \quad (5.7)$$

The indices i, j, k, l represent the x and y axes in a standard Cartesian coordinate system. From symmetries in the strain tensor, the elastic modulus tensor exhibits the following symmetries:

$$C_{iklm} = C_{kilm} = C_{ikml} = C_{lmik}. \quad (5.8)$$

In Cartesian space, the symmetries are

$$C_{xyxy} = C_{yxxy} = C_{xyyx} = C_{yxyx}, \quad (5.9)$$

$$C_{xxyy} = C_{yyxx}, \quad (5.10)$$

$$C_{xxxy} = C_{xxyx} = C_{xyxx} = C_{yxxx}, \quad (5.11)$$

$$C_{yyyy} = C_{yyxy} = C_{yxyy} = C_{yyyx}. \quad (5.12)$$

The simplified elastic modulus tensor then contains only six unique elements. If the crystal has additional symmetries, the number of unique elements of C will be less than six. In particular, a square geometry introduces an additional symmetry in Cartesian space,

$$C_{xxxx} = C_{yyyy}, \quad (5.13)$$

and a reduction in terms,

$$C_{xxxy} = C_{yyyx} = 0. \quad (5.14)$$

After simplification, the elastic modulus tensor for a square geometry contains only three unique elements, C_{xxxx} , C_{xxyy} , and C_{xyxy} , which implies that the free energy of a square crystal is determined entirely by three moduli. The next step in the derivation of a set stress-strain equations is the introduction of the stress definition into Equation (5.6). From the basic theory of elasticity

$$\sigma_{ik} = \frac{\partial F}{\partial u_{ik}}. \quad (5.15)$$

Therefore, Equation (5.6) reduces to

$$\sigma_{ik} = C_{iklm}u_{lm}. \quad (5.16)$$

If the square Cartesian symmetries are applied, only three stresses characterize the membrane. The three stress-strain relationships are given by

$$\sigma_{xx} = C_{xxxx}u_{xx} + C_{xxyy}u_{yy}, \quad (5.17)$$

$$\sigma_{yy} = C_{yyyy}u_{yy} + C_{yyxx}u_{xx}, \quad (5.18)$$

$$\sigma_{xy} = 4C_{xyxy}u_{xy}. \quad (5.19)$$

In matrix form, the generalized stress-strain relationship for a square crystal geometry is given by

$$\begin{pmatrix} \sigma_{xx} \\ \sigma_{yy} \\ \sigma_{xy} \end{pmatrix} = \begin{pmatrix} C_{xxxx} & C_{xxyy} & 0 \\ C_{xxyy} & C_{xxxx} & 0 \\ 0 & 0 & 4C_{xyxy} \end{pmatrix} \begin{pmatrix} u_{xx} \\ u_{yy} \\ u_{xy} \end{pmatrix}. \quad (5.20)$$

Discrete Geometry Stress-Strain Relationship

The next step in relating the elastic moduli in Equation (5.20) to the constitutive equations of individual bar elements in the discretized model is the generation of stress-strain relationships for a continuum of discretized cells. Before these relationships can be derived, a connection must be drawn between the strains represented in Equation (5.20) and the strains in a continuous array of discretized square cells. In the generalized equation, the strains u_{xx} , u_{yy} , and u_{xy} represent a longitudinal strain in the x axis direction, a longitudinal strain in the y axis direction and a shear deformation, respectively. Figure (5.3) illustrates a pure strain deformation of each type for a membrane composed of

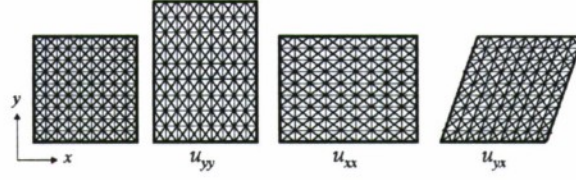


Figure 5.3: A juxtaposition of images showing the strain types represented in Equation (5.20) on a finite array of square cell membranes. From left to right: the array in equilibrium, the array strained longitudinally in the y axis direction, the array strained longitudinally in the x axis direction, and the array in shear deformation.

a finite array of square cells. It should be noted that the longitudinal strains in the figure are not simply generated by applying a force at the ends. Due to the coupling of longitudinal stresses in the microstructure of materials (and in the discrete model), one would generally expect a decrease in the perpendicular dimension from axial loading. So the generation of pure single-axis longitudinal deformation requires that a boundary condition, like sliding rings on a bar, be applied to the perpendicular dimension.

With the relationships between the strains for a continuous array of square cells defined, a similar relationship is sought for the stresses. From solid mechanics, the local stresses induced in a structure represent the resistive forces present in the body when a preferentially-aligned slice is taken through the structure divided by the slice area. In the case of a continuous medium composed of square cells, σ_{xx} would represent sum of forces acting in the x direction on a slice perpendicular to the x axis. The σ_{xx} stress measurement for a piece of material strained in the u_{xx} mode is shown in Figure 5.4. From

the elementary definition of stress

$$\sigma_{ik} = \frac{\overline{F}_{ik}}{A_i}, \quad (5.21)$$

where \overline{F}_{ik} is the sum of the forces in the k direction acting on the i face and A_i is the area of the i side (length in two-dimensional space). For a continuous medium of square cell geometry, the unique forces per length provide the measure of force per cellular unit length. For the σ_{xx} case, the forces obtained from a u_{xx} strain are illustrated in Figure 5.4.

The next step in the derivation is to apply a constitutive equation to the discrete elements in the square cell geometry. In this analytical derivation, the bar elements are assumed to be Hookean strain springs that follow the simple relationship

$$F_{\text{elem}} = k \frac{\delta l}{l_0}, \quad (5.22)$$

where F_{elem} is the resistive force of the element, k is a spring constant with units of force, δl is the elongation of the spring, and l_0 is the equilibrium spring length. In the equilibrium square cell geometry, there are two equilibrium spring lengths, L_0 and L_1 , for the side length and diagonal length, respectively. Figure 5.5 illustrates the geometric definitions of the equilibrium lengths.

Now a hydrostatic deformation can be applied to the square cell to obtain a reference state for the application of the elasticity equations. Upon hydrostatic deformation, a new set of lengths is defined. L'_0 is the length of a side element under hydrostatic deformation. L'_1 is the length of a diagonal

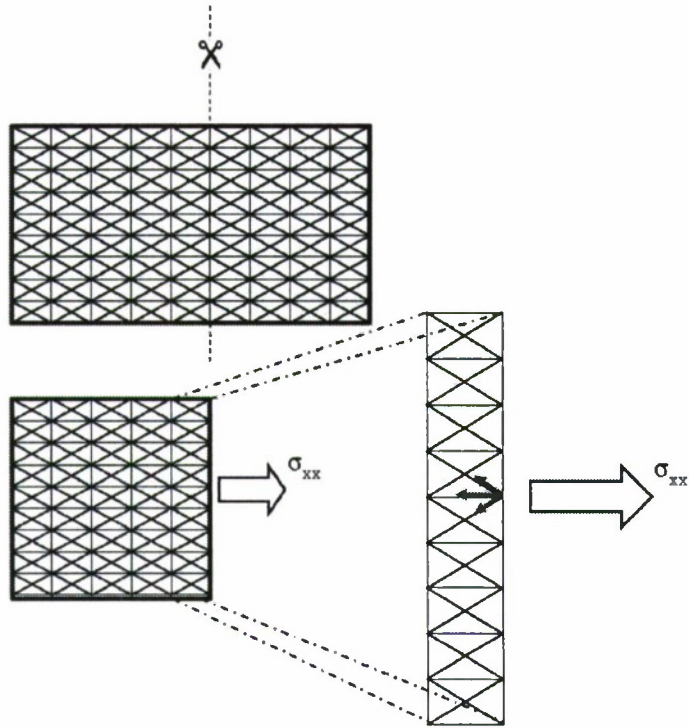


Figure 5.4: The stress measurement for a membrane composed of square cells in pure u_{xx} longitudinal strain. The top image shows the imaginary cut performed to measure σ_{xx} , and the bottom left image shows the remaining section of material along with a stress arrow indicating the stress required to maintain the deformation. The bottom right image is an exploded view of the square cells of the boundary, with red arrows highlighting the unique resistive forces per square cell length.

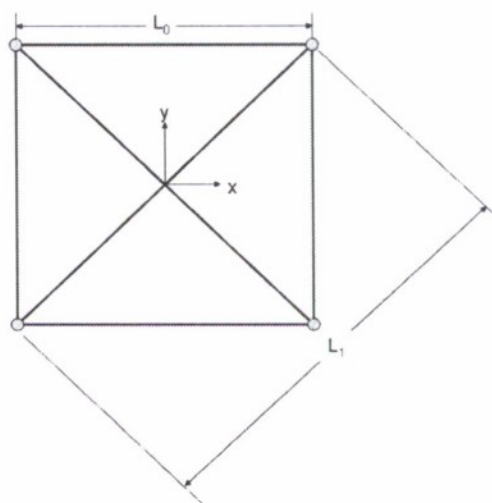


Figure 5.5: An illustration of the idealized square cell geometry with equilibrium length variables defined.

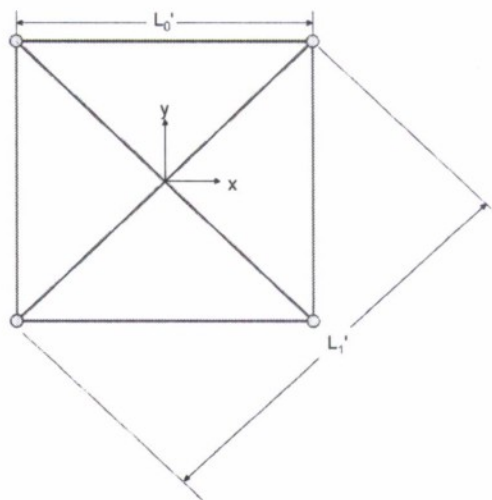


Figure 5.6: An illustration of the hydrostatically deformed square cell geometry with length variables defined. The grey bars represent the equilibrium geometry.

element under the same conditions. Figure 5.6 illustrates the length definitions for a hydrostatically deformed square cell.

Once the cell is hydrostatically deformed, a reference stress state is established. From the discussion of stress definitions for a continuous array of square cells, the calculation of reference stress depends on the type of stress. For each type of stress there is a set of unique forces which must be summed and divided by the hydrostatic side length. Fortunately, upon hydrostatic deformation, the forces are equal in both Cartesian directions, leading to a simple force sum

$$\overline{F}'_{ii} = \frac{k}{L_0}(L'_0 - L_0) + 2\frac{k}{L_1}(L'_1 - L_1)\frac{L'_0}{L'_1}, \quad (5.23)$$

where \overline{F}'_{ii} is the resultant hydrostatic force for either longitudinal direction, composed of three unique bar-element forces per side in a longitudinal deformation. In the case of hydrostatic deformation, there are no shear forces induced in the structure, and therefore the reference hydrostatic shear force is zero. The hydrostatic stress state can be obtained through the stress definition above and is equal to \overline{F}'_{ii}/L'_1 .

An additional set of stress and strain relationships will be required to relate the elastic moduli to the constitutive equations of each bar element. In particular, two analytical deformations will be required to relate all of the stresses and strains in the general equation to forces and elongations in the discretized model. The first deformation is a pure longitudinal strain along the $+x$ axis while fixing the y axis dimension. This deformation sets u_{yy} to zero

in Equation (5.20), leading to two simple relationship for C_{xxxx} and C_{xxyy} :

$$C_{xxxx} = \frac{\sigma_{xx}}{u_{xx}}, \quad (5.24)$$

$$C_{xxyy} = \frac{\sigma_{yy}}{u_{xx}}. \quad (5.25)$$

The second deformation is a shear strain applied to the $+y$ face, labeled as u_{yx} in Figure 5.3. This deformation will allow for the calculation of C_{xyxy} according to

$$C_{xyxy} = \frac{\sigma_{yx}}{4u_{yx}}, \quad (5.26)$$

obtained from Equation (5.20). In general the elongation and shear can be applied to any face, but specific faces are chosen for simplicity. For each of these deformations, additional lengths must be defined to determine analytically the force contribution of each element in the discrete model. Figure 5.7 illustrates the length changes and definitions for an elongation deformation. Here ϵ_l is an infinitesimal elongation length, L_0'' is the total length of an elongated side element of a square under hydrostatic deformation, and L_1'' is the total length of an elongated diagonal element of a square under hydrostatic deformation. Figure 5.8 illustrates the length variable definitions used in calculations of stress and strain due to shear deformation. Here, ϵ_s is an infinitesimal shear stretch length. It should be noted that the y face side lengths (top and bottom faces in Figure 5.8) remain the same before and after deformation, while the x face side lengths, L_{s0}'' , increase with increasing shear. The diagonal elements also vary; one diagonal increases in length upon shear to L_{2+}'' while the other decreases in length upon shear to L_{2-}'' .

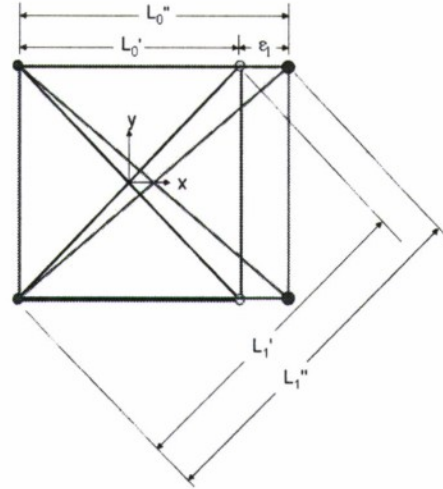


Figure 5.7: An illustration of the length variable definitions for an elongation deformation applied to the hydrostatically expanded square cell geometry.

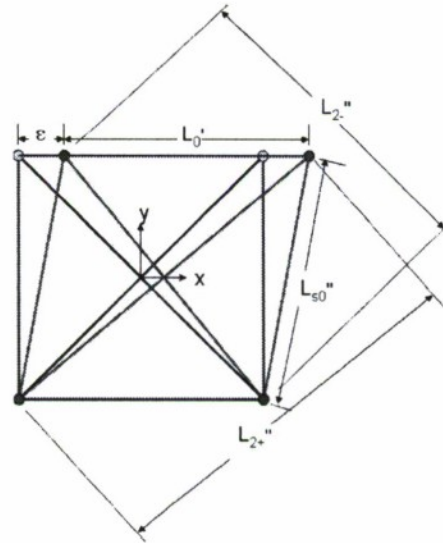


Figure 5.8: An illustration of the length variable definitions for a shear deformation applied to the hydrostatically expanded square cell geometry.

For the lengths defined above, the total force for a given stress state, \overline{F}_{ik}'' , is determined by simply adding the k^{th} axis projections of the forces on the i^{th} face of the structure. In the case of longitudinal strain superimposed on the reference hydrostatically deformed state, the total x and y forces are given by

$$\overline{F}_{xx}'' = \frac{k}{L_0}(L'_0 + \epsilon_l - L_0) + 2\frac{k}{L_1}(L_1'' - L_1)\frac{L'_0 + \epsilon_l}{L_1''}, \quad (5.27)$$

$$\overline{F}_{yy}'' = \frac{k}{L_0}(L'_0 - L_0) + 2\frac{k}{L_1}(L_1'' - L_1)\frac{L'_0}{L_1''}. \quad (5.28)$$

For the shear strain case, the total force is given by

$$\overline{F}_{yx}'' = \frac{k}{L_0}(L_{s0}'' - L_0)\frac{\epsilon_s}{L_{s0}''} + \frac{k}{L_1}(L_{2+}'' - L_1)\frac{L'_0 + \epsilon_s}{L_{2+}''} - \frac{k}{L_1}(L_{2-}'' - L_1)\frac{L'_0 - \epsilon_s}{L_{2-}''}. \quad (5.29)$$

For the discrete model, stresses corresponding to those measured in Equation (5.20) are calculated according to

$$\sigma_{ik} = \frac{\overline{F}_{ik}'' - \overline{F}_{ik}'}{L'_0}. \quad (5.30)$$

In this case, σ_{ik} represents the relative stress induced by infinitesimal deformation of the structure at a given hydrostatic deformation. The corresponding strain for the infinitesimal deformation of the structure at a given hydrostatic deformation state is given by

$$u_{ii} = \frac{\epsilon_l}{L'_0}, \quad (5.31)$$

$$u_{ik} = \frac{\epsilon_s}{2L'_0}, \quad (i \neq k). \quad (5.32)$$

Elastic Moduli Relationships

If the stress and strain values in Equations (5.24–5.26) are replaced with the appropriate stress and strain relationships from Equations (5.30–5.32) then the relationships for the elastic moduli in Equation (5.20) as a function of the bar element forces are realized. However, since the incremental procedure is intended to identify the elastic constants for hydrostatic deformation, the limit of each modulus is taken as ϵ vanishes:

$$C_{xxxx} = \lim_{\epsilon_l \rightarrow 0} \frac{\bar{F}_{xx}'' - \bar{F}_{xx}'}{\epsilon_l}, \quad (5.33)$$

$$C_{xxyy} = \lim_{\epsilon_l \rightarrow 0} \frac{\bar{F}_{yy}'' - \bar{F}_{yy}'}{\epsilon_l}, \quad (5.34)$$

$$C_{xyxy} = \lim_{\epsilon_s \rightarrow 0} \frac{\bar{F}_{yx}'' - \bar{F}_{yx}'}{2\epsilon_s}. \quad (5.35)$$

To obtain an explicit relationship between the elastic moduli and the constitutive equations for bar elements, the total force equations must be substituted into Equations (5.33–5.35). We begin with the force difference in Equation (5.33),

$$\bar{F}_{xx}'' - \bar{F}_{xx}' = \frac{k}{L_0}\epsilon_l + 2\frac{k}{L_1} \left[\frac{(L_1'' - L_1)(L_0' + \epsilon_l)}{L_1''} - \frac{(L_1' - L_1)L_0'}{L_1'} \right]. \quad (5.36)$$

The terms inside the brackets in Equation (5.36) can be expanded and simplified to obtain

$$\bar{F}_{xx}'' - \bar{F}_{xx}' = \frac{k}{L_0}\epsilon_l + 2\frac{k}{L_1} \left[\epsilon_l \left(1 - \frac{L_1}{L_1''} \right) + \frac{L_1 L_0'}{L_1'} \left(1 - \frac{L_1'}{L_1''} \right) \right]. \quad (5.37)$$

Substitution of Equation (5.37) into Equation (5.33) yields

$$C_{xxxx} = \frac{k}{L_0} + \lim_{\epsilon_l \rightarrow 0} 2 \frac{k}{L_1} \left(1 - \frac{L_1}{L_1''} \right) + \lim_{\epsilon_l \rightarrow 0} 2 \frac{k'}{\sqrt{2}\epsilon_l} \left(1 - \frac{L_1'}{L_1''} \right). \quad (5.38)$$

Further examination of the geometry in Figure 5.7 reveals that ϵ_l appears in L_1'' through the relationship

$$L_1'' = \sqrt{(L_0' + \epsilon_l)^2 + L_0'^2}. \quad (5.39)$$

Inspection of Equation (5.38) reveals that the binomial on the left, when the limit is taken, reduces to

$$\lim_{\epsilon_l \rightarrow 0} \left(1 - \frac{L_1}{L_1''} \right) = 1 - \frac{L_1}{\sqrt{2}L_0'} = 1 - \frac{L_1}{L_1'}. \quad (5.40)$$

The binomial on the right requires a little more manipulation. First, a relationship between L_1'' and L_1' is derived:

$$L_1'' = \sqrt{\left(\frac{L_1'}{\sqrt{2}} + \epsilon_l \right)^2 + \left(\frac{L_1'}{\sqrt{2}} \right)^2} = L_1' \sqrt{1 + \left(\frac{2\epsilon_l}{\sqrt{2}L_1'} + \frac{\epsilon_l^2}{L_1'^2} \right)}. \quad (5.41)$$

Substitute Equation (5.41) into the second binomial in the parentheses in Equation (5.38) to obtain the equation

$$1 - \frac{L_1'}{L_1''} = 1 - \left[1 + \left(\frac{2\epsilon_l}{\sqrt{2}L_1'} + \frac{\epsilon_l^2}{L_1'^2} \right) \right]^{-\frac{1}{2}}. \quad (5.42)$$

Since ϵ_l is small compared to L_1' , one can assume the squared term in parentheses in Equation (5.42) is negligible. The remaining binomial in brackets can be simplified using the linear approximation

$$\left(1 + \frac{2\epsilon_l}{\sqrt{2}L_1'} \right)^{-\frac{1}{2}} \approx 1 - \frac{\epsilon_l}{\sqrt{2}L_1'}. \quad (5.43)$$

Equation (5.43) can be substituted into Equation (5.42) to obtain the simplified binomial

$$1 - \frac{L'_1}{L''_1} \approx \frac{\epsilon_l}{\sqrt{2}L'_1}. \quad (5.44)$$

Finally, Equation (5.44) and Equation (5.40) can be substituted into Equation (5.38), with the appropriate limits applied, to obtain the expression

$$C_{xxxx} = \frac{k}{L_0} + 2\frac{k}{L_1} \left(1 - \frac{L_1}{2L'_1}\right). \quad (5.45)$$

Attention is turned now to the force difference in Equation (5.34),

$$\overline{F''}_{yy} - \overline{F}'_{yy} = 2\frac{k}{L_1} \left[(L''_1 - L_1) \frac{L'_0}{L''_1} - (L'_1 - L_1) \frac{L'_0}{L'_1} \right]. \quad (5.46)$$

Equation (5.46) can be simplified in a similar manner as Equation (5.36) to obtain

$$\overline{F''}_{yy} - \overline{F}'_{yy} = 2\frac{kL'_0}{L'_1} \left(1 - \frac{L'_1}{L''_1}\right). \quad (5.47)$$

The approximation from Equation (5.44) can be applied to Equation (5.47) and the result inserted into Equation (5.34):

$$C_{xxyy} = \frac{k}{L'_1}. \quad (5.48)$$

The final modulus to be determined is dependent on the shear force difference:

$$\overline{F''}_{yx} - \overline{F}'_{yx} = \frac{k}{L_0} (L''_{s0} - L_0) \frac{\epsilon_s}{L''_{s0}} + \frac{k}{L_1} (L''_{2+} - L_1) \frac{L'_0 + \epsilon_s}{L''_{2+}} - \frac{k}{L_1} (L''_{2-} - L_1) \frac{L'_0 - \epsilon_s}{L''_{2-}}. \quad (5.49)$$

Equation (5.49) can be reduced to a set of binomial terms like in the previous force difference calculations:

$$\overline{F}_{yx}'' - \overline{F}_{yx}' = \frac{k\epsilon_s}{L_0} \left(1 - \frac{L_0}{L_{s0}''} \right) + 2 \frac{k\epsilon_s}{L_1} + kL_0' \left(\frac{1}{L_{2-}''} - \frac{1}{L_{2+}''} \right) - k\epsilon_s \left(\frac{1}{L_{2-}''} + \frac{1}{L_{2+}''} \right). \quad (5.50)$$

With a new geometry, each term in the binomial is expanded a little differently from the longitudinal case. From Figure 5.8, simple geometry shows

$$L_{s0}'' = \sqrt{L_0'^2 + \epsilon_s^2}, \quad (5.51)$$

$$L_{2+}'' = \sqrt{(L_0' + \epsilon_s)^2 + L_0'^2}, \quad (5.52)$$

$$L_{2-}'' = \sqrt{(L_0' - \epsilon_s)^2 + L_0'^2}. \quad (5.53)$$

As in the longitudinal strain development, each binomial can be reduced independently and reinserted into Equation (5.50). Simplification begins with the first binomial in parentheses in Equation (5.50):

$$1 - \frac{L_0}{L_{s0}''} = 1 - \frac{L_0}{L_0'} \left(1 + \frac{\epsilon_s^2}{L_0'^2} \right)^{-1/2}. \quad (5.54)$$

In the linear approximation, the expression on the right in Equation (5.54) is given by

$$1 - \frac{L_0}{L_{s0}''} \approx 1 - \frac{L_0}{L_0'}. \quad (5.55)$$

The second binomial in the parentheses in Equation (5.50) can be reduced to

$$\frac{1}{L_{2-}''} - \frac{1}{L_{2+}''} = (2L_0'^2 - 2L_0'\epsilon_s + \epsilon_s^2)^{-1/2} - (2L_0'^2 + 2L_0'\epsilon_s + \epsilon_s^2)^{-1/2}. \quad (5.56)$$

Elimination of the small nonlinear terms from the expression on the right in Equation (5.56) simplifies the relationship to

$$\frac{1}{L_{2-}''} - \frac{1}{L_{2+}''} \approx \frac{1}{L_0'} \left[\left(2 - 2\frac{\epsilon_s}{L_0'} \right)^{-1/2} - \left(2 + 2\frac{\epsilon_s}{L_0'} \right)^{-1/2} \right]. \quad (5.57)$$

A linear approximation can be applied to each of the binomials in brackets in Equation (5.57) and the expression reduces to

$$\frac{1}{L_{2-}''} - \frac{1}{L_{2+}''} \approx \frac{\epsilon_s}{L_0' L_1'}. \quad (5.58)$$

The final binomial in Equation (5.50) is the same as the second binomial with a sign change on the second term. The third binomial can be expanded using Equations (5.52, 5.53). Once nonlinear terms are removed, the binomial can be written as

$$\frac{1}{L_{2-}''} + \frac{1}{L_{2+}''} \approx \frac{1}{L_0'} \left[\left(2 - 2 \frac{\epsilon_s}{L_0'} \right)^{-\frac{1}{2}} + \left(2 + 2 \frac{\epsilon_s}{L_0'} \right)^{-\frac{1}{2}} \right]. \quad (5.59)$$

A linear approximation of each binomial in the parentheses in Equation (5.59) reduces the relationship to

$$\frac{1}{L_{2-}''} + \frac{1}{L_{2+}''} \approx 2 \frac{1}{L_1'}. \quad (5.60)$$

Equations (5.55), (5.58), and (5.60) can be inserted into Equation (5.50) and simplified to obtain

$$\overline{F}_{yx}'' - \overline{F}_{yx}' = \frac{k}{L_0} \epsilon_s \left(1 - \frac{L_0}{L_0'} \right) + 2 \frac{k \epsilon_s}{L_1} - \frac{k \epsilon_s}{L_1'}. \quad (5.61)$$

One can substitute Equation (5.61) into Equation (5.35) to obtain

$$C_{xyxy} = \frac{k}{2L_0} \left(1 - \frac{L_0}{L_0'} \right) + \frac{k}{L_1} \left(1 - \frac{L_1}{2L_1'} \right). \quad (5.62)$$

Equations (5.45), (5.48), and (5.62) provide the characteristic elastic moduli for a given set of hydrostatic deformation lengths. A more useful form

of these equations requires the introduction of a hydrostatic strain term, Δ_H , defined by

$$\Delta_H = \frac{\epsilon_H}{L_0}, \quad (5.63)$$

where ϵ_H is the difference $L'_0 - L_0$. The hydrostatic lengths can be redefined in terms of Δ_H through

$$L'_0 = L_0 + \Delta_H L_0, \quad (5.64)$$

$$L'_1 = L_1 + \Delta_H L_1. \quad (5.65)$$

The relationships for each elastic modulus can now be written in terms of a hydrostatic strain deformation:

$$C_{xxxx} = \frac{k}{L_0} + 2\frac{k}{L_1} \left(1 - \frac{1}{2(1 + \Delta_H)}\right), \quad (5.66)$$

$$C_{xxyy} = \frac{k}{L_1} \frac{1}{1 + \Delta_H}, \quad (5.67)$$

$$C_{xyxy} = \frac{k}{2L_0} \left(1 - \frac{1}{1 + \Delta_H}\right) - \frac{k}{L_1} \left(1 - \frac{1}{2(1 + \Delta_H)}\right). \quad (5.68)$$

Figure 5.9 shows a plot of the elastic moduli over a realistic range of hydrostatic deformations of the lung. Though each spring in the model is linear with strain, over a range of hydrostatic deformations the structural geometry introduces geometric nonlinearity. Prior to discussion of the results, it should be mentioned that a numerical analysis was applied to a slightly modified geometry. A smaller square was added to the center of the basic square and attached via diagonals from the corners. Figure 5.10 illustrates the proposed geometry. Initially the goal of the modification was to introduce additional

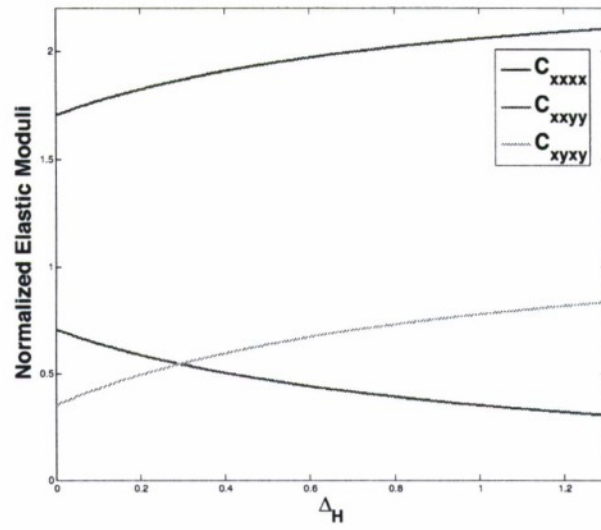


Figure 5.9: A plot of the characteristic elastic moduli for a square cell membrane versus hydrostatic strain for $k = 1$, $L_0 = 1$, $L_1 = \sqrt{2}$, and Δ_H ranging from 0 to 1.3, corresponding to a strain of 130%.

degrees of freedom to the system; however, the hypothesis was proven unfeasible due to a characteristic feature of pin-jointed square structures without complete diagonal supports; they cannot resist shear.

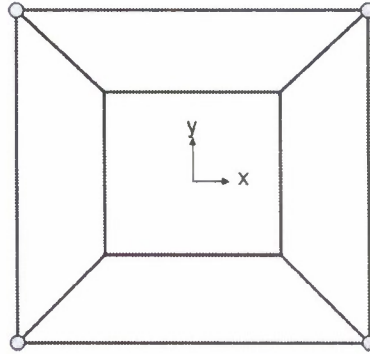


Figure 5.10: A modified square cell geometry generated to increase the flexibility of the square cell model.

A further modification of the geometry included the introduction of diagonal cross-members in the central square. The modification improved the shear resistive characteristics of the structure and introduced an additional degree of freedom, the interior length ratio of the squares. The interior length ratio is defined as the length of the interior square, l_i , divided by the length of the outer square wall, L_0 . Figure 5.11 shows the second iteration of the modified square cell geometry with each length defined. Elastic moduli for the structure were obtained numerically by simulating the incremental hydrostatic deformation procedure, outlined above, on a single cell. Results for three different interior length ratios are plotted along with the analytical solution derived above in Figure 5.12.

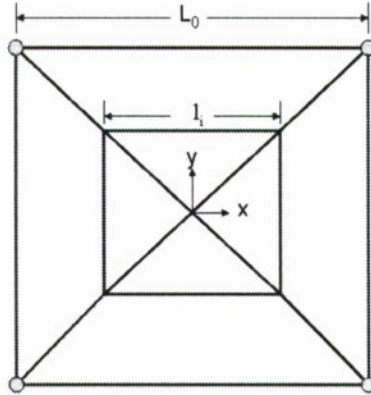


Figure 5.11: The modified square cell geometry with diagonal cross-members added.

Conclusions from Model Geometry

Whether based on a simple square, or a complex square-within-a-square, the behavior of the model exhibits consistent elastic characteristics over a range of hydrostatic deformations. The plots in Figures 5.9 and 5.12 show an increase in longitudinal and shear resistance as the structure reaches large hydrostatic deformations. In the lung, the increase in value of an elastic modulus corresponds primarily to stiffening upon inspiration to total lung capacity. The rapid fluctuations of pressure induced by acoustic excitation would induce expansions on the order of a few percent of the total lung dimension. In a continuous section of parenchyma, the elastic moduli derived in this section provide very little information about the response of the system, since it should only exhibit hydrostatic deformation; however, along a boundary, acoustic excitation may induce non-uniform expansion of tissue. The change in anisotropic elastic response of the tissue may provide clues about the mech-

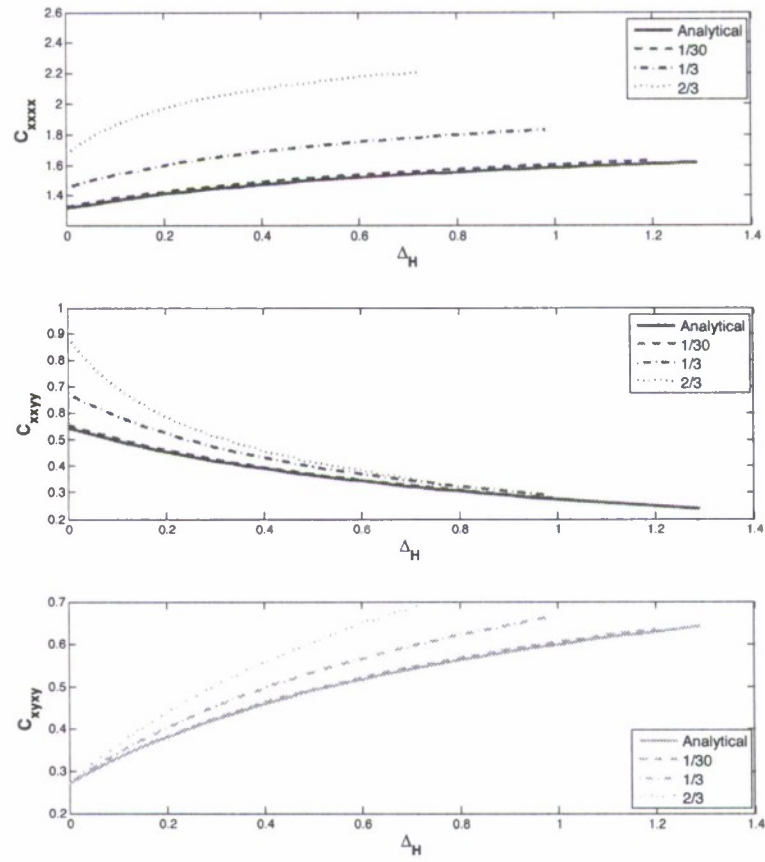


Figure 5.12: Elastic moduli plotted against hydrostatic strain for various interior length ratios in the modified square cell geometry with diagonal cross-members. Here $k = 1/1.3$ N/m, $L_0 = 1$.

anisms responsible lung damage.

5.4 Material Properties

Throughout the literature, a debate exists about the elastic response of lung tissue. Chapter 3 presented several of the qualitative empirical theories about the support structure of the tissue, while Chapter 4 presented several modeling approaches used to replicate mechanical tissue response. The model developed here follows a prevailing theory in modern literature which assumes that a pin-jointed bar element structure is the most appropriate structural support system for a model of lung tissue. In the previous section, an analytical solution for the elastic moduli of a two-dimensional square cell membrane composed of linear strain spring bar element was derived. A more appropriate tissue model follows from the experimental work of Carton et al. [36] and the modeling work of Dale et al. [3],

$$T = -\frac{1}{\alpha} \left(1 - \frac{\epsilon}{\beta} \right), \quad (5.69)$$

where T is tension, α is a constant which depends upon the fiber/bundle cross-sectional area, β is a constant which defines the upper strain limit of the exponential force-strain relationship, and ϵ is the strain of the fiber/bundle. Figure 5.13 illustrates the force strain relationship from Equation (5.69), as well as its linearized form.

The choice for each constant in Equation (5.69) requires a precise definition of the scale of the model. In particular, each bar element must represent

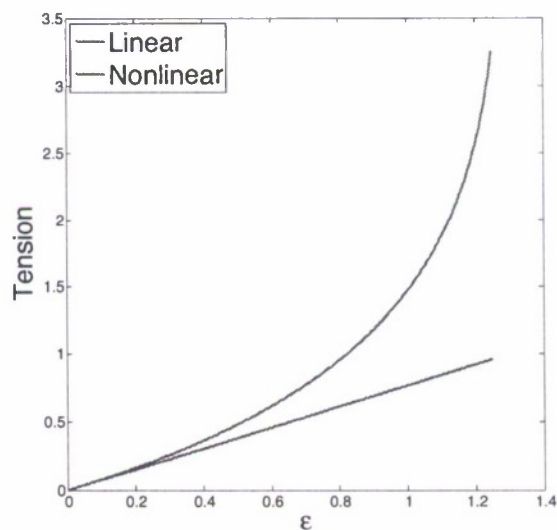


Figure 5.13: A plot of the force-strain relationship in Equation (5.69) with $\alpha = 1$, $\beta = 1.3$. The linear relationship is also plotted for $k = 1/1.3$, the small-strain linear approximation of Equation (5.69).

some finite number of fibers or fiber bundles in order to obtain realistic force estimates from the model. *In vivo*, fibers are arranged in a nearly random array across the alveolar septa, and appear in dense bundles along septal borders and along alveolar mouths and ducts. Therefore, if each square cell of the model is intended to represent a single alveolar septum, the constants chosen in Equation (5.69) should replicate the response of a single fiber, or just a few fibers. However, if each square cell represents some larger aggregate of

alveolar septa, septal borders and ducts, the constants should reflect a more complex relationship derived from the elastic response of larger portions of tissue. Given the difficulty in defining constants based on extrapolated data from the literature, selection of α is neglected in favor of obtaining qualitative, rather than quantitative, results regarding stress concentrations at boundaries. In the model, α has units of force and is set to unity for simplicity.

5.5 Boundary Conditions

In the section on damage mechanisms, two locations in the lung are listed as potential stress concentration regions: the lung tip and the rib-lung interface. Each boundary has unique modeling characteristics. This section examines the assumptions of the model used to characterize the boundaries at the lung tips and rib-lung interface. The discussion first examines the common pleural interface surrounding the lung and the implied boundary conditions. Next, each location of interest is examined independently.

5.5.1 Pleural Lining

Surrounding nearly the entire lung are two thin membranes of tissue known as the parietal and visceral pleura. The two pieces of tissue are actually one continuous sheet of tissue that forms a thin fluid-filled sac around the lung. As discussed in Chap. 2, the function of these tissue layers, and the fluid between them, is two-fold: to provide a nearly frictionless interface for the lungs to move smoothly along the organs, rib cage and diaphragm; and to

maintain a negative relative pressure on the exterior of the lung. This boundary condition resembles a set of rings on a frictionless bar in a modeling sense. The tissue is free to slide along the interface, but no velocity perpendicular to the boundary can be imparted to the tissue. In the model, bar members attached to the pleural edge are allowed to move freely in a line parallel to the interface.

5.5.2 Lung Tips

At the bottom of the thoracic cavity, the lung meets the diaphragm and chest wall. In this model, the lung tip is defined as the region encompassing the intersection between the chest wall and the diaphragm muscle. In two dimensions, the model is a wedge where the two interfaces corresponds to the chest wall and to the diaphragm. Ideally, a model would be able to simulate a variety of angles between the chest wall and diaphragm which likely occur during a normal breathing cycle. However, the use of square cells restricts the angle for a wedge to 45° for a continuous membrane. Therefore the model of the lung tip is a 45° wedge where one wall represents the chest wall interface and the other represents the diaphragm. An image of the wedge structure is shown in Figure 5.14.

Over the duration of an acoustic excitation near lung resonance, very little volume change will occur. Therefore, it is reasonable to assume that the diaphragm and rib will not deflect during excitation. Additionally, the model assumes a static approach where the tissue is stretched to examine

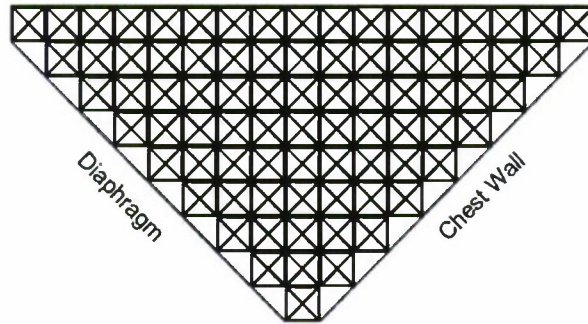


Figure 5.14: An image of a 9 row wedge structure representing the interface between the chest wall, the diaphragm, and lung tissue.

the concentrations of stress for a given geometrical situation. Thus, during a numerical test the vertices of the wedge and the top row of masses are held fixed while the bar elements along the edges are allowed to expand and contract freely along the interface. This condition implies that the entire top row of masses is held fixed in a position until the system reaches equilibrium.

5.5.3 Rib-Lung Interface

Along the exterior of the lung, the rib-lung interface has a greater surface area than any other boundary (the diaphragm or mediastinum). The rib-lung interface model investigates the effects on the lung tissue immediately surrounding a single rib and the tissue which lies between ribs. The lung tissue along the rib is modeled as a rigid structure which cannot deflect in any direction. Between the ribs, the model is given a free boundary condition. Each of these boundary conditions is an exaggeration of actual tissue behavior. For example, in the lung, any tissue along the pleural surface can slide along

the interface, even along the ribs where the model assumes a rigid nature. Additionally, the intercostal muscles, located between the ribs, are an elastic structure that is more rigid than the tissue, but less rigid than the bone. In the model, the elasticity of the intercostals is omitted in favor of investigating the effect of relative strain between the tissue along the rib surface and the tissue between the ribs. An image of the rib-lung interface model is shown in Figure 5.15.

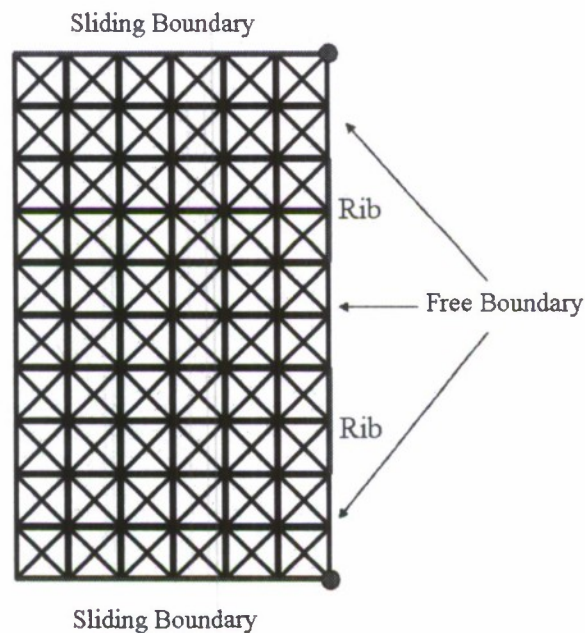


Figure 5.15: An image of a 6×10 rib-lung interface tissue model with 2 ribs denoted by red lines. The blue line represents a sliding boundary condition along the line. The red dots show a rigid point on the structure.

This chapter has developed the assumptions and conditions required to generate a numerical model of two potential damage locations in a lung ex-

posed to high-intensity waterborne sound near resonance. Since the structural geometry and boundary conditions have been defined, the following chapter presents the numerical model and graphical interpretation of results.

Chapter 6

Numerical Model

The previous chapter developed all of the necessary tools to design and implement a two-dimensional lung model based on square unit cell geometry which can be used to investigate potential damage mechanisms in the tissue. The chapter ended with the introduction of two structural arrangements with associated boundary conditions which may be used to investigate damage mechanisms at the rib-lung interface and the lung tips. The present chapter develops the numerical model further, including several graphical interpretations of the resultant data. The discussion begins with the presentation of the model equations in Section 6.1. Section 6.2 explains the process of model excitation incorporated for each of the lung regions under investigation. Finally, Section 6.3 presents several approaches used to obtain both qualitative and quantitative results.

6.1 Discrete Numerical Analysis

Two potential solution methods are considered for the static model of a discretized system of bar elements. The first solution is to minimize the potential energy of the system to determine the 'rest' position of the structure.

This type of solution is computationally efficient, and is a common method for solving large static problems. The second method, used in the current model, is to assign masses at the nodes of the structure and apply Newton's laws to observe the system dynamics. The method of minimizing the potential energy is sufficient for a first draft of the lung model, but the approach based on Newton's laws can also give dynamic solutions. With an infinitesimal mass assigned to each node and a large damping force applied to each bar element, the solution using Newton's laws approach rapidly approaches the solution obtained by using the minimized potential energy approach. This technique is used in the current implementation of the model since rigorous analysis of anatomical data is required to obtain an appropriate representative mass for each node and representative damping coefficient for each bar element in the system.

The numerical model of lung tissue is composed of 2 elements: discrete bar elements defined by a spring-damper constitutive equation, and nodal mass units assigned an arbitrarily small mass value. In the numerical model, the forces which act on each nodal mass are functions of nodal position and velocity. Therefore, each nodal mass is associated with a global position, velocity, and acceleration for each discrete time value in the integration of Newton's law. For any given arrangement of square cells, the velocity and acceleration of the nodal masses is a simple function of the summed contribution of forces

from each of the bar element members attached to the node, and is given by

$$\mathbf{F} = \sum_{i=1}^{N_j} \mathbf{f}_i(\epsilon, v), \quad (6.1)$$

where \mathbf{F} is the total force vector acting on a given nodal mass, N_j is the number of bar elements connected to a given node, v is the relative velocity of the nodal ends of the i th bar element, ϵ is the strain on the i th bar element and $\mathbf{f}_i(\epsilon, v)$ is the bar element constitutive equation defined by

$$\mathbf{f}_i(\epsilon, v) = -\frac{1}{\alpha} \ln \left(1 - \frac{\epsilon}{\beta} \right) - Cv, \quad (6.2)$$

where α and β are the constitutive relation constants defined above, and C is an arbitrarily large damping constant used to reduce the ring-down time of the model. From Newton's second law, the instantaneous acceleration of a nodal mass is simply

$$\mathbf{a} = \frac{1}{m} \sum_{i=1}^n \mathbf{f}_i(\epsilon, v), \quad (6.3)$$

where \mathbf{a} is the acceleration of a given mass node. The velocity of each node follows simply from the integration of acceleration along with the current nodal velocity

$$\mathbf{v}_1 = \mathbf{v}_0 + \int_{t_0}^{t_1} \mathbf{a} dt, \quad (6.4)$$

where \mathbf{v}_1 is the nodal velocity at time t_1 and \mathbf{v}_0 is the nodal velocity at time t_0 . Equations (6.1)–(6.4) are the fundamental equations used in the numerical model of lung tips and the rib-lung interface. All that remains to complete the model is an excitation process explained in the following section.

6.2 Excitation Methods

The numerical model focuses on two potential damage locations in the lung: the lung tips and the rib-lung interface. In each of the locations, we are interested in determining the stress concentrations that result from rapid pressure expansion of the constant volume system (see Section 5.2). This is best accomplished through an incremental strain procedure which approximates *in vivo* response. There are unique problems which arise when trying to create an applicable simulation using two-dimensional square cell geometry. This section analyzes the boundary conditions and excitation processes that are applied to each region of the lung in order to simulate acoustic excitation response.

6.2.1 Lung Tips

For the numerical model of lung tips, the initial configuration is shown in Figure 5.14. In this figure, there are nine rows of square unit cells. The size of the structure is determined by the number of rows used to generate the wedge shape. After the shape is generated, each mass is assigned zero initial velocity and zero initial acceleration. The structure is then excited by imposing a small vertical displacement on the top row of masses. The force on each nodal mass is calculated utilizing the equations in Section 6.1 and integrated using an adaptive Runge-Kutta routine, taken from Numerical Recipes [72], to obtain new locations for the masses. The routine incorporates several boundary conditions. First, the top row of masses is given zero vertical ve-

locity and zero vertical acceleration since the position is governed entirely by the excitation routine. The horizontal velocity and acceleration of each mass in the top row is left free so that the structure can expand without losing its wedge shape. Next, the velocity and acceleration of the two apex masses of the structure are set to zero to impose a rigid point on the structure. This condition simulates the tip of the lung. As air in the lung rapidly expands in response to pressure minima, the tissue surrounding the lung (rib-lung interface and diaphragm) is essentially rigid but the lung tissue remains in contact with the wall, creating a fixed region where the tissue will attempt to separate. Finally, the perpendicular forces on the edges of the wedge are set to zero to create the sliding boundary discussed in Section 5.5. Each of the boundary conditions allows each cell in the structure to expand hydrostatically in area, maintaining the overall wedge shape. The top row continues to be pulled until the overall structure is strained beyond an imposed global strain limit, or until any bar element exceeds the maximum strain length of the elastin-fiber constitutive equation (130%).

The free parameters which define the structure and excitation are the number of rows and the global strain percentage. As the number of rows increases, the number of nodal masses increases and the total computation time increases. In order to capture the behavior of lung tissue along the tips, an appropriate number of square cell rows must be incorporated to eliminate boundary condition effects from excitation along the top row of masses. Currently the largest data set obtained for the lung tip model contains 50 rows

of square cells (2650 masses). Three data files, generated during program execution, contain all of the information necessary to reproduce the wedge at every increment of strain performed during the calculation. A fourth data file records a strain value for the most deformed bar element attached to each mass node after the model is completely deformed. This file can be imported into Matlab or any other data analysis software to quantitatively compare strains around the lung tip structure.

6.2.2 Rib-Lung Interface

The numerical excitation of the rib-lung interface follows a similar pattern to the lung tip presented in the previous section. The initial configuration of the rib-lung interface, shown in Figure 5.15, is composed of a rectangular grid of square cells in equilibrium with a set of masses assigned to be adjacent to the ribs. Masses along the ribs, shown in black in the figure, are set as rigid objects in the structure. The structure is excited by pulling the opposite side of the membrane perpendicular to the ribs. Displacements in the structure are calculated using the same deformation-integration procedure used for the lung tips, but the boundary conditions are handled a little differently. If no further boundary conditions are imposed on the structure, the middle masses compress toward the center of the structure, forming an hourglass shape, while most of the square cells elongate in a direction perpendicular to the structure. This compression, associated with Poisson's ratio in solid mechanics, is unrealistic for a piece of continuous tissue because the boundary condition is no longer

free to deform—the connecting tissue resists the deformation. The phenomenon is overcome by imposing a sliding boundary condition on the free edges of the membrane. These boundary conditions cause the structure to appear as an expanding rectangle, opposed to an hourglass, as deformation is applied.

It is believed that *in vivo* the tissue expands nearly uniformly, appearing as a hydrostatic area expansion in two-dimensions; however, hydrostatic expansion of a two-dimensional model around the ribs is difficult to reproduce since, in contrast to the lung tips, where pulling on the model corresponded directly to volume expansion of the tissue, the rib-lung interface poses significant problems in replicating volume expansion in two-dimensions. By pulling on the membrane in the manner described above, a longitudinal deformation of the square cells occurs and the free edges of the membrane between the ribs pull in toward the inner parts of the lung. This deformation simulates volume compression rather than volume expansion of the lung since the tissue would press outwards between the ribs as the lung expands. However, the location and relative intensity of stress concentration in the compressing rib-lung interface simulation should be nearly equivalent to the expansion of the tissue along the rib-lung interface.

The output from the model is the same as obtained from the lung tips model. Mass locations are recorded for each integration step in the process and a final maximum strain file is written for quantitative strain analysis.

6.3 Graphical Interpretation

Each numerical model described above is augmented with an adaptable three-dimensional graphical output, programmed using the OpenGL API, which initiates immediately following the numerical simulation. The objective of the graphical output is to assist in drawing qualitative conclusions about the stresses and strains in the system and to ensure that programming or numerical errors have not skewed the intended excitation. Two graphical windows illustrate the concentration of stress by superimposing colored bar elements on the initial configuration of the model in one window and on the moving structure in a second window. A two-windowed approach allows the user to simultaneously watch the deformation of the structure to see how strain becomes concentrated in a region and watch stresses develop in the equilibrium structure to identify concentrations in relation to the original configuration.

Each window illustrates the structure by drawing spheres and lines. Each sphere represents a nodal mass and each line represents an elastic bar element. During the course of the simulation, each mass remains a constant color. However, as the structure is deformed, the lines change color as strain is imposed on the bar elements. The coloring scheme spans from yellow to red between an adjustable minimum strain constant and an adjustable maximum

strain constant in a linear progression,

$$R = 1.0, \quad (6.5)$$

$$G = 1.0 - \frac{\epsilon - \epsilon_{\min}}{\epsilon_{\max} - \epsilon_{\min}}, \quad (6.6)$$

$$B = 0.0, \quad (6.7)$$

where R , G , and B are the color indices on a scale of 0 to 1 for red, green, and blue, respectively, ϵ is the strain value of a given bar element, ϵ_{\min} is the minimum strain constant, and ϵ_{\max} is the maximum strain constant. If the linear progression proves inconclusive, an optional exponential relationship has also been developed

$$R = 1.0, \quad (6.8)$$

$$G = 1.0 - \log_{10} \left(1 + C \epsilon_{\min} \frac{\epsilon - \epsilon_{\min}}{\epsilon_{\max} - \epsilon_{\min}} \right), \quad (6.9)$$

$$B = 0.0. \quad (6.10)$$

where C is an adjustable parameter which determines the sensitivity of the graphical system to various ranges of strain.

The second window also illustrates the model structure with spheres and lines. However, as the data from the numerical simulation are read, the mass positions change (along with the bar element colors) according to the simulation data. This window allows the user to visually inspect the dynamics of the model over the complete simulation to ensure the data is physically accurate and that no errors have occurred. In the rib-lung interface simulation these illustrations also provide a visual reference for the degree of strain

imparted on the system and the resultant shape deformation. Since the shape remains the same in the lung tips model, it is difficult to get a feel for the percent strain induced on the structure by simply comparing the static to dynamic windows. Figure 6.1 shows the two window outputs for a rib-lung interface simulation.

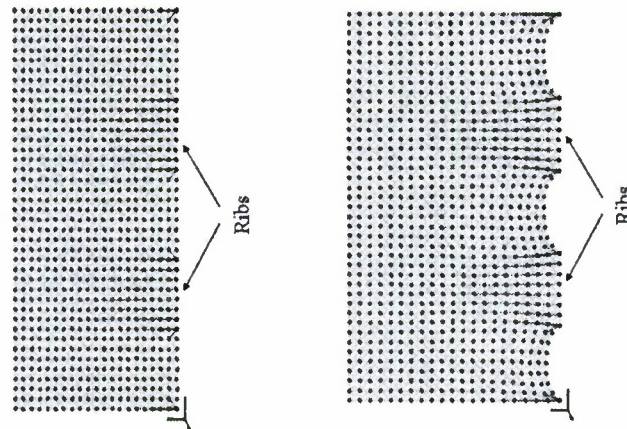


Figure 6.1: Comparison of the two graphical outputs for a rib-lung interface simulation. In the simulation, the structure is strained by 30% of its original width dimension.

Another concern with the graphical output is the difficulty in interpreting results for very large simulations. Particularly when adjacent bar elements experience vastly different percentages of strain, the severity of the strain can potentially be hidden by low strain elements. A solution to this problem is to leave the bar elements hidden until a minimum element strain threshold is met, then draw extremely thick lines to draw attention to the region. Figure 6.2 illustrates use of this technique for modeling the rib-lung interface using an arbitrary minimum strain value of 50% for a global strain value of 130%. In

Figure 6.2, the region of damage along the edges of the ribs are most notable. These results agree well with experimental work by Dalecki et al. [15] which observed hemorrhaging between the ribs on submerged mice exposed to high intensity low-frequency sound. This agreement provides some testament to the validity of the model.

This chapter completes the development of a model for lung tissue damage mechanisms in both the rib-lung interface and lung tips. Though the initial results are qualitative in the graphical interpretation, future adaptations can be applied (finite mass values and modified damping coefficients) to obtain potentially useful realistic quantities for strains experienced at the microscopic level induced by macroscopic hydrostatic expansion of the lung.

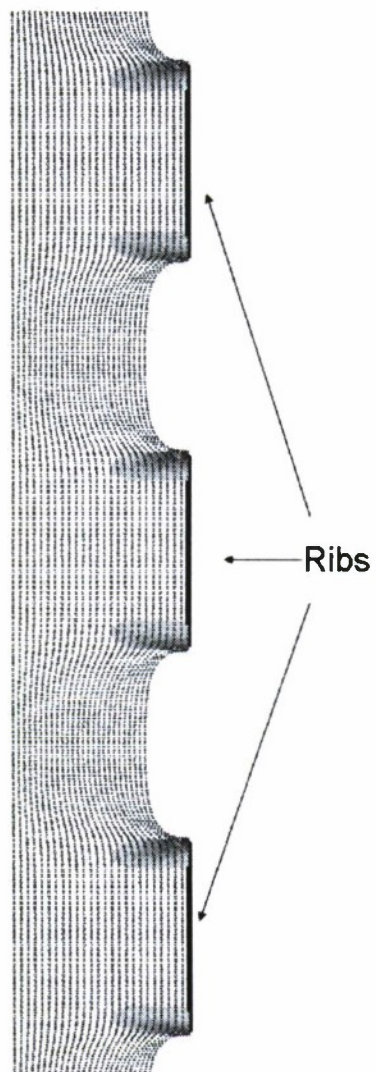


Figure 6.2: Illustration of a strained chest wall using an improved coloring technique to highlight significant stresses and strains in a large simulation.

Chapter 7

Summary and Conclusions

The work presented in Chapters 2-5 has produced a model of microscopic dynamic response of lung parenchyma to excitation which may be used to investigate damage mechanisms in the parenchyma. The objective of the model lies within a broader scope of work to identify specific damage thresholds for submerged human divers exposed to high-intensity low-frequency sounds. The results of this broader investigation can be applied to developing technologies designed to exploit these thresholds for non-lethal diver deterrence in sensitive commercial port areas or naval bases.

The objective of this work was to develop a model of lung tissue damage mechanisms, and several notable accomplishments have been included. The work has bridges to multiple disciplines including biology, solid mechanics, mechanical engineering, and to a lesser extent computer science. This thesis also introduces a unique lung model into the literature that can examine mechanically induced lung damage. Finally, this thesis presents a detailed connection between isotropic elastic constants and an anisotropic line-element model of lung tissue.

This thesis followed a generalized modeling approach that began with

identifying common biological features and morphometry of the lung. Next, historical lung models were examined to get a modern image of the lung and understand what features are absolutely necessary in modeling lung behavior. Given the objective of the model, the third step in the development was to predict which damage mechanisms occur at the lowest effective sound pressure level to provide basic parameter limits for future testing and model development. Finally, a two-dimensional tessellating geometry was chosen for further analysis and model development. These first three steps help establish the true objective and limits of the model, and the remainder of the process was similar to Fung's [43] proposed method as discussed previously in Chapter 4, where a model geometry is selected and corresponding constitutive equations are derived. Finally, boundary conditions are carefully chosen and applied to complete the model.

The development of the model began with a review of current knowledge in the fields of human lung biology, biomechanical lung response, and lung modeling. Specifically, Chapter 2 presented a detailed physiological review of the respiratory system and the components of the lung; Chapter 3 provided an analysis of the mechanical features of mammalian lung tissue and the historical developments that have created the modern image of the lung; and Chapter 4 examined the history of lung modeling, which is the bridge of understanding between morphological data and lung function. Each of these reviews provide a complete picture of both the historical developments within the field and the important features required to develop the current model.

The model developed in the last two chapters is a natural extension of the historical work. In Chapter 5, an analysis of biological failure modes in the lung was presented. The objective of the analysis was to identify the lowest potential damage threshold based on current literature reports and elementary analysis. The literature and basic analysis point to lung hemorrhage as the most likely candidate for damage induced by high-intensity acoustic excitation of the lung. In the last half of Chapter 5, a derivation of constitutive equations was presented for a two-dimensional rectangular crystallographic model of lung tissue. Finally, Chapter 6 presented a numerical method for replicating lung response to hydrostatic acoustic expansion using the two-dimensional model from Chapter 5.

The model developed in this thesis is unique in that it predicts the micromechanical stresses of the tissue along the lung tips and at the rib-lung interface based on macroscopic hydrostatic mechanical excitation. The closest models to this type of analysis come from work on ventilator-induced lung injury; however, excitation from slowly-varying positive trachea pressure may not directly relate to rapid hydrostatic pressure oscillations induced from low-frequency acoustic excitation. Additionally, very little attention has been given to analyzing the potential failure modes associated with hydrostatic acoustic excitation in the literature. The present work includes a unique discussion of the potential failure of the lung and identifies the most likely mode associated with hydrostatic acoustic excitation.

The next step in the life of this model is to perform a complete paramet-

ric study which examines various degrees of macroscopic strain, constitutive equation constants, and element sizes. The conclusions from the study may be combined with macroscopic finite-element models of the lung to obtain a visualized, qualitative feel for the level of microscopic damage induced by various degrees of macroscopic excitation. Several models developed by the research group at Applied Research Laboratories of the University of Texas at Austin may provide the appropriate input strain percentages which would simulate acoustic excitation at a given sound pressure level. This model may provide a vehicle to visualize and understand the micromechanical forces at work. In the long run, one may be able to predict the percentage of lung-tissue damage induced by sound at a particular frequency and sound pressure level. This type of calculation could potentially be applied to psychological studies to predict discomfort levels based on lung damage rates as well.

Several other extensions of this model might include the use of hexagonal structural elements, compound two-dimensional elements (square and hexagons), three-dimensional geometry, or new boundary conditions which characterize the bronchial-alveolar interface. Given the adaptable nature of the current code, implementation of new constitutive relations and two-dimensional geometry is simple, and the graphical representation is well suited for extension to three-dimensional geometry.

Bibliography

- [1] J. Mead, T. Takishima, and D. Leith. Stress distribution in lungs: a model of pulmonary elasticity. *Journal of Applied Physiology*, 28:596–608, 1970.
- [2] J. B. West and F. L. Matthews. Stresses, strains, and surface pressures in the lung caused by its weight. *Journal of Applied Physiology*, 32:332–345, 1972.
- [3] J. P. Dale, F. L. Matthews, and R. C. Schroter. Finite element analysis of lung alveolus. *Journal of Biomechanics*, 13:865–873, 1980.
- [4] E. Denny and R. C. Schroter. The mechanical behavior of a mammalian lung alveolar duct model. *Journal of Biomechanical Engineering*, 117:254–261, 1995.
- [5] E. Denny and R. C. Schroter. Relationship between alveolar size and fibre distribution in a mammalian lung alveolar duct model. *Journal of Biomechanical Engineering*, 119:289–297, 1997.
- [6] E. Denny and R. C. Schroter. Viscoelastic behavior of a lung alveolar duct model. *Journal of Biomechanical Engineering*, 122:143–151, 2000.
- [7] E. Denny and R. C. Schroter. A model of non-uniform lung parenchyma distortion. *Journal of Biomechanics*, 39:652–663, 2006.

- [8] K. W. Rehn and P. K. Riggs. Non-lethal swimmer neutralization study. Technical Report 3138, Applied Research Laboratories, 2002.
- [9] M. S. Wochner, Yu. A. Ilinskii, M. F. Hamilton, and E. A. Zabolotskaya. Finite aperiodic model of human lung. *Journal of the Acoustical Society of America*, 120:3194(A), 2006.
- [10] Yu. A. Ilinskii, M. S. Wochner, M. F. Hamilton, and E. A. Zabolotskaya. Infinite periodic model of human lung. *Journal of the Acoustical Society of America*, 120:3194(A), 2006.
- [11] M. S. Wochner, Yu. A. Ilinskii, M. F. Hamilton, and E. A. Zabolotskaya. Effective medium model of human lung response to low-frequency sound. *Journal of the Acoustical Society of America*, 121:3082(A), 2007.
- [12] M. S. Wochner, Y. Zhang, Yu. A. Ilinskii, M. F. Hamilton, and E. A. Zabolotskaya. Influence of inhomogeneity and geometry on lung response to low-frequency underwater sound. *Journal of the Acoustical Society of America*, 122:2957(A), 2007.
- [13] M. S. Wochner, Yu. A. Ilinskii, M. F. Hamilton, and E. A. Zabolotskaya. Simulated response of the human lung to low-frequency underwater sound using a finite-element-based thoracic model. *Journal of the Acoustical Society of America*, 123:3914(A), 2008.
- [14] M. S. Wochner, Yu. A. Ilinskii, M. F. Hamilton, and E. A. Zabolotskaya. Development of a lung tissue fatigue and failure model. *Journal of the*

Acoustical Society of America, 124:2446(A), 2008.

- [15] D. Dalecki, S. Z. Child, and C. H. Raeman. Lung damage from exposure to low-frequency underwater sound. *Journal of the Acoustical Society of America*, 111:2462(A), 2002.
- [16] M. P. Hlastala and A. J. Berger. *Physiology of respiration*, chapter 2, pages 4, 6–21, 41–42. Oxford University Press, New York, 1996.
- [17] F. H. Netter. *Atlas of Human Anatomy*, page 183. Novartis, New Jersey, 1997.
- [18] H. Gray. *Anatomy of the human body*, page 1396. Lea & Febiger, Philadelphia, 20th edition, 1918.
- [19] F. H. Netter. *Respiratory System*, volume 7 of *The Ciba Collection of Medical Illustrations*, page 24. Ciba, Summit, New Jersey, 1979.
- [20] J. E. Hansen and E. P. Ampaya. Human air space shapes, sizes, areas, and volumes. *Journal of Applied Physiology*, 38:990–995, 1975.
- [21] G. E. Angus and W. M. Thurlbeck. Number of alveoli in the human lung. *Journal of Applied Physiology*, 32:483–485, 1972.
- [22] E. R. Weibel. *Morphometry of the human lung*. Springer-Verlag, New York, 1963.

- [23] E. H. Oldmixon and F. G. Hoppin, Jr. Distribution of elastin and collagen in canine lung alveolar parenchyma. *Journal of Applied Physiology*, 67:1941–1949, 1989.
- [24] J. Mead. Mechanical properties of lungs [review]. *Physiological Reviews*, 41:281–330, 1961.
- [25] J. Hutchinson. Thorax. *Todd Encyclopedia of Anatomy and Physiology*, pages 1849–1852, 1059, 1849.
- [26] E. P. Radford, Jr. and N. M. Lefcoe. Effects of bronchoconstriction on elastic properties of excised lungs and bronchi. *American Journal of Physiology*, 180:479, 1955.
- [27] M. B. McIlroy. Physical properties of normal lungs removed after death. *Thorax*, 7:285, 1952.
- [28] D. H. Glaister, R. C. Schroter, M. F. Sudlow, and J. Milic-Emili. Bulk elastic properties of excised lungs and the effect of a transpulmonary pressure gradient. *Respiration Physiology*, 17:343–364, 1973.
- [29] F. G. Hoppin, Jr. and J. Hildebrandt. *Bioengineering Aspects of the Lung*. Marcel Dekkar, Inc., New York, 1977.
- [30] E. J. Burger and P. T. Macklem. Airway closure: demonstration by breathing 100% oxygen O_2 at low lung volumes and by N_2 washout. *Journal of Applied Physiology*, 25:139–148, 1968.

- [31] J. M. B. Hughes, D. Y. Rosenzweig, and P. B. Kivitz. Site of airway closure in excised dog lungs: histologic demonstration. *Journal of Applied Physiology*, 29:340–344, 1970.
- [32] R. Kowe, R. C. Schroter, F. L. Matthews, and D. Hitchings. Analysis of elastic and surface tension effects in the lung alveolus using finite element methods. *Journal of Biomechanics*, 7:541–549, 1986.
- [33] M. A. Hajji, T. A. Wilson, and S. J. Lai-Fook. Improved measurements of shear modulus and pleural membrane tension of the lung. *Journal of Applied Physiology; Respiratory Environmental Exercise Physiology*, 47:175–181, 1979.
- [34] E. H. Oldmixon and F. G. Hoppin, Jr. Comparison of amounts of collagen and elastin in pleura and parenchyma of dog lung. *Journal of Applied Physiology: Respiratory, Environmental, Exercise Physiology*, 56:1383–1388, 1984.
- [35] T. A. Wilson and H. Bachofen. A model for mechanical structure of the alveolar duct. *Journal of Applied Physiology*, 52:1064–1070, 1982.
- [36] R. W. Carton, J. Dainauskas, B. Tews, and C. M. Hass. Elastic properties of single elastic fibers. *Journal of Applied Physiology*, 17:547–551, 1962.
- [37] Y. C. Fung. *Biomechanics: Mechanical Properties of Living Tissues*. Springer-Verlag, New York, second edition, 1993.

- [38] D. D. Stromberg and C. A. Wiederhielm. Viscoelastic description of a collagenous tissue in simple elongation. *Journal of Applied Physiology*, 26:857–862, 1969.
- [39] H. Fukaya, C. J. Martin, A. C. Young, and S. Katsura. Mechanical properties of alveolar walls. *Journal of Applied Physiology*, 25:689–695, 1968.
- [40] F. G. Hoppin, Jr., G. C. Lee, and S. V. Dawson. Properties of lung parenchyma in distortion. *Journal of Applied Physiology*, 39:742–751, 1975.
- [41] H. Hamm, H. Fabel, and W. Bartsh. The surfactant system of the adult human lung: physiology and clinical perspectives. *Clinical Investigator*, 70:637–657, 1992.
- [42] G. N. Maksym. *Modelling Lung Tissue Rheology*. PhD thesis, McGill University, 1997.
- [43] Y. C. Fung. *Biomechanics: Motion, Flow, Stress, and Growth*, chapter 11. Springer-Verlag, New York, 2nd edition, 1990.
- [44] A. Heynsius. Ueber die grösse des negativen drucks im thorax beim ruhigen athmen. *Archiv für die gesamte Physiologie des Menschen und der Tiere*, 29:265, 1882.
- [45] G. A. Cavagna, E. J. Stemmler, and A. B. DuBois. Alveolar resistance to atelectasis. *Journal of Applied Physiology*, 22:441–452, 1967.

- [46] W. Cheng, D. S. Delong, G. N. Franz, E. L. Petsonk, and D. G. Fraser. Contribution of opening and closing of lung units to lung hysteresis. *Respiration Physiology*, 102:205–215, 1995.
- [47] R. R. Mercer and J. D. Crapo. Spatial distribution of collagen and elastin fibers in the lungs. *Journal of Applied Physiology*, 69:756–765, 1990.
- [48] S. S. Sobin, Y. C. Fung, and H. M. Tremer. Collagen and elastin fibers in human pulmonary avleolar walls. *Journal of Applied Physiology*, 64:1659–1675, 1988.
- [49] R. R. Mercer, M. L. Russell, and J. D. Crapo. Alveolar septal structure in different species. *Journal of Applied Physiology*, 77:1060–1066, 1994.
- [50] R. E. Brown, J. P. Butler, J. J. Godleski, and S. H. Loring. The elephant's respiratory system: adaptation to gravitational stress. *Respiratory Physiology*, 109:177–194, 1997.
- [51] R. Graham. Y. C. Fung wins Russ Prize. *Medical News Today*, 2007.
- [52] Y. C. Fung. Does surface tension make the lung inherently unstable? *Circulation Research*, 37:497–502, 1975.
- [53] T. A. Wilson. A continuum analysis of a two-dimensional mechanical model of lung parenchyma. *Journal of Applied Physiology*, 33:472–478, 1972.

- [54] Y. C. Fung. A model of lung structure and its validation. *Journal of Applied Physiology*, 64:2132–2141, 1988.
- [55] R. K. Lambert and T. A. Wilson. A model of the elastic properties of the lung and their effect on respiratory flow. *Journal of Applied Physiology*, 34:34–48, 1973.
- [56] D. Stamenovic and T. A. Wilson. A strain energy function for lung parenchyma. *Journal of Biomechanical Engineering*, 107:81–86, 1985.
- [57] B. Budiansky and E. Kimmel. Elastic moduli of the lungs. *Journal of Applied Mechanics Transactions of the ASME*, 54:351–358, 1987.
- [58] E. Denny and R. C. Schroter. A mathematical model for the pulmonary morphology of the pulmonary acinus. *Journal of Biomechanical Engineering*, 118:210–215, 1996.
- [59] D. R. Otis, E. P. Ingenito, R. D. Kamm, and M. Johnson. Dynamic surface tension of surfactant ta: Experiments and theory. *Journal of Applied Physiology*, 77:2681–2688, 1994.
- [60] R. R. Mercer and J. D. Crapo. Three-dimensional reconstruction of the rat acinus. *Journal of Applied Physiology*, 63:785–794, 1987.
- [61] J. S. Martin, P. H. Rogers, and E. A. Cudahy. Measurement of the depth-dependent resonance of water-loaded human lungs. *Journal of the Acoustical Society of America*, 117:2291–2300, 2005.

- [62] T. G. Leighton. *The Acoustic Bubble*. Academic, New York, 1994.
- [63] M. F. Pistorius. Effects of low frequency waterborne sound on divers. Technical Report ARL-TR-96-5, Applied Research Laboratories, The University of Texas at Austin, 1996.
- [64] E. Cudahy, E. Hanson, and D. Fothergill. Summary report on the bioeffects of low frequency waterborne sound. Technical Report 3 LFA EIS, Naval Submarine Medical Research Laboratory, 1999.
- [65] S. A. Sahn and J. E. Heffner. Spontaneous pneumothorax. *New England Journal of Medicine*, 342:868–874, 2000.
- [66] A. S. Slutsky. Lung injury caused by mechanical ventilation. *Chest*, 116:9S–15S, 1999.
- [67] S. Denot-Ledunois, G. Vardon, P. Perruchet, and J. Gallego. Effects of voluntary changes in breathing frequency on respiratory comfort. *Biological Psychology*, 49:71–82, 1998.
- [68] K. E. Schaefer, W. P. McNulty, Jr., C. Carey, and A. A. Liebow. Mechanisms in development of interstitial emphysema and air embolism on decompression from depth. *Journal of Applied Physiology*, 13:15–29, 1958.
- [69] J. N. Maina and J. B. West. Thin and strong! The bioengineering dilemma in the structural and functional design of the blood-gas barrier. *Physiological Review*, 85:811–844, 2005.

- [70] M. Wochner. Personal communication, August 22, 2008.
- [71] L. D. Landau and E. M. Lifshitz. *Theory of Elasticity*, volume 7 of *Course of Theoretical Physics*. Pergamon Press, New York, second edition, 1970.
- [72] W. H. Press, S. A. Teukolsky, W. T. Vetterling, and B. P. Flannery. *Numerical Recipes in Fortran 90*. Cambridge University Press, New York, second edition, 1996.

Vita

Paul Allen Waters was born in Austin, Texas on September 28, 1983, the son of Laura Lee Waters and Michael Earl Waters. After receiving a diploma from Pflugerville High School in May of 2002, he was awarded a summer position in the Applied Research Laboratories High School Internship Program. In August of 2002, he enrolled in the University of Texas at Austin. In May 2006, he received a degree of Bachelor of Science in Mechanical Engineering. The following August, he entered graduate school at the University of Texas at Austin.

Permanent address: 405 Suzzane Rd
Pflugerville, Texas 78660

This thesis was typeset with \LaTeX^\dagger by the author.

[†] \LaTeX is a document preparation system developed by Leslie Lamport as a special version of Donald Knuth's \TeX Program.